Corrosion Performance of High Temperature Alloys in Molten Salt Mixtures for Next Generation Energy Systems

Isabella McDonald

Supervisor: Dr. Joey Kish

Department of Materials Science and Engineering

McMaster University

Thesis submitted in partial fulfillment of the requirements for the Degree of Master of Applied Science

December 2021

Abstract

Molten chloride salts have been proposed to be used as the primary coolant in molten salt reactors, and as the heat transfer fluid in concentrated solar power plants in next generation energy system design. The corrosive properties of molten chloride salts make it challenging to find appropriate structural materials for plant/system realization. In this work, two corrosion mitigation strategies are investigated to determine the relative corrosion performance of high temperature alloys in molten chloride salt mixtures: (1) chemical purification of salt mixture using a Mg sacrificial anode and (2) developing a protective oxide layer on the surface of high temperature alloys after pre-oxidation. These corrosion inhibitors are studied in combination with each other to determine the relative corrosion performance of three high temperature alloys: Incoloy 800H (chromia former), Haynes 214 (alumina former), and Noram SX (silica former). The unprotected and pre-oxidized alloys were exposed to molten chloride salt (62.5 wt % KCl + 37.5 wt % $MgCl_2 \cdot 6H_2O$) with and without 1.7 wt % Mg as a corrosion inhibitor for 100 h at 700°C under inert Ar atmosphere. SEM-EDS characterization was used to compare cross-sections and surfaces of each alloy exposed to molten salt with and without Mg additions.

SEM-EDS cross-sectional characterization revealed significant Cr depletion in each unprotected alloy, and reduced Cr depletion in alloys immersed in molten chloride salt mixtures with chemical purification included. The addition of Mg metal to the salt mixture resulted in the precipitation of MgO on the alloy surfaces. The oxide deposition of MgO on components may impact the thermal and mechanical performance of the system. Therefore, the addition of Mg should be optimized for use in an operational system. Cross-sectional analysis identified the dissolution of Cr_2O_3 and SiO_2 oxide scales and a stable Al_2O_3 oxide scale post-exposure.

Acknowledgements

I would like to thank my supervisor Dr. Joey Kish for sharing his corrosion wisdom with me and whose support made this project possible. I am deeply grateful to Dr. Beth McNally whose guidance was crucial for the success of this project. I would also like to thank Dr. David Novog for sitting on my committee and sharing his expertise.

I would also like to thank Jhoynner Martinez, Carmen Andrei, and Travis Casagrande for microscopy assistance. Thanks are also expressed to Chris Thomsen (Noram Engineering), Joshua Roberts (VDM Metals), and Jim Kaiser (ORNL) for donating material to this project.

I wish to thank my fiancé, Josh, for his unconditional patience, support, and love throughout these last two years. Finally, I would like to thank my mom, Tanya, for being my mentor and always encouraging me to do my best. I am forever grateful of your support, and I would not be who I am today without you. This work is dedicated to you.

Abbreviations and Symbols

List of Abbreviations

MSR	Molten Salt Reactor
CSP	Concentrated Solar Power
SMR	Small Modular Reactor
ORNL	Oak Ridge National Laboratory
MSRE	Molten Salt Reactor Experiment
IMSR	Integral Molten Salt Reactor
BPVC	Boiler and Pressure Vessel Code
ASME	American Society of Mechanical Engineers
I800H	Incoloy 800H
H214	Haynes 214
SX	Noram SX
LOM	Light Optical Microscopy
RD	Rolling Direction
ND	Normal Direction
BSE	Backscattered Electron
UP	Unprotected
CP	Chemical Purification
PO	Pre-oxidation
SEM	Scanning Electron Microscopy
EDS	Energy Dispersive X-Ray Spectroscopy
SE	Secondary Electron
XRD	X-Ray Diffraction
FIB	Focused Ion Beam

TEM	Transmission Electron Microscopy

List of Symbols

h	Hours
°C	Degrees Celsius
µm	Micrometer
nm	Nanometer
ΔG°	Standard Gibbs Free Energy
%	Percent
kJ	Kilojoule

Table of Contents

List of Figures

List of Tables

1.0 Introduction

In November of 2020, the Government of Canada introduced the Canadian Net-Zero Emissions Accountability Act [1]. This Act formalized Canada's target to achieve net-zero emissions by the year 2050. Deployment of advanced nuclear and renewable energy sources is considered necessary in the near term to meet this objective. Molten salt reactors (MSR) and concentrated solar power (CSP) are promising technologies that produce energy with zero greenhouse emissions. Descriptions of these two technologies and of the common limiting material challenges are provided separately below.

1.1 Molten Salt Reactors (MSRs)

In recent years, the government of Canada has expressed great interest and support in the development and deployment of small modular reactors (SMR) [2]. One candidate for a potential SMR is the MSR. MSRs are a class of nuclear fission reactors in which the primary coolant is molten salt containing dissolved fuel and fission products. MSRs were initially researched for civilian use throughout the 1960s by Oak Ridge National Laboratory (ORNL) in the project titled, "The Molten Salt Reactor Experiment (MSRE)" [3]. This project revealed many design benefits for MSRs compared to conventional water-cooled reactors.

Molten fluoride and chloride salts are thermally stable which permits high temperature operation that facilitates a high energy conversion efficiency. They can operate at close to atmospheric pressure, which significantly reduces the cost of containment structures. MSRs have many inherent safety features that classify them as 'walk-away safe'. MSRs are not cooled by water, therefore the risk of steam explosions is eliminated, and if the reactor temperature increases past a critical

point, then freeze valves are passively melted and the salt is drained into storage tanks. Thorium, uranium, or plutonium are readily dissolved in molten salts giving each of them the capability of being used as a dissolved fuel. This is especially important for countries that are short on uranium deposits since they can use the substantially more abundant thorium. Fuel can be processed online to remove or add selective components, whereas solid fuel must be removed, treated, remanufactured, and reinserted in the reactor.

Terrestrial Energy is a nuclear company working on developing a 195 MWe Integral Molten Salt Reactor (IMSR®) in Oakville, ON [4]. Their design, as an example, incorporates many aspects of the MSRE that were researched, demonstrated, and proven by the test reactors at ORNL. Figure 1.1 displays Terrestrial Energy's Integral Molten Salt Reactor (IMSR®). This schematic demonstrates how this reactor can be used for a variety of applications such as power generation, grid services, and process heat uses.

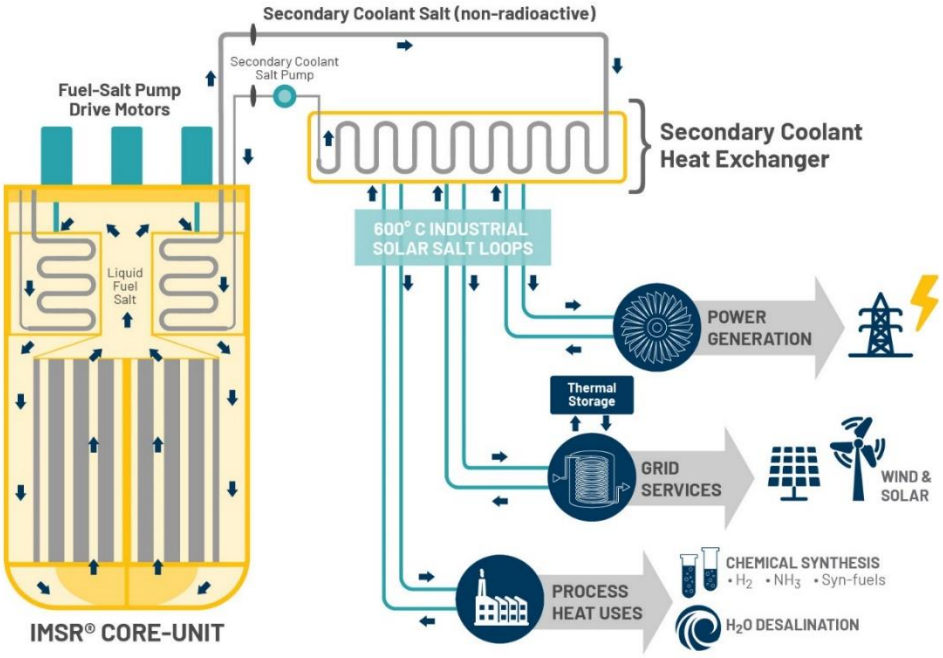

Figure 1.1: Terrestrial Energy's IMSR® concept [4].

1.2 Concentrated Solar Power (CSP) Plants

CSP technology is emerging as a future renewable energy system. CSP systems use thousands of curved mirrors that concentrate the sun's energy to a receiving tower that transfers the energy to a heat transfer fluid. This heat transfer fluid can be used to drive traditional steam turbines that generate electricity or can be stored in thermal storage systems for later use. Figure 1.2 displays a CSP concept that includes a molten salt receiver tower and storage system. These systems have a much greater advantage over photovoltaic cells because they can generate dispatchable power in the absence of sunlight. Current CSP technologies use nitrate salt mixtures as the thermal energy storage medium and heat transfer fluid and operate at 500 °C [5]. Next generation CSP plants aim to increase operating temperatures to as high as 800 °C to increase the efficiency of the power cycle. This operation temperature increase requires a change in molten salt since nitrate mixtures decompose at temperatures above 550 °C. Candidate salts must have favourable thermophysical properties such as a low melting point, high heat capacity, high thermal conductivity, compatibility with containment materials, and thermal stability at temperatures as high as 750 °C [6]. Three candidate salts have been identified by the National Renewable Energy Laboratory's CSP Gen3 Demonstration Roadmap: $KCl\text{-}MgCl_2$, KCl- $NaCl\text{-}ZnCl_2$, and $Na_2CO_3\text{-}K_2CO_3\text{-}Li_2CO_3$ [6].

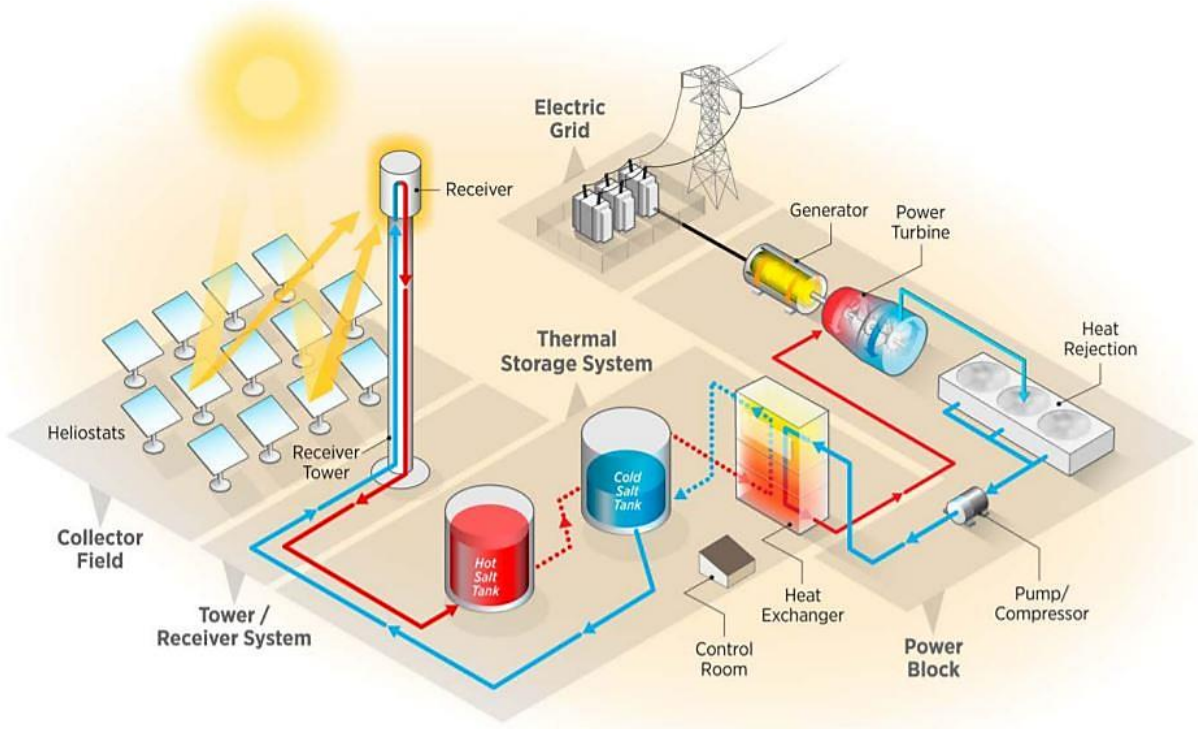

Figure 1.2: Molten salt power tower with direct storage of salt [6].

1.3 Common Material Challenge

One of the most significant challenges that the commercialization of MSRs and CSP plants face is material degradation by corrosion. Structural metallic materials (alloys) must have maximized durability to extend the system's lifetime, thereby increasing its economic competitiveness. The foundational work done by the MSRE revealed the instability of protective chromia oxide films and the selective removal of Cr from metal matrices when in contact with molten fluoride salt [3]. The selective removal of Cr by fluoride mixtures is described by the following chemical reactions [7]:

1. Due to impurities in the melt such as

$$FeF_2 + Cr \rightarrow CrF_2 + Fe \quad 1.1$$

$$2HF + Cr \rightarrow CrF_2 + H_2 \quad 1.2$$

2. Dissolution of oxide films from the metal surface such as

$$2Fe^{3+}(from\ film) + 3Cr \rightarrow 2Fe + 3Cr^{2+} \quad 1.3$$

3. Due to constituents in the fuel such as

$$Cr + 2UF_4 \rightarrow 2UF_3 + CrF_2 \quad 1.4$$

Research has shown that the selective removal of Cr is also common in molten chloride salts [5, 9-12, 34-35]. The conditions that accelerate corrosion rates in molten chloride salts are impurities, thermal gradients, irradiation (MSRs), and dissimilar material coupling. As an example of corrosion experienced by Cr-containing alloys, Figure 1.3 shows a cross-sectional SEM image of a Hastelloy N sample that was exposed to FLiNaK salt at 850 °C for 500 h and an associated distribution map acquired using X-ray dispersive spectroscopy (EDS). The Cr map clearly shows uniform depletion from the surface of Hastelloy N.

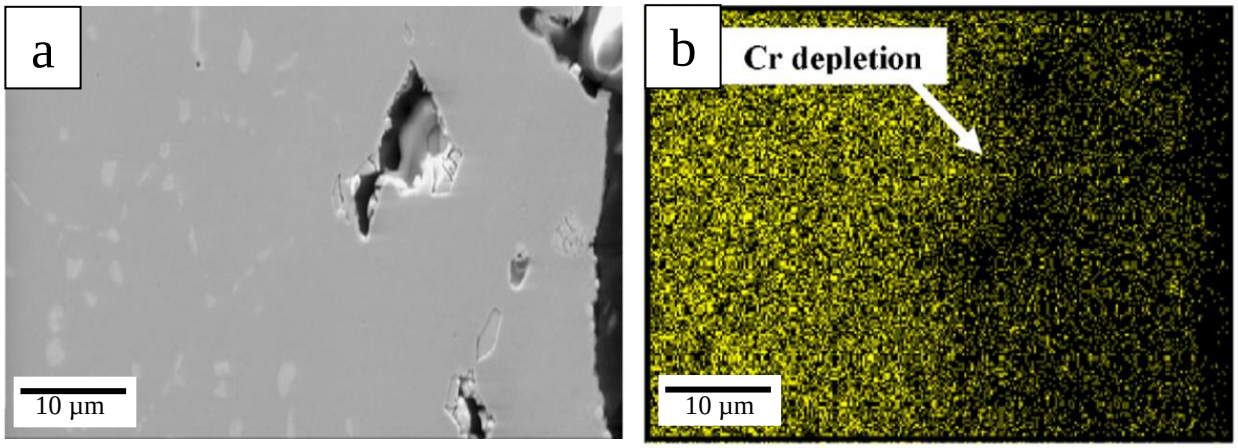

Figure 1.3: (a) SEM-BSE and (b) EDS Cr map of the cross-section of Hastelloy N after exposure to FLiNaK salt at 850 °C [8].

Structural alloys must meet specific codes and standards such as the Boiler and Pressure Vessel Code (BPVC) from the American Society of Mechanical Engineers (ASME) to be approved by nuclear regulators for use in nuclear reactors. The process to approve new reactor materials is extensive and expensive, therefore corrosion control measures other than material selection should be sought. Mitigation methods are utilized as a less expensive strategy to lower the corrosion rates of structural materials exposed to molten salts. Adding a corrosion inhibitor is an effective method to mitigate corrosion by lowering the redox potential of the salts [1, 9-10]. These inhibitors preferentially react with impurities generated by corrosion reactions between the alloy and the salt. An alternative strategy is used to grow a protective oxide on a given alloy, as a surface pre-treatment process, to help serve as a barrier layer between corrosive molten salt mixtures and the alloy [1, 11, 12]. Thus, the objective of this work is to compare the aforementioned control strategies on different scale-forming alloys when immersed in a molten chloride salt mixture.

1.4 Thesis Outline

Section 1 provides a description of MSR and CSP technologies, as well as their common material challenges, building upon the description provided above. Section 2 discusses the background information necessary to place the research conducted in this thesis within the context of the current knowledge base. Section 3 outlines the experimental procedures and parameters used in this project. Section 4 presents the results of the experimental procedure, whereas Section 5 discusses the effectiveness of each mitigation method and compares the performance of each alloy. Section 6 presents the major conclusions made in this thesis and includes recommendations for future work.

2.0 Literature Review

2.1 Characteristics of Molten Chloride Salt Corrosion

The passive oxide film that protects an alloy from corrosion is chemically unstable when exposed to molten chloride salt [13-19]. When the native oxide film is dissolved by molten salt, alloying elements are vulnerable to dissolution. Exposed metal must be thermodynamically more stable than the salt constituents to resist dissolving into the salt as a metal chloride. Corrosion proceeds even after this condition has been met by other forms such as impurity-driven corrosion, galvanic corrosion, and corrosion caused by temperature gradients. This research addresses the impurity-driven corrosion mechanism.

2.1.1 Thermodynamics

Corrosion of metals in molten chloride salt is driven by the nobility of the metal. Metals with higher negative Gibbs free energies of chloride formation are more likely to form a chloride compound and dissolve in the salt, therefore initiating corrosion by the selective oxidation and removal of the least noble component [20-23]. Figure 2.1 below displays the Gibbs free energies of formation of metal chlorides. Of the most common alloys considered for use in MSRs and CSPs, those with Cr are unattractive since Cr forms a relatively stable chloride and is therefore prone to selective removal. Fe is also prone to selective removal, but not as severely as Cr. Equation (2.1) demonstrates an example of a chemical formula for the formation of $CrCl_2$ involving Cl_2 (g).

$$Cr(s) + Cl_2(g) \rightarrow CrCl_2(s) \qquad 2.1$$

Figure 2.1 demonstrates that the chloride salt constituents are thermodynamically favoured over the chlorides of typical alloying elements. This indicates that the salt, without impurities, should not oxidize the alloying elements, and thus cause corrosion.

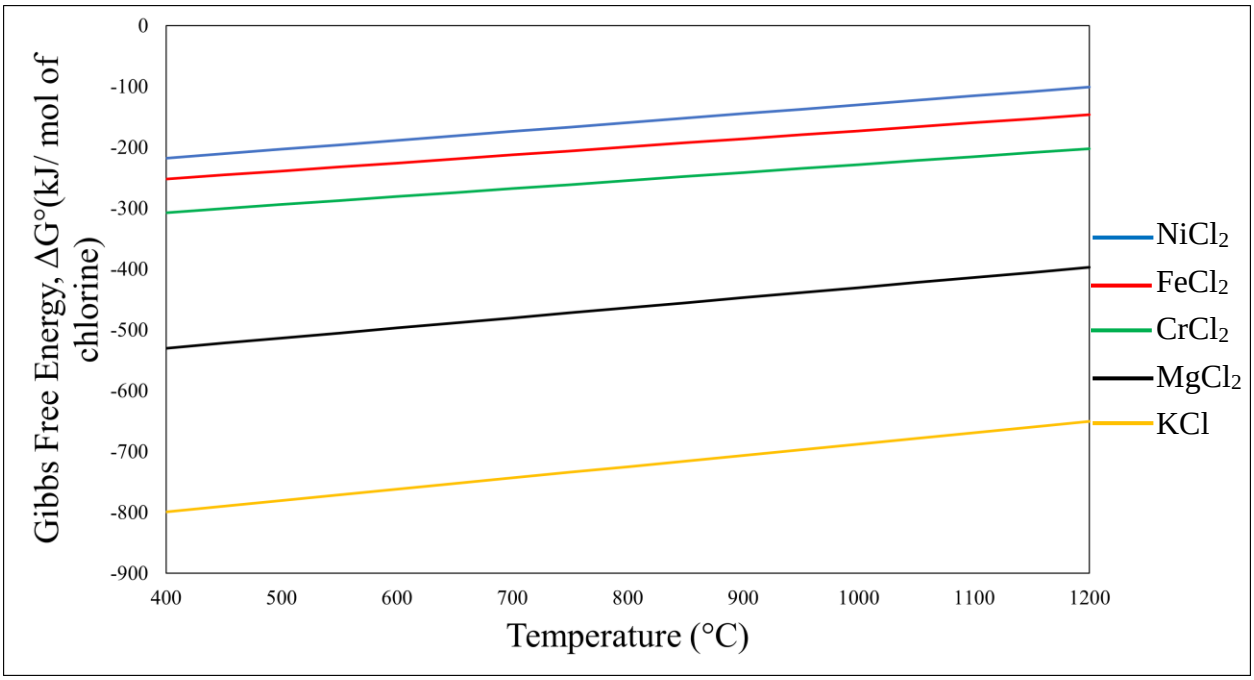

Figure 2.1: Ellingham-Richardson diagram of common chlorides.

2.1.2 Impurity-Driven Corrosion

It is well accepted that the corrosion of alloys in molten chlorides is primarily driven by the impurities within the salt [17, 21, 23-28]. Problematic impurities include, but are not limited to, moisture (H_2O) and O_2 dissolved in the chloride salts [29-31]. Moisture residing in salts is commonly found in the form of hydrates (discussed in more detail later) which promotes hydrolysis during heating. Equation (2.2) demonstrates an example of a hydrolysis reaction between $MgCl_2$ (s) and H_2O (g) [9]. This reaction between $MgCl_2$ (s) and H_2O (g) produces the corrosive impurities MgOHCl (s) and HCl (g). At temperatures greater than 550 °C, MgOHCl (s) decomposes in a molten $MgCl_2$-containing mixture to form MgO (s), $MgOH^+$, Cl^-, and HCl (g) as

shown in Equations (2.3) and (2.4) [9]. HCl (g) can react with O_2 (g) in the atmosphere to produce Cl_2 and H_2O as demonstrated in Equation (2.5).

$$MgCl_2(s) + H_2O(l) \rightarrow MgOHCl(s) + HCl(g) \quad 2.2$$

$$MgOHCl(s) \rightarrow MgO(s) + HCl(g) \quad 2.3$$

$$MgOHCl(s) \rightarrow MgOH^+ + Cl^- \quad 2.4$$

$$O_2(g) + 4HCl(g) \rightarrow 2Cl_2(g) + H_2O(g) \quad 2.5$$

HCl (g) reacts with the metallic materials, as demonstrated in Equation (2.6) to form solid metal chlorides at target temperatures of Gen. IV MSRs and next generation CSP plants. $MgOH^+$ corrodes metallic materials as shown in Equation (2.7). Cl_2 (g) can diffuse through grain boundaries as well as cracks and pores, of the oxide scale to the substrate, where it reacts with the metal as shown in Equation (2.8).

$$xHCl\ (g) + M(s) \rightarrow MCl_x(s) + \frac{x}{2}H_2(g) \quad 2.6$$

$$xMgOH^+ + M(s) \rightarrow xMgO(s) + M^{x+}(s) + \frac{x}{2}H_2(g) \quad 2.7$$

$$M(s) + Cl_2(g) \rightarrow MgCl_2(s) \quad 2.8$$

The detrimental effects of impurities in molten chloride salts and its atmosphere have been studied by many researchers [22-26, 31-33]. Liu *et al*. [34] studied the corrosion mechanism of Ni-based alloys in molten chloride salts under air atmosphere. Isothermal corrosion tests were conducted at 600 °C, and alloys Inconel 625 (Ni-58Cr-22Fe-5), Hastelloy X (Ni-48Cr-22Fe-19), and Hastelloy B-3 (Ni-65Cr-1.5Fe-1.5) were immersed in molten NaCl-$CaCl_2$-$MgCl_2$. Since the experiments were carried out in air, it was expected that O_2 (g) and H_2O (g) would significantly

accelerate corrosion. The following reactions were proposed to describe the corrosion observed. First, O_2 (g) and H_2O (g) impurities present in the atmosphere react with the molten salt according to Equations (2.9) and (2.10).

$$MgCl_2(l) + H_2O(g) \rightarrow MgO(s) + 2HCl(g) \quad 2.9$$

$$4HCl(g) + O_2(g) \rightarrow 2Cl_2(g) + 2H_2O(g) \quad 2.10$$

Dissolved O_2 (g) from the atmosphere reacts with the alloys to form an oxide scale as demonstrated in Equation (2.11).

$$xM(s) + \frac{y}{2}O_2(g) \rightarrow M_xO_y(s) \quad 2.11$$

Cl_2 is then able to penetrate through the oxide scale and deeper into the inner corrosion layers through pores and cracks where it reacts with Cr to produce $CrCl_4$ (g) as shown in Equation (2.12.)

$$Cr(s) + 2Cl_2 \rightarrow CrCl_4(g) \quad 2.12$$

$CrCl_4$ (g) then diffuses into the outer corrosion layer where it reacts with O_2 (g) to form CrO_2Cl_2 (g), according to Equation (2.13).

$$CrCl_4(g) + O_2(g) \rightarrow CrO_2Cl_2(g) + Cl_2(g) \quad 2.13$$

CrO_2Cl_2 (g) then diffused into the molten salt. Thus, corrosion manifests itself as a Cr depleted region in the alloy at the surface. It was concluded that the formation of Cl_2 (g) due to the reaction between O_2 (g) and H_2O (g) as atmospheric impurities, and $MgCl_2$ are the driving force for the corrosion of Ni-based alloys exposed to molten chloride salt under an air atmosphere. Cr is preferentially depleted due to due its high negative Gibbs free energy of chloride formation compared to other common alloying elements, as displayed in Figure 2.1.

Ding *et al*. [35] presented a corrosion mechanism to describe how Cr is depleted from a Ni-Cr-Fe alloy exposed to molten NaCl-KCl-$MgCl_2$ in contact with an inert atmosphere. First, $MgOH^+$ disassociates into Mg^{2+}, O^{2-}, and H^+ as described by Equation (2.14):

$$MgOH^+ \leftrightarrow Mg^{2+} + O^{2-} + H^+ \qquad 2.14$$

H^+ penetrates the sample surface and reacts with Cr to form Cr^{2+} according to Equation (2.15):

$$Cr(s) + 2H^+ \rightarrow Cr^{2+} + H_2(g) \qquad 2.15$$

Cr^{2+} reacts with Mg^{2+} and O^{2-} to form $MgCr_2O_3$ (s) as described by Equation (2.16).

$$2Cr^{2+} + Mg^{2+} + 3O^{2-} \rightarrow MgCr_2O_3(s) \qquad 2.16$$

The formation of $MgCr_2O_3$ led to the enrichment of Cr-containing corrosion products on the surface of the alloys which resulted in a Cr-depleted region under the sample surface. Therefore Ding *et al*. concluded that the main driving force for alloys exposed to molten chloride salt under inert atmosphere is the dissociation of $MgOH^+$. Figure 2.2 shows an example of a cross-section and an associated set of SEM-EDS maps of corroded Incoloy 800H after immersion in molten $MgCl_2$-KCl-NaCl at 700 °C for 500 h. This cross-sectional analysis shows the corrosion products of Incoloy 800H contain Mg, Cr, and O. It was also observed that small Cr-depleted alloy fragments spalled off from the alloy surface during exposure.

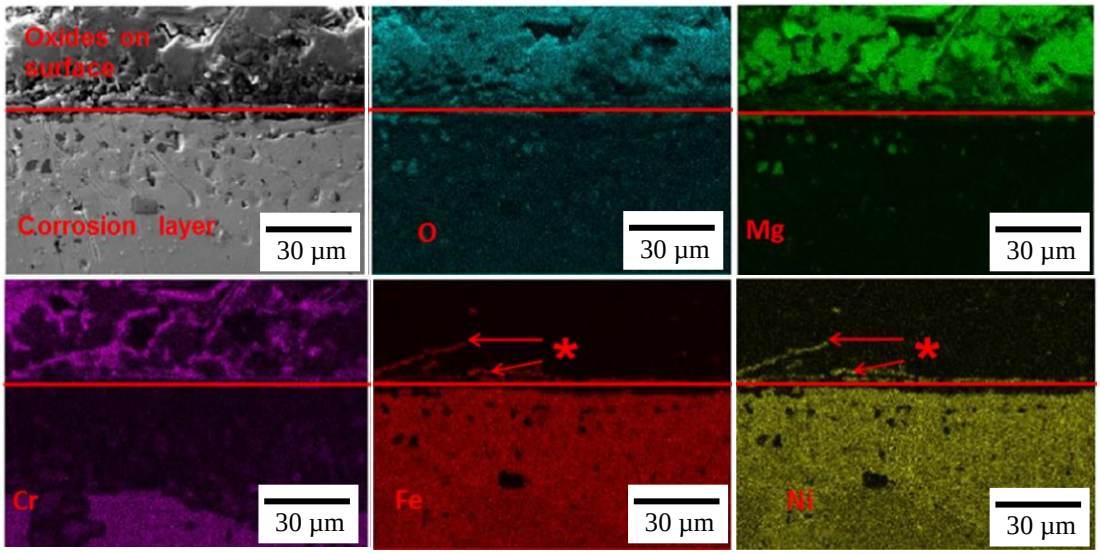

Figure 2.2: Cross-section SEM-EDS elemental maps of Incoloy 800H after immersion in molten $MgCl_2$-KCl-NaCl at 700 °C. *small Cr-depleted alloy fragments spalled off [35].

2.1.3 Alloying Elements

The alloys of interest for MSR and CSP systems mainly include those containing Ni, Cr, and Fe. Most literature agrees that alloys with a higher Ni content and lower Cr content perform better from a corrosion perspective when exposed to molten salt compared to stainless steels [34-40]. However, the conclusion that corrosion resistance increases with Ni content in molten chloride salt is not always true. Lai *et al*. [30] investigated alloys with varying Fe-Ni-Co compositions immersed in molten NaCl-KCl-$BaCl_2$ at 840 °C for one month. The best performing alloys of those tested were stainless steel (Types 304 and 310), which exhibited a lower depth of corrosion than the high Ni alloys (Inconel 600 and 604). Research conducted by ORNL showed that Hastelloy N suffered the least corrosion in those alloys tested in molten fluoride salts [41-45]. However, experiments conducted by Vignarooban *et al*. [46] indicate that Hastelloy N may not be a compatible alloy with molten chloride salts. Corrosion rates of Hastelloy C-276 (Ni-57Cr-16), Hastelloy C-22 (Ni-56Cr-22), and Hastelloy N (Ni-71Cr-7) in molten NaCl-KCl-$ZnCl_2$ salts at

500 °C were estimated using a steady-state potentiodynamic method. The corrosion rate was calculated to be >150 μm/year, 50 μm/year, and 42 μm/year for Hastelloy N, Hastelloy C-22, and Hastelloy C-276 respectively. These results suggest that alloys with higher Ni and lower Cr content experience more corrosion.

The selection of appropriate Cr content is very important when considering corrosion of alloys in molten chloride salts. Cr alloying is used to help improve mechanical properties of high temperature alloys and to promote the growth of a protective chromia scale [37-40] but can also be selectively dissolved due to its low nobility. Polovov *et al*. [51] investigated the corrosion of stainless steels Types 316L and 321 molten equimolar in NaCl-KCl at 750 °C. Metallographic analysis post exposure indicated that the precipitation of Cr carbides and Cr depletion caused intergranular oxidation. Liu *et al*. [34] studied the corrosion of Inconel 625 (60Ni-23Cr), Hastelloy X (47Ni-22Cr), and Hastelloy B3 (65Ni-1.5Cr) in molten NaCl-$CaCl_2$-$MgCl_2$ at 600 °C. Hastelloy B3 suffered more corrosion than Hastelloy X and Inconel 625. Hastelloy X and Inconel 625 exhibited large Cr depleted zones compared to Hastelloy B3, but both Hastelloy X and Inconel 625 showed evidence of a compact protective layer of $MgCr_2O_4$ (s) that helped mitigate corrosion. These results indicate that a lower Cr content reduces the corrosion resistance of grain boundaries, but a higher Cr content helps to form a protective $MgCr_2O_4$ (s) scale that can resist molten chloride salts. Ding *et al*. [35] also found that Hastelloy C-276 exhibited the best corrosion resistance when compared to Type 310 stainless steel (Fe-Cr-24Ni-22) and Incoloy 800H (Fe-Cr-20Ni-30) in molten $MgCl_2$-KCl-NaCl at 700 °C. The corrosion rates were measured to be 500 μm/year, 1000 μm/year, and 2000 μm/year for Hastelloy C-276, Incoloy 800H, and 310 stainless steel respectively. The results from these two studies indicate that the optimal Cr content for Ni-based alloys is likely between 7 and 22 wt%.

Additions of Al and Si to alloys can promote the growth of protective Al_2O_3 and SiO_2 scales, which is discussed in more detail in Section 2.3.3. Table 2.1 provides a snapshot of the corrosion rates measured from various alloys in molten chloride salts reported in the literature for comparative purposes.

Table 1.1: Comparison of corrosion rates of various alloys exposed to molten chloride salts under various conditions.

Alloy	Molten Salt	T (°C)	Atmosphere	Corrosion Rate (μm/year)	Scale Forming Tendency	Ref
Hastelloy C-22	KCl-NaCl-$ZnCl_2$	500	Air	35	Cr_2O_3	46
Hastelloy C-276	KCl-NaCl-$ZnCl_2$	500	Air	40	Cr_2O_3	46
Hastelloy C-22	KCl-NaCl-$ZnCl_2$	500	Air	45	Cr_2O_3	39
Hastelloy C-276	KCl-NaCl-$ZnCl_2$	500	Air	50	Cr_2O_3	39
Hastelloy N	KCl-NaCl-$ZnCl_2$	500	Air	>150	/	46
SS 304	KCl-NaCl-$ZnCl_2$	500	Air	381	Cr_2O_3, Fe_3O_4	39
Hastelloy C-276	KCl-NaCl-$ZnCl_2$	800	Air	500	Cr_2O_3	39
SS 304	KCl-NaCl-$ZnCl_2$	400	Inert	14	Cr_2O_3, Fe_3O_4	39
Hastelloy C-276	KCl-NaCl-$ZnCl_2$	800	Inert	10	Cr_2O_3	39
Hastelloy C-22	KCl-NaCl-$ZnCl_2$	800	Inert	14	Cr_2O_3	39
Hastelloy C-276	KCl-NaCl-$MgCl_2$	700	Inert	79	Cr_2O_3	35
Incoloy 800H	KCl-NaCl-$MgCl_2$	700	Inert	364	Cr_2O_3	35
SS 310	KCl-NaCl-$MgCl_2$	700	Inert	1581	Cr_2O_3, Fe_3O_4	35
SS 347	LiCl-NaCl	350	Nitrogen	7490	Cr_2O_3, Fe_3O_4	36
Inconel 625	LiCl-NaCl	650	Nitrogen	2800	Cr_2O_3	36
SS 310	LiCl-NaCl	650	Nitrogen	6420	Cr_2O_3, Fe_3O_4	36
SS 310	LiCl-NaCl	700	Nitrogen	12450	Cr_2O_3, Fe_3O_4	36
Incoloy 800H	LiCl-NaCl	700	Nitrogen	14310	Cr_2O_3	36
Ni (>99.97)	NaCl-$MgCl_2$	520	Air	57	/	21
GH 4033	NaCl-$MgCl_2$	520	Air	124	Cr_2O_3, $NiFe_2O_4$	21
Inconel 625	NaCl-$CaCl_2$-$MgCl_2$	600	Air	200	Cr_2O_3, Fe_3O_4	32
Hastelloy X	NaCl-$CaCl_2$-$MgCl_2$	600	Air	220	Cr_2O_3, Fe_2O_3	34
Hastelloy B3	NaCl-$CaCl_2$-$MgCl_2$	600	Air	440	Cr_2O_3	34

2.2 Corrosion Mitigation Strategies

2.2.1 Thermal Dehydration

Molten $MgCl_2$-containing salt mixtures are candidate heat transfer fluids for CSP and primary coolants for MSRs [20, 23, 35, 52-54]. $MgCl_2$ is naturally hygroscopic and can easily bond with water to form a series of hydrate compounds ($MgCl_2 \cdot nH_2O$, n =1, 2, 4, 6, 7, 12) [9-10, 25-26, 28]. It is undesirable for water to be present in molten salts due to hydrolysis reactions that occur at target operating temperatures of Gen. IV MSRs and next generation CSPs, as discussed in Section 2.12. The phase diagram outlined in Figure 2.3 displays the hydrated forms of $MgCl_2$ at various temperatures. The most hydrated form of $MgCl_2$ at room temperature is $MgCl_2 \cdot 6H_2O$.

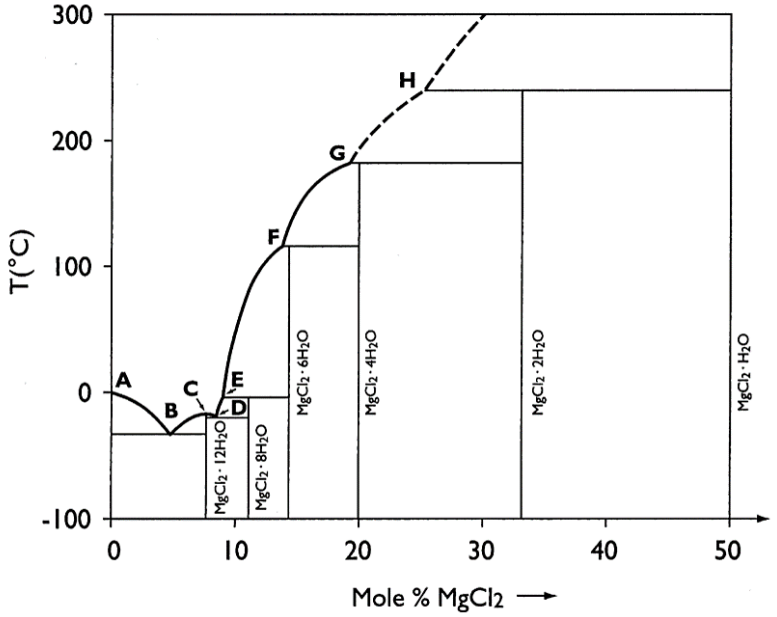

Figure 2.3: Phase diagram of $MgCl_2$ - water system [31].

To drive off these six waters, the temperature must be increased to dehydrate $MgCl_2$. The following dehydration reactions were outlined by Kipouros *et al.* [31]:

$$MgCl_2 \cdot 6H_2O(s) \rightarrow MgCl_2 \cdot 4H_2O(s) + 2H_2O(g) \sim 117°C \qquad 2.17$$

$$MgCl_2 \cdot 4H_2O(s) \rightarrow MgCl_2 \cdot 2H_2O(s) + 2H_2O(g) \sim 180°C \qquad 2.18$$

$$MgCl_2 \cdot 2H_2O(s) \rightarrow MgCl_2 \cdot H_2O(s) + H_2O(g) \sim 240°C \quad 2.19$$

$$MgCl_2 \cdot H_2O(s) \rightarrow MgCl_2(s) + H_2O(g) \sim 400°C \quad 2.20$$

Equations (2.17)-(2.20) demonstrate how thermal dehydration can be utilized to remove waters present in $MgCl_2$ salt. A consequence of the thermal dehydration process is the hydrolysis reactions that occur between $MgCl_2$ and H_2O to form corrosive compounds while the salt is drying according to Equation (2.2). To prevent the development of corrosive compounds, all hydrate waters need to be removed from the salt mixture before contact with metallic components to control corrosion. One such method to dehydrate an $MgCl_2$-containing salt mixture is outlined in the Section 2.2.2.

Zhao *et al*. [9] studied the content of MgOHCl in molten NaCl-KCl-$MgCl_2$ with and without thermal dehydration. Titration analysis was used to measure the concentration of MgOHCl in the original salt mixture, and salt mixture that had been thermally dehydrated at 117 °C for 8 hours, 180 °C for 8 h, 240 °C for 2 h, 400 °C for 1 h, and 600 °C for 1 h. Each step of the thermal dehydration procedure corresponds to the dehydration process outlined by Kipouros *et al*. [31]. The results of this experiment are shown in Figure 2.4 which demonstrate that the additive stepwise heating of carnallite salt is effective at purifying the salt. This is due to the significant reduction of MgOHCl content between the non-treated salt, and the thermally purified salt after 600 °C. The authors explained that this decrease in MgOHCl concentration at 600 °C corresponds to the thermal decomposition of the compound as described by Equations (2.3) and (2.4). More than 2 wt % MgOHCl content remained after the thermal dehydration process indicating that this method does not completely remove corrosive compounds. Figure 2.4 includes the MgOHCl content when a Mg corrosion inhibitor was added in the salt mixture. The content of MgOHCl was significantly lower compared to the thermally dehydrated mixture, indicating that chemical purification is an effective technique (discussed in more detail later).

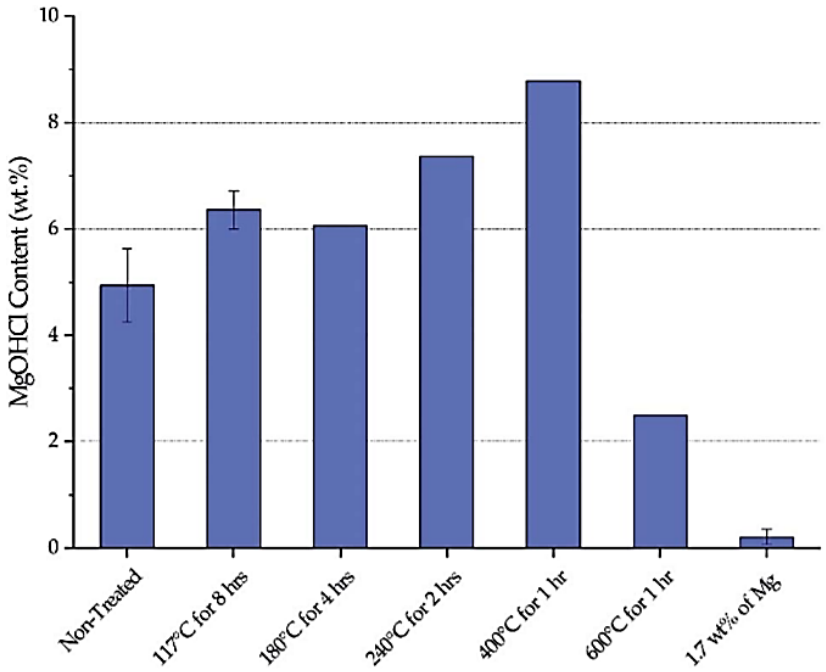

Figure 2.4: MgOHCl concentrations during thermal dehydration of NaCl-KCl-$MgCl_2$ carnallite salt [9].

Hosoya *et al*. [55] tested Hastelloy X in molten $NdCl_3$-NaCl-KCl that had been pre-dried at 550 °C for 70 minutes, 600 °C for 70 minutes, and 800 °C for 600 minutes. The corrosion rate of Hastelloy X when immersed in the molten salt mixture for 3 h at 250 °C was reported to be 5 mg/cm^2/h, 0.5 mg/cm^2/h, and 0.25 mg/cm^2/h for the salts dried at 500 °C, 600 °C, and 800 °C respectively. XRD post-exposure examination identified a NiO phase in each sample. Further examination using an atomic force microscope revealed that the NiO scale was stripped off and the bare metal experienced intergranular oxidation. The authors concluded that once the oxide scale was removed, corrosion of the alloy proceeded due to the reaction with HCl that was formed by Equation (2.21).

$$NdCl_3 + H_2O \rightarrow NdOCl + 2HCl \qquad 2.21$$

2.2.2 Chemical Purification

As previously mentioned in Section 2.12, corrosion of alloys in molten chloride salt mixtures is primarily driven by impurities. Impurities such as H_2O and O_2 react with the salt components and produce corrosive compounds as shown in Equations (2.1)-(2.7). Chemical purification is a technique that uses a sacrificial anode to selectively react with corrosive $MgOH^+$, therefore mitigating corrosion of structural alloys. Active metals can be added to the salt mixture to help reduce the redox potential of the mixture, and therefore decrease the concentration of $MgOH^+$ [5, 9-10]. The Gibbs free energy of formation is plotted against different cations in Figure 2.5. The chosen active metal must form a more stable cation than the alloying elements but cannot be more stable than the other constituents in the salt [9]. This leaves Mg metal as a good candidate since it does not introduce other elements into a $MgCl_2$ salt system.

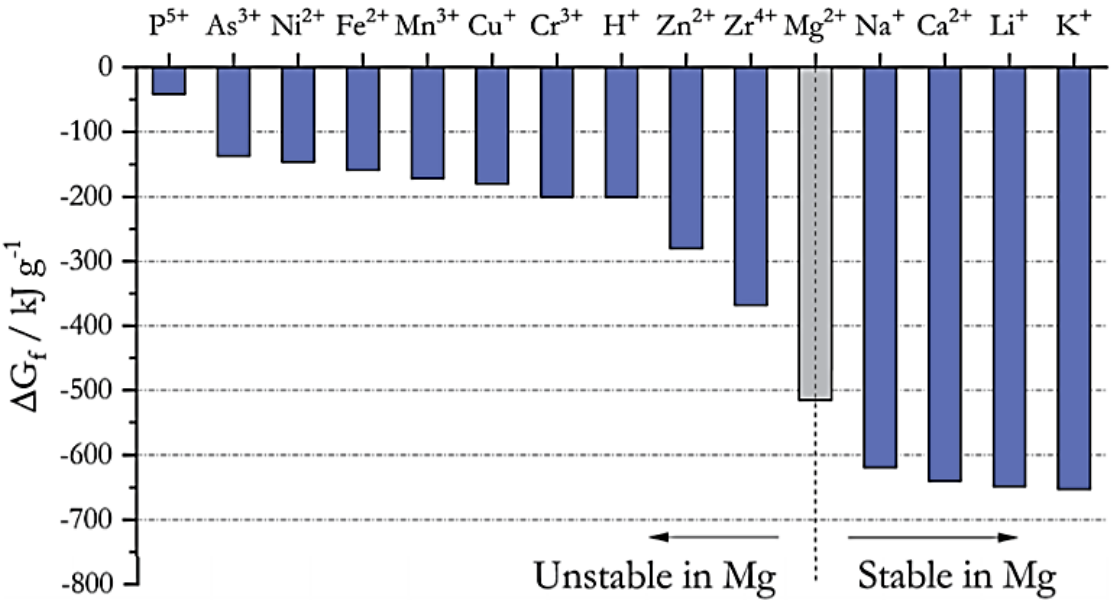

Figure 2.5: Gibbs free energy of formation for different cations at 827 °C [9].

Additions of Mg metal to molten chloride salt mixtures promotes oxygen scavenging. When a soluble $MgOH^+$ impurity is produced by the decomposition of MgOHCl (Equation (2.4)), it can transport oxygen to the substrate where it reacts with the alloying elements as described by Equation (2.7) [9]. Mg metal can reduce $MgOH^+$ to form MgO and H_2 as shown in Equation (2.22):

$$2MgOH^+ + Mg \rightarrow Mg^{2+} + 2MgO + H_2 \qquad 2.22$$

Garcia-Diaz *et al*. [53] studied the corrosion rates of alloys in molten KCl-$MgCl_2$ that contained 1.15 mol% of Mg. They found that samples immersed in the molten chloride salt mixture containing Mg metal as a corrosion inhibitor showed a corrosion rate that was 35 times lower than the samples immersed without the inhibitor added. Ding *et al*. [5] also investigated the effects of adding Mg metal as a corrosion inhibitor to molten chloride salt mixtures. Ni-based alloys were exposed to molten $MgCl_2$-NaCl-KCl at 700 °C for 500 h with an addition of 1 wt % Mg metal. The corrosion rate was reduced by 83% for Type 310 stainless steel, 70% for Incoloy 800H, and 94% Hastelloy C-276 when Mg metal was added.

Chlorinating processes have been studied as an effort to help reduce the hydrolysis reaction within molten chloride salt mixtures [20, 56]. Studies performed by ORNL found that drying chloride salts under vacuum before heating, then treating the salt with dry HCl (g), and finishing with an inert gas purge of HCl (g) from the salt, almost completely removed bound oxygen from the salts [20]. Cherginets *et al*. [56] found that a more effective method of removing oxygen from molten chloride salt mixtures is carbochlorination. A eutectic mixture of KCl-LiCl was melted and purified in a flow of N_2 saturated by CCl_4 vapour for 4 hours at 800 °C. This process successfully resulted in the reduction of oxide impurity concentrations to approximately 3 ppm.

2.2.3 Pre-Oxidation Treatment

Pre-oxidation is a treatment applied to alloys to help enhance their protection through the growth of a homogeneous and compact oxide scale [12]. The developed oxide scale helps mitigate further oxidation during service, thus improving corrosion resistance. The tendency of the oxide scale to protect the metal from corrosion is related in part to the relative volumes of the oxide and metal, which is described by the Pilling-Bedworth (PB) ratio [57]. The Pilling-Bedworth ratio expresses the ratio of the volumes in Equation (2.23):

$$PB\ Ratio = \frac{A_o \rho_M}{A_M \rho_o} \qquad 2.23$$

where A_O is the molecular weight of the oxide (kg/k·mol), A_M is the atomic weight of the metal, ρ_O is the oxide density (kg/m^3), and ρ_M is the metal density (kg/m^3) [57]. Metals with PB ratios less than unity tend to have porous oxide layers that are unprotective, whereas metals with PB ratios greater than unity form protective oxide layers [57]. Table 2.2 displays common protective oxide scales researched for MSR and CSP systems with their respective PB ratios. The protective oxide layers of Al, Cr, and Si formers is discussed and analyzed further.

Table 2.2: Pilling-Bedworth ratios for metal oxides [57].

Metal	Oxide	PB Ratio
Al	Al_2O_3	1.29
Ni	NiO	1.69
Fe	FeO	1.69
Mn	MnO	1.76
Cr	Cr_2O_3	2.00
Si	SiO_2	2.14

Mathieu *et al.* [60] examined oxidation of Cr_2O_3 and Al_2O_3 forming alloys in dry air, air + H_2O, and Ar-H_2O. Surface observations indicated that the specimens exposed to water vapour atmospheres did not uniformly oxidize. This suggests that a dry oxidizing environment should be used in pre-oxidation treatments for the formation of dense and uniform oxide scales.

Ding *et al*. [5] investigated the pre-oxidation of Al_2O_3-forming alloys as a mitigation strategy against molten chloride salt corrosion. The alloys AF-1 (75.5Fe-8Al-16Cr-0.5Y) and AF-2 (75.5Fe-8Al-16Cr-0.5Zr) were heated to 800 °C for 15 h in a furnace to promote a protective oxide scale, then the treated alloys were immersed in molten NaCl-KCl-$MgCl_2$ at 700 °C for 500 h. Figure 2.6 (a) displays a BSE image of pre-oxidized AF-1 post-exposure, demonstrating the formation of a dense and uniform Al_2O_3 scale. Figure 2.6 (b) displays the EDS line scans through the cross-section of pre-oxidized AF-1 after immersion in the molten chloride salt mixture. There was an enrichment Mg at the surface of the alloy, but the Al_2O_3 scale effectively stopped the penetration of Mg into the matrix. No Cr depletion is evident in the cross-section of pre-oxidized AF-1 after immersion.

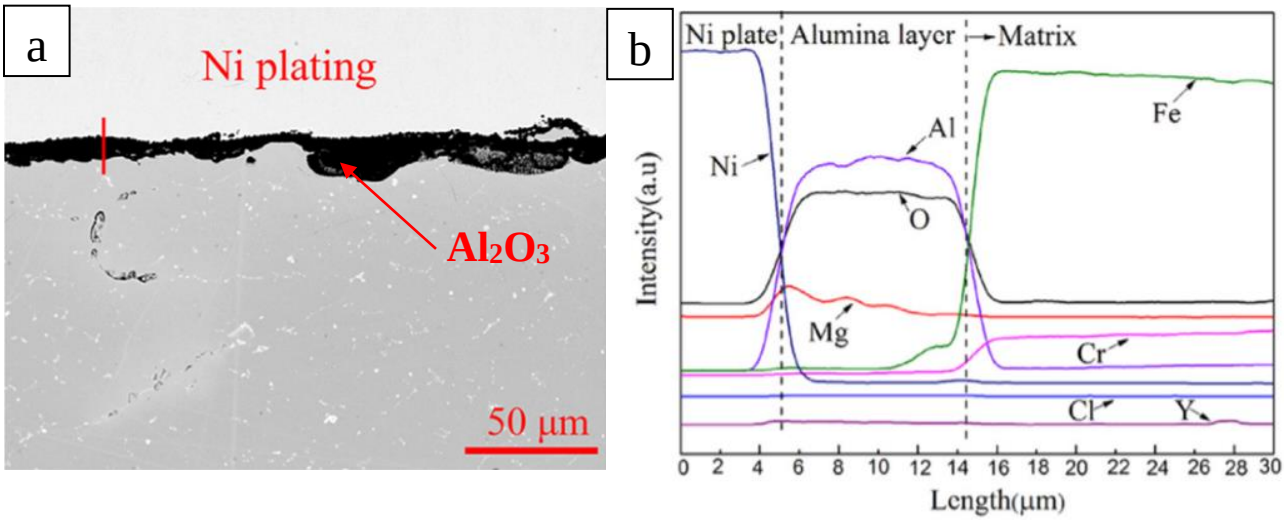

Figure 2.6: (a) BSE image of polished cross-section of AF-1 after immersion in molten NaCl-KCl-$MgCl_2$ at 700 °C for 500 h, and (b) EDS line scans through the cross-section of AF-1 post-exposure [5].

Vidal *et al.* [11] studied the pre-oxidation treatment of Al_2O_3 forming alloys as a corrosion mitigation strategy for molten chloride salt exposure. It was found that, of the various alloys tested, Inconel 702 (75Ni-15Cr-3Al-2Fe) produced the most protective Al_2O_3 scale. The scale consisted of two distinct zones: a denser layer on top, and thicker, dispersed inner layer. XRD analysis confirmed a crystalline polymorphic α-corundum phase. The authors explained that this phase is a very protective structure because it lacks crystalline defects. The worst performing alloy was Haynes 224 since the alloy formed mixed oxides consisting of Al, Cr, and Fe.

Israelsson *et al.* [58] investigated the pre-oxidation and corrosion of the Al_2O_3 forming Kanthal APMT (Fe-21Cr-5Al-3Mo) alloy. The pre-oxidized specimens were heated to 900 °C and 1100 °C for 1 and 24 h, then exposed to KCl solution that was sprayed on the specimens, then dried with flowing air. The KCl-coated samples were studied though isothermal exposures at 600 °C in a 5 % O_2 + 40% H_2O + 55 % N_2 environment for 24 h. The Al_2O_3 scales formed during pre-oxidation treatment for 1 h at 900 °C and 1100 °C were both unable to protect the alloy against corrosion due to breakaway oxidation that initiated at flaws of the oxide scale. These results demonstrate that a dense and continuous Al_2O_3 scale is required to provide sufficient protection to the alloy against molten chloride salt corrosion.

Abdullah *et al.* [59] studied the effect of pre-oxidized Cr_2O_3 forming alloys that were exposed to molten glass via electrochemical methods. The results showed that as-prepared alloys experienced severe corrosion, whereas the pre-oxidized samples developed a thick and adherent Cr_2O_3 scale that effectively hindered corrosion. It was also concluded that the solubility limit plays a major role in determining the ability of an oxide scale to provide protection to alloys. It was found that the dissolution of Cr_2O_3 occurs simultaneously with the growth, therefore corrosion protection depends on relative rates of both processes.

Pan *et al.* [61] investigated the corrosion of pre-oxidized Fe-Ni-Al-Cr alloys in molten KCl contaminated air. Severe degradation of the formed Cr_2O_3 scale due to the formation of chromate was observed, as shown in Equation (2.24):

$$4KCl + Cr_2O_3 + \frac{5}{2}O_2 \rightarrow 2K_2CrO_4 + 2Cl_2 \qquad 2.24$$

The equilibrium Cl_2 (g) partial pressure of Equation (2.24) is 10^{-5} atm [61]. This value is substantially higher than the value for Al_2O_3 (10^{-15} atm) and Fe_2O_3 (10^{-12} atm), as represented by Equation (2.25) and (2.26) respectively [61-62]:

$$2KCl + Al_2O_3 + \frac{1}{2}O_2 \rightarrow 2KAlO_2 + Cl_2 \qquad 2.25$$

$$2KCl + Fe_2O_3 + \frac{1}{2}O_2 \rightarrow 2KFeO_2 + Cl_2 \qquad 2.26$$

The high equilibrium Cl_2 (g) partial pressure of Cr_2O_3 implies that it is the more reactive oxide of the three considered with KCl, and Al_2O_3 is the least reactive. Kassim *et al.* [12] investigated pre-oxidation treatments of Hastelloy C22 that would develop a protective Cr_2O_3 chromia scale. It was found that the oxide scale thickness increases with the temperature of the pre-oxidation treatment. The most protective oxide scale of the pre-treatments applied was 1000 °C for 4 h, which coincided with the growth of a dense and adhering scale comprised of Cr_2O_3 and $MnCr_2O_4$. Pre-oxidation temperatures greater than 1000 °C resulted in an oxide scale that spalled due to the volatilization of Cr_2O_3 according to Equation (2.27):

$$Cr_2O_3(s) + \frac{3}{2}O_2(g) \rightarrow 2CrO_3(g) \qquad 2.27$$

These results suggest that the pre-oxidation temperature must be equal to or less than 1000°C to avoid the spallation of Cr_2O_3. Examination of the pre-oxidized Hastelloy C22 post-exposure via a field emission electron microscope revealed a loose and porous Cr_2O_3 scale with large crack structures. It was concluded that the instability of the Cr_2O_3 layer was due to the formation of K_2CrO_4 (s) as described in Equation (2.24). K_2CrO_4 (s) is not protective from a corrosion perspective because it has a high solubility in molten chloride salts [12, 63].

Li *et al.* [62] investigated corrosion of a Fe-15Cr-5Si alloy that had been pre-oxidized in air with a presence of solid KCl salt. Cross-sectional analysis of the alloy post-exposure via SEM revealed a double-layered oxide layer that included an external K_2CrO_4 scale, and an inner SiO_2 scale. It was concluded that the Cr_2O_3 scale transitioned into K_2CrO_4 via Equation (2.24), but the inner SiO_2 scale acted as an effective barrier that could repress the evolution of Fe oxides. More research is needed to fully understand how SiO_2 scales provides corrosion protection for high temperature alloys in molten chloride salt mixtures.

Table 2.3 displays the thickness of oxides formed on various alloys exposed to different pre-oxidation conditions for comparative purposes. Oxide scale thickness increases with and increase of temperature, and generally increases with an increase of exposure time.

Table 2.3: Comparison of alloys subjected to pre-oxidation treatments under various conditions.

Alloy	Time (h)	T (°C)	Oxide Thickness (μm)	Ref
Ni-30Cr	2	1100	2.5	59
Ni-8Al-28Cr	2	1100	10	59
AF-1 (Fe-8Al-16Cr-0.5Y)	15	800	1.1	5
Hastelloy C22 (Ni-21Cr-13Mo-4Fe)	4	800, 900, 1000, 1100	0.5, 2.2, 3.4, 7.1	12
Haynes 224 (Ni-20Cr-3Al-27Fe)	4, 8, 15	1050	5, 2, 2	11
Kanthal APMT (21Cr-5Al-70Fe)	8, 16, 20	950	2.5, 1, 4	11
Inconel 702 (75Ni-15Cr-3Ni-2Fe)	4, 8, 25	1050	1, 2, 2.5	11
Kanthal APMT (21Cr-5Al-70Fe)	24	1100	1.5	58
602CA (Ni-9Fe-24Cr-2.3Al)	48	950	0.5	58
Manaurite 40XO (Ni-26Fe-28Cr-1.6Al)	48	950	1.5	60
Inconel 693 (Ni-6Fe-29Cr-3.2Al)	48	950	1	60
Fe-15Cr-5Si	48	650	5	62

2.3 Research Objective

The main forms of corrosion for Fe-based and Ni-based alloys are in the form of electrochemical corrosion, and impurity driven corrosion. In molten chloride salt mixtures, Fe-based and Ni-based alloys will not form a passive oxide scale to inhibit corrosion. Corrosion of metals in molten chloride salt is driven by the nobility of the metal. Metals with higher negative Gibbs free energies of chloride formation are more likely to form a chloride compound and dissolve in the salt, therefore initiating corrosion by the selective oxidation and removal of the least noble component. Therefore, Cr is preferentially corroded, followed by Fe, and Ni.

The objective of this research project is to determine the relative corrosion performance of high temperature alloys with different protective scale forming tendencies when exposed to molten KCl-$MgCl_2$ salt mixture. The corrosion performance is investigated using two corrosion mitigation methods, relative to the unprotected (UP) case: chemical purification (CP) of the molten salt mixture by Mg metal additions to render it less corrosive, and thermal pre-oxidation (PO) of the alloys to render them less prone to corrosion.

3.0 Experimental Methods

3.1 Materials

Three high temperature alloys were chosen for investigation, which include Incoloy® 800H (Cr_2O_3-forming), HAYNES® 214 (Al_2O_3-forming) and NORAM SX™ (SiO_2-forming). The chemical compositions of the alloys, as specified in the mill certificates, are listed in Table 3.1. Incoloy® 800H (I800H) was provided in plate form (0.12 mm) by VDM Metals (Toronto, ON), HAYNES® 214 (H214) was provided in plate form (0.50 mm) by Haynes International (Cambridge, ON), and NORAM SX™ (SX) was provided in tube form (1.9 mm outer diameter × 1.6 mm inner diameter) by NORAM Engineering (Vancouver, BC). The relative high Al and Si content in H214 and SX, respectively, promotes the formation of thin and compact protective inner Al_2O_3 [64-68] and SiO_2 layers [62, 66, 69], underneath a Cr_2O_3-base scale during high temperature oxidation.

Table 3.1: Chemical compositions (wt.%).

Alloy	Ni	Fe	Cr	Mn	Si	Mo	Cu	Al	Ti	Co
I800H	30.7	Bal.	20.6	0.60	0.30	-	0.03	0.50	0.60	-
H214	Bal.	3.6	16.3	0.20	-	0.50	-	4.20	0.50	2.00
SX	19.2	Bal.	17.8	0.52	4.60	0.40	2.00	-	-	-

Square (10 mm × 10 mm) test coupons were cut out of the as-received I800H and H214 plates and ¼ rings segment test coupons (~15 mm x 5 mm) were cut out of the SX tube using a SiC blade in a precision cutter with a commercial cutting fluid (Cooli Additive Plus). All coupon surfaces were mechanically abraded to a 600 grit finish using SiC abrasive papers and water as a

lubricant, ultrasonicated for 15 minutes in deionized water, rinsed with ethanol and dried in lab air at room temperature and weighed using a digital balance with 0.1 mg precision prior to testing.

One coupon of each alloy was cold mounted in cross-section in epoxy, polished and etched to reveal the starting microstructure (procedure described in more detail later). Light optical microscopy (LOM) images of the starting microstructures are shown in Figure 3.1. All three alloys exhibit an equi-axed grain structure with relatively minor twinning. There is a notable difference in grain size between the alloys. The average grain sizes of H214, I800H, and SX (with 95 % confidence intervals), as measured using the ASTM E112-13 intercept procedure, are 45±3.4 µm, 138±5.6 µm, and 50±11.3 µm respectively. Large spherical particles are distributed along the grain boundaries and within the grains of I800H. Such particles are commonly observed in this alloy and characterization by SEM-EDS has revealed them to be either Ti-containing carbides, or nitrides [70-74].

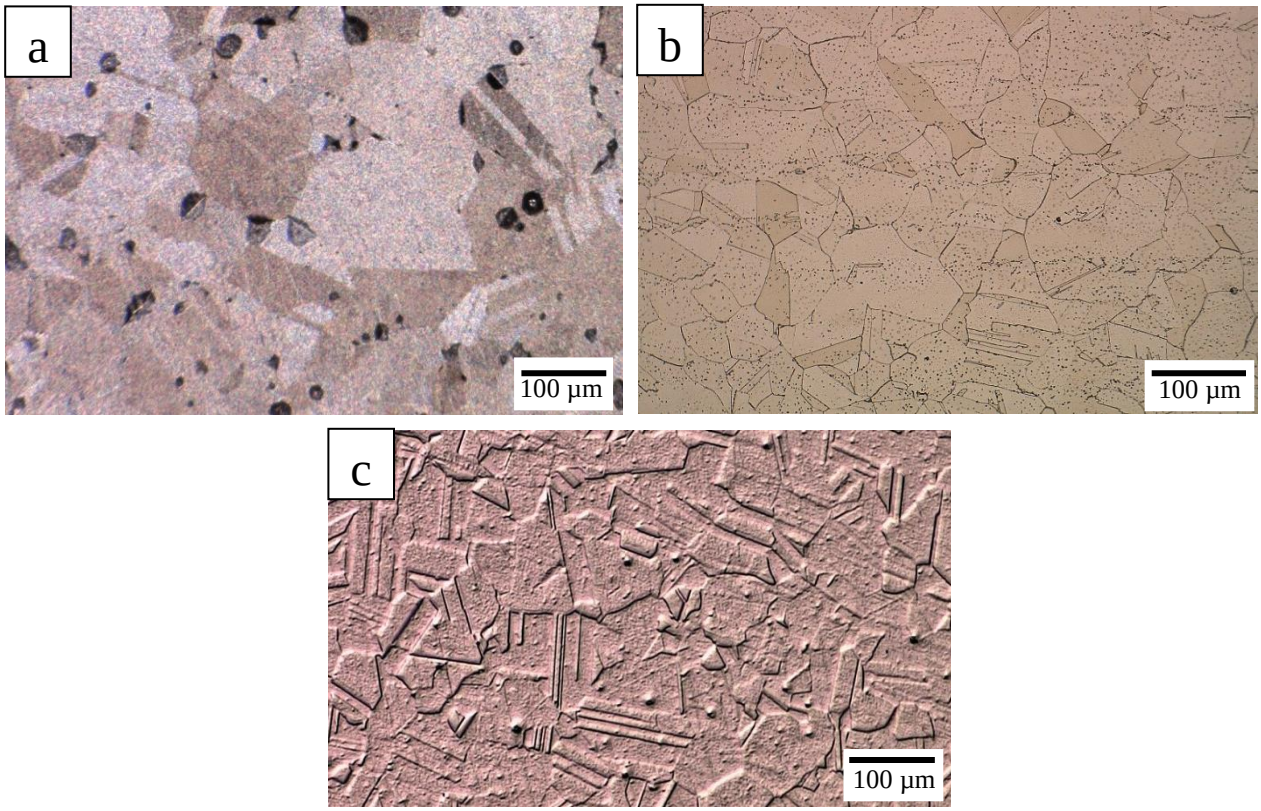

Figure 3.1: Starting microstructures of (a) I800H, (b) H214, and (c) SX.

3.2 Heat Treatment

Thermal pre-oxidation exposures in air at various temperatures and durations were conducted to grow a protective oxide scale on the surface of the three alloys as a corrosion control measure. A high temperature silicon carbide horizontal tube furnace and alloy test coupons were used for this purpose. Each alloy was subjected to three thermal pre-oxidization treatments, as listed in Table 3.2. Table 2.3 shows the wide range of temperatures and exposure times used for pre-oxidation treatments of high temperature alloys in literature. The treatments for this work were chosen based on these results published in literature that demonstrated effective oxide scales were developed on the experimental alloys used in this work [64-65, 75-79]. Of these three, one was selected to move forward with for corrosion testing in the molten KCl-$MgCl_2$ salt mixture. The qualitative criteria used for selection included the formation of a uniform, compact and adherent oxide scale, as judged from cross-sectional SEM images (procedure described in more detail later).

Table 3.2: Thermal pre-oxidation treatments.

Treatment	Time (h)	Temperature (°C)	Reference
1	2	1000	[58, 60, 80]
2	4	1000	[11, 60, 80]
3	24	800	[5, 62, 75-76]

Backscattered electron (BSE) cross-section images of the oxide scales formed on the alloys subjected to the three thermal pre-oxidation treatments are shown in Figure 3.2. Based on the qualitative criteria stated above, the following treatments were selected for corrosion testing: 4 h at 1000 °C for I800H (Figure 3.2(d)), 4 h at 1000 °C for H214, (Figure 3.2(e)), and 24 h at 800 °C for SX (Figure 3.2(i)). The selected Treatment 2 for I800H is not considered ideal since it also

produces intergranular oxidation (about 4 µm deep) in the alloy. Treatment 1 also produced intergranular oxidation in this alloy, but is much deeper (about 25 µm), whereas Treatment 3 produced a loose and cracked oxide scale, indicating a tendency for oxide spallation. Treatment 2 produced a layered oxide scale (thicker outer layer (bright)) on top of a thinner inner layer (dark)) consistent with the formation of an Al_2O_3 layer underneath a Cr_2O_3 layer [64-68]. Treatment 3 was the only treatment of the three to produce a crack-free oxide scale on SX.

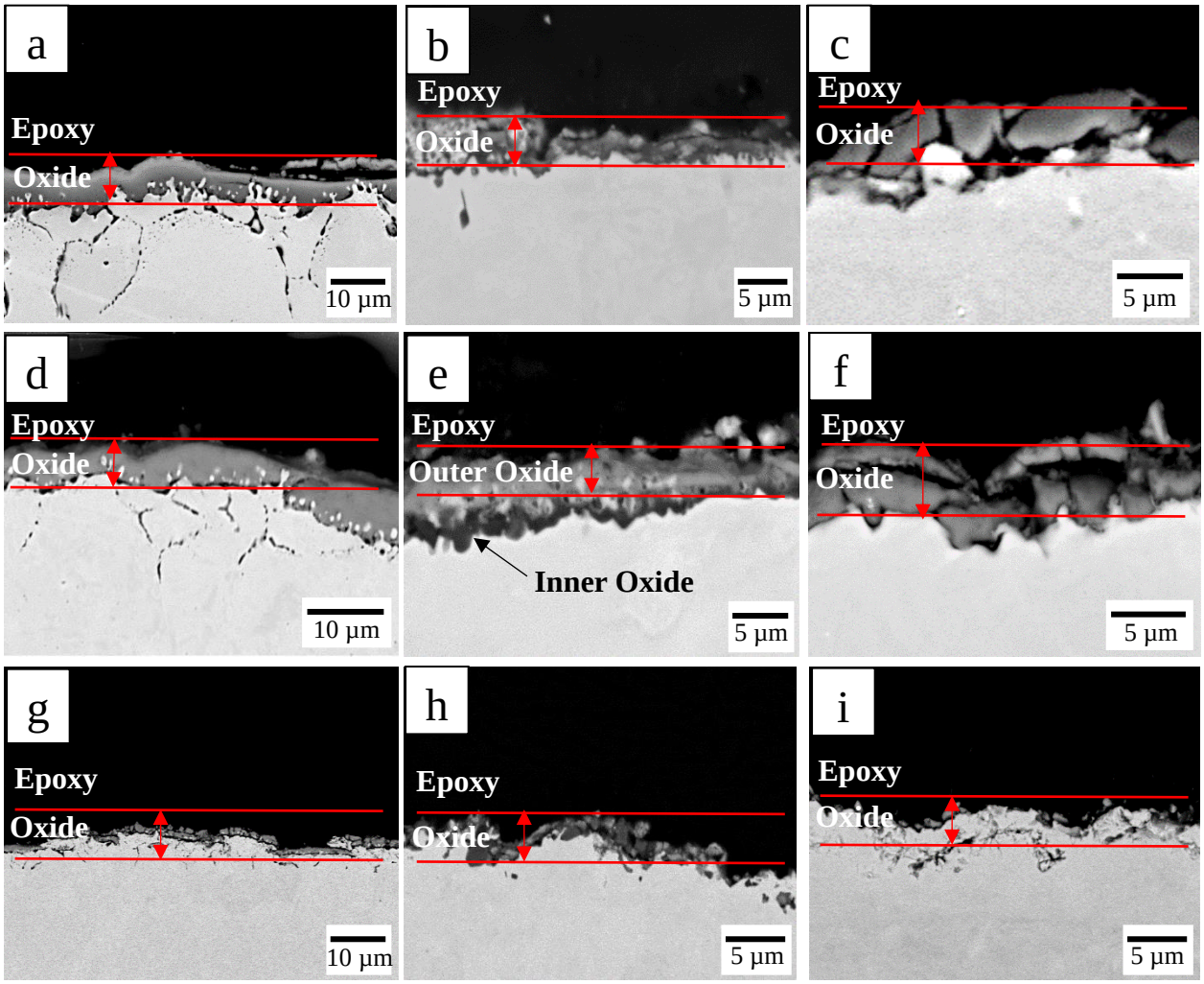

Figure 3.2: Cross-sectional BSE images after pre-oxidation treatment (in air) of I800H (a) 2 h at 1000 °C, (d) 4 h at 1000 °C, (g) 24 h at 800 °C, H214 (b) 2 h at 1000 °C, (e) 4 h at 1000 °C, (h) 24 h at 800 °C, and SX (c) 2 h at 1000 °C, (f) 4 h at 1000 °C, (i) 24 h at 800 °C.

3.3 Molten KCl-$MgCl_2$ Mixture

The salt mixture chosen for corrosion testing is 78.2 wt % KCl – 21.8 wt % $MgCl_2$ (dry basis), which is consistent with CSP and MSR applications [6, 20, 81-86]. Mixtures were prepared using reagent grade KCl and $MgCl_2 \cdot 6H_2O$ powder crystals. The mixture was thermally dehydrated *in-situ* during subsequent corrosion testing by using the thermal dehydration cycle shown in Figure 3.3, which was originally published by Kipouros *et al.* [31]. Two water molecules are driven off at 117 °C, two more are driven off at 180 °C, one more is driven off at 240 °C and the last one is driven off at 400 °C.

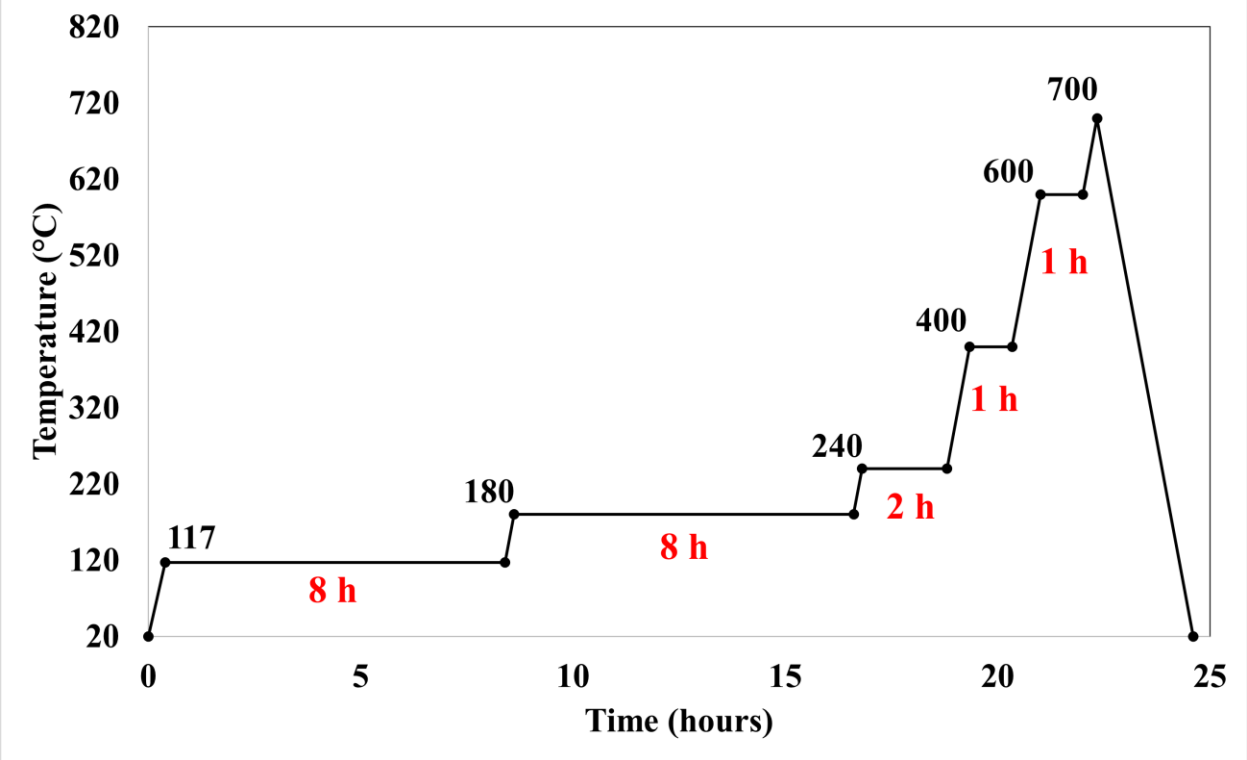

Figure 3.3: Temperature-time plot showing thermal dehydration cycle following procedure originally published by Kipouros *et al.* [31].

An XRD measurement (described in more detail later) was used to validate successful thermal dehydration using this thermal cycle. Figure 3.4 shows the XRD spectrum acquired from the KCl-$MgCl_2$ after being subjected to the thermal dehydration cycle. The experiment followed a typical corrosion test (procedure described in more detail later). Two clear sets of peaks are identified: one set belonging to KCl and another set belonging to $MgCl_2 \cdot 6H_2O$. $MgCl_2$ cannot be differentiated from $MgCl_2 \cdot 6H_2O$ due to overlapping peaks. Therefore, validation was based on a $MgCl_2$ proportion comparison before and after thermal dehydration. The proportion of $MgCl_2 \cdot 6H_2O$ in the starting salt mixture was 37.5%. After thermal dehydration, the proportion of $MgCl_2/MgCl_2 \cdot 6H_2O$ was 15%. The significant reduction indicates dehydration occurred. From a dry basis perspective, the proportion of $MgCl_2$ after thermal dehydration is lower than that expected before thermal dehydration (15% versus 21.5%). A lower value can be expected based on the hydrolysis reaction (Equation (2.2)) involving $MgCl_2$ as a reactant that are known to occur during thermal dehydration [5, 9-10, 31].

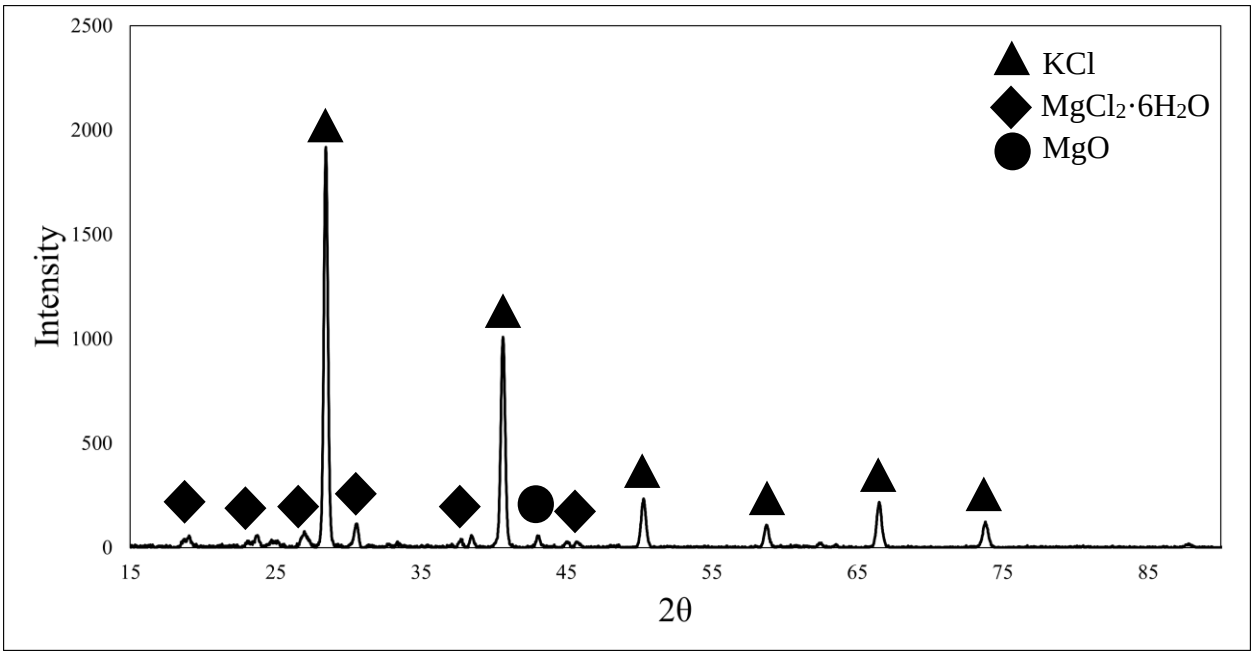

Figure 3.4: XRD spectrum acquired from KCl-$MgCl_2$ after being subjected to the thermal dehydration cycle.

Chemical purification of the molten salt mixture by additions of Mg metal as a sacrificial corroding metal was also conducted as a corrosion control measure. This was achieved by adding 1.7 wt % Mg (99.8% purity) chips to the starting KCl-$MgCl_2$ mixture: a value based on the research conducted by Zhao *et al.* [9].

3.4 Molten Salt Corrosion Testing

The apparatus used for corrosion testing in the molten KCl-$MgCl_2$ mixture is shown in Figure 3.5. Argon cover gas was transferred from the tank, through the gas regulator where it was converted to supply a constant rate of 1.48 cm/s to the stainless-steel gas inlet of the furnace. The gas was carried over a set of alumina crucibles placed on a rectangular alumina charge tray within a quartz glass tube inside the horizontal furnace (Thermocraft). Cylindrical, alumina crucibles (0.6 mL capacity, height: 14 mm, inner diameter: 9.5 mm) were purchased from Goodfellow Corporation (Coraopolis, Pennsylvania). The gas picked up any gaseous products associated with thermal dehydration and corrosion and carried them out of the furnace into a scrubber solution containing 1 M NaOH (aq). The scrubbed gas was then vented to atmosphere in a fume hood.

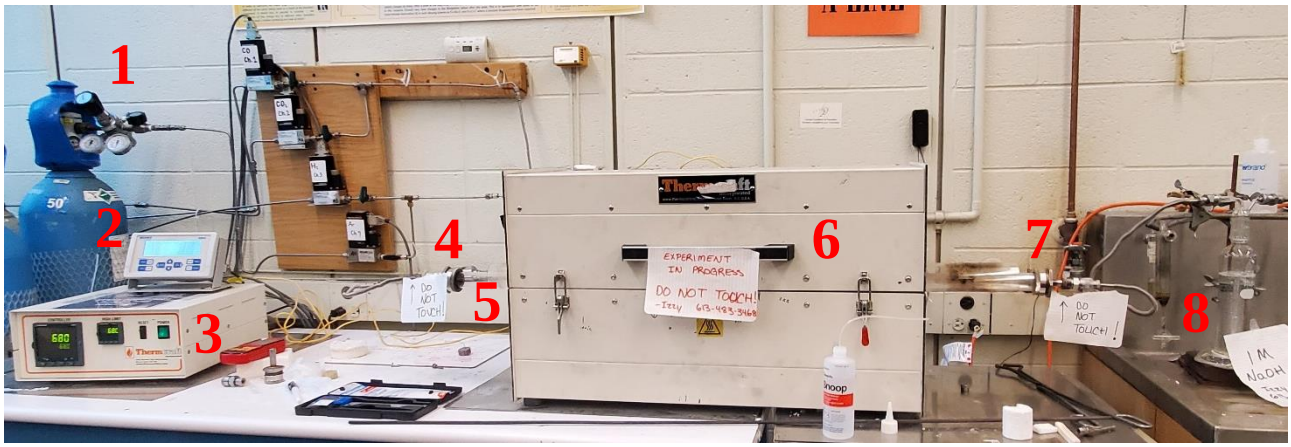

Figure 3.5: Photograph showing the apparatus used corrosion testing in the molten KCl-$MgCl_2$ mixture at 700 °C. 1: Ar gas tank. 2: Gas regulator. 3: Furnace controller. 4: gas inlet. 5: quartz tube. 6: Thermocraft furnace. 7: gas outlet. 8: NaOH scrubber.

Corrosion testing involved placing an alloy coupon into an alumina crucible containing the starting KCl-$MgCl_2$ mixture that was filled to capacity. The isothermal hot zone of the tube furnace permitted the use of six such crucibles in each test. Three crucibles contained a triplicate set of coupons immersed in the starting KCl-$MgCl_2$ mixture without Mg metal, added and the remaining three crucibles contained a second triplicate set of the coupons immersed in the starting KCl-$MgCl_2$ salt mixture with Mg metal added. Each alumina crucible was initially filled to 50% capacity with the starting KCl-$MgCl_2$ mixture, then the coupon, and Mg metal when required, was placed into the salt mixture and covered with the starting KCl-$MgCl_2$ mixture until the crucible was 100% filled. The total mass of the starting KCl-$MgCl_2$ mixture added to each crucible was about 0.54 g. When required, 0.01 g of Mg metal was added to each crucible. A set of photographs documenting this procedure is shown in Figure 3.6. The crucibles were 0.5 cm taller than the charge tray wall, and there was a 100 mm gap between the top of the crucibles, and the glass tube of the horizontal furnace. This gap was necessary to permit gas flow pattern over the crucibles, and therefore effective removal of water vapour and gaseous corrosion products. Alloys were tested with and without chemical purification (CP) by Mg metal addition and with and without thermal pre-oxidation (PO) as a corrosion control means. Thus, the comparative basis consists of three cases: (i) unprotected (UP): without CP or PO, (ii) protected by CP, (iii) protected by PO and (iv) protected by both CP and PO (CP+PO).

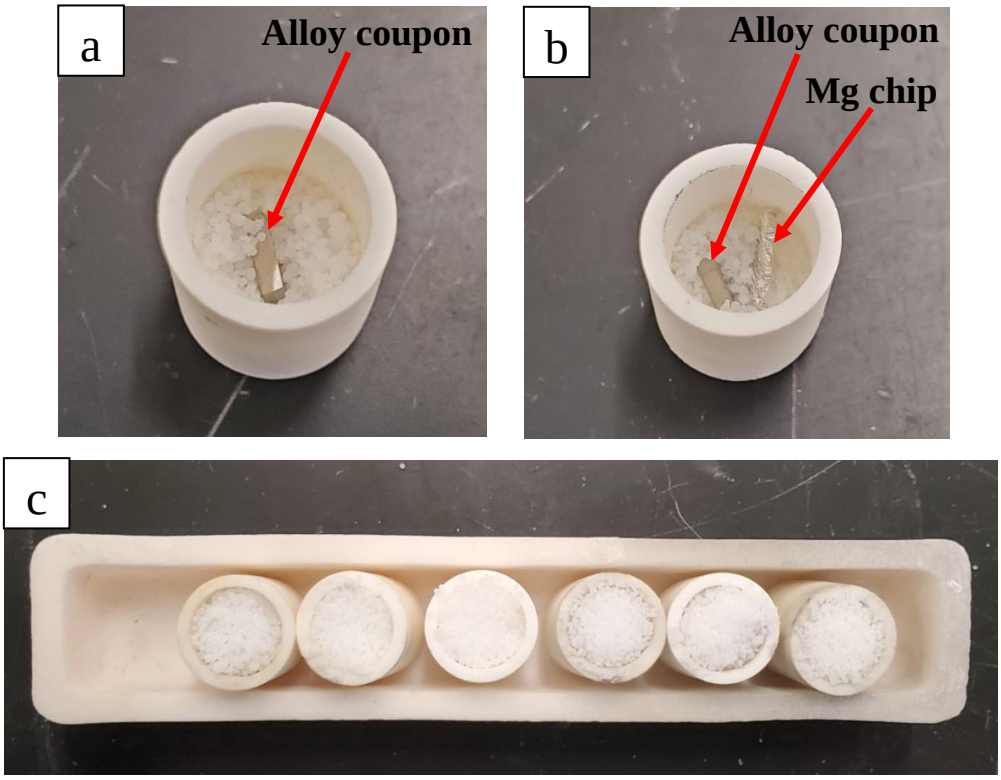

Figure 3.6: Photographs showing the steps involved in preparing the crucibles for corrosion testing: (a) coupon immersed in starting KCl-$MgCl_2$ mixture without Mg metal added, (b) coupon immersed in strating KCl-$MgCl_2$ mixture with Mg metal added and (c) arrangement of filled crucibles on charging tray.

The furnace dwelled at 700 °C for 100 h, then returned to room temperature. The stepwise heating procedure of the furnace for the corrosion exposure, complete with in-situ thermal dehydration is shown in Figure 3.7. Crucibles were taken from the furnace and the coupons were removed from the solidified salt mixture with tweezers. Extracted coupons were ultrasonicated for 15 minutes in deionized water to dissolve the bulk of the adhered solidified salt mixture from the surface prior to re-weighing.

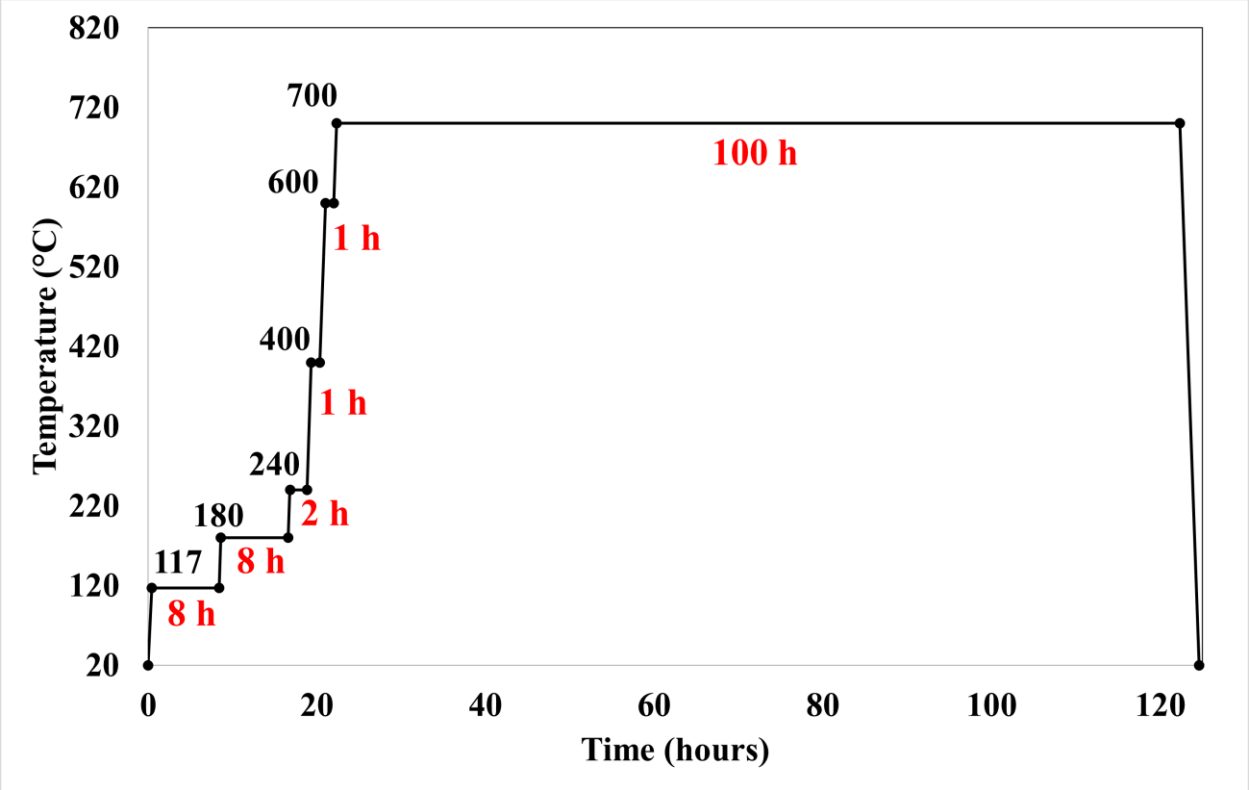

Figure 3.7: Temperature-time plot showing heating procedure for corrosion testing, complete with the initial in-situ thermal dehydration.

Crucibles were cleaned by first submerging them in boiling deionized water for 10 minutes. They were then submerged in reagent grade HCl (aq) for 5 minutes. The crucibles were dried for 30 minutes in a drying furnace at 150 °C. This was done after each corrosion test so that the crucibles could be reused. Each crucible was weighed before and after drying to ensure all moisture and salt deposits were removed.

3.5 Material Characterization Techniques

The materials characterization techniques that were used include LOM, SEM and associated EDS, XRD, and TEM and associated EDS of FIB-prepared samples. The objective being to determine links between near-surface structure and corrosion extent of the alloys exposed in the molten KCl-

$MgCl_2$ mixture at various length scales. Specific details pertaining to each technique are provided separately below.

Coupons (pre-and post-corrosion exposure) were sectioned using a SiC blade in a precision cutter and cold mounted in cross-section (exposing the rolling direction-normal direction RD-ND plane for the I800H and H214 plates and longitudinal direction-radial direction of the SX tube as the working surface) using epoxy. The H214 surface was ground with 320 grit SiC paper, and polished with 9 µm diamond, 3 µm diamond, and colloidal silica (OP-S) suspension. The SX and I800H surfaces were ground with 320, 400, 600, 800, and 1200 grit SiC abrasive paper and water as a lubricant, then polished with OPS suspension. Both SX and I800H are softer Fe-based alloys compared to the Ni-based H214, and therefore required a less aggressive polishing procedure.

For the LOM images of the starting microstructures, etching was done using a "chrome-regia" solution. The etchant was made by mixing one-part reagent grade H_2CrO_4 (aq), with one-part hot water, and three-parts reagent grade HCl (aq). The sample mounts were immersed face-up for approximately 1-3 s. Etched surfaces were observed under a Nikon Eclipse LV100 optical microscope.

Post-corrosion surfaces were imaged in plan-view and/or cross-section view (unetched) with a JEOL 6610LV scanning electron microscope operated using an acerating voltage of 20 keV and working distance of 10 mm. Both BSE and secondary electron (SE) imaging modes were used. BSE imaging was used to reveal information about composition and contrast, whereas SE imaging was used to analyze surface morphology and topography.

Element distribution maps and line scans of the scale/alloy interface in cross-section were acquired using SEM-EDS. An Oxford X-max 20 mm^2 silicon drift detector equipped as part of the

JEOL 6610LV SEM microscope was used for this purpose. Line scans and element distribution maps were taken at three locations for each sample. The three common major alloying elements include Cr, Ni, and Fe. The Kα energies are approximately 5.4 keV for Cr, 7.5 keV for Ni, and 6.4 keV for Fe [87]. Typically, a beam energy double the highest Kα of the elements being analyzed is required [87], therefore an accelerating voltage of 20 keV was used at a working distance of 10 mm.

XRD was used to determine the crystalline composition of the sample of interest (salt mixture after thermal dehydration and surface scale formation after corrosion testing). A sample of the dehydrated salt mixture was carefully transferred to a glass capillary and immediately sealed using epoxy to minimize re-hydration. The encapsulated dehydrated salt mixture was then analyzed using the Bruker Smart6000 CCD Cu source instrument. An acquisition time of 5 h was used to yield strong peak intensities. The entire coupon was used for the XRD analysis of the surface scale composition. A Bruker D8 Discover Co source instrument was used for this purpose. An acquisition time of 1 h was used to yield strong peak intensities.

A Zeiss NVision 40 dual beam microscope with a Ga source was used to mill a thin cross-sectional foil of SX surface after both thermal pre-oxidation and molten salt corrosion testing for TEM analysis. Electron beam deposition was used to apply a protective coating overtop of the area of interest that was approximately 100 nm thick to ensure enough protection during FIB milling. This was followed by ion beam deposition. Electron beam deposition was applied first because it is less damaging than ion beam deposition. Additional thinning of the cross-sectional foil was done using a lower voltage to reduce Ga implantation and amorphization of the surface. A Talos 200X analytical transmission electron microscope equipped with an X-FEG source was used for cross sectional analysis of FIB-prepared SX surface cross sectional foils. An accelerating voltage of 200

kV was used. Super X-detectors were used for EDS analysis for elemental mapping and line scans. A dwell time of 30 minutes for EDS maps were used to ensure sufficient resolution.

4.0 Results

4.1 Molten Salt Chemistry Validation

The composition of the as-received salt mixture is 62.5 wt% KCl-37.5 wt% $MgCl_2 \cdot 6H_2O$. The composition of the as-received salt mixture was measured by XRD to establish a baseline and the result is represented by 'Baseline Wet' in Table 4.1. After the as-received salt was treated to the thermal purification procedure, the chemical composition of the salt changed to 85 wt% KCl-15 wt% $MgCl_2 \cdot 6H_2O$ without chemical purification, and 78 wt % KCl-17.6 wt% $MgCl_2 \cdot 6H_2O$ -4 wt% MgO with chemical purification. The theoretical dry composition of the as-received salt mixture was calculated by eliminating the hexahydrate to validate that the thermal purification procedure effectively removed the H_2O from the mixture and is represented by 'Baseline Dry' in Table 4.1. The thermally purified salt without chemical purification has a chemical composition very similar to the calculated baseline dry composition. This suggests that the thermal purification procedure is successfully driving off the H_2O from $MgCl_2$. 4 wt % MgO was detected in the composition of the thermally purified salt with chemical purification. When the Mg inhibitor reacts with $MgOH^+$, MgO is produced as described by Equation (2.22). This reaction is assumed to go to completion, therefore the amount of MgO present in the thermally dehydrated salt with chemical purification corresponds to the amount of Mg dissolved.

Table 4.1: Compositions of salt mixture measured by XRD under various conditions.

Sample	KCl (wt %)	$MgCl_2 \cdot 6H_2O$ (wt %)	MgO (wt %)
Baseline Wet	64	36	-
Baseline Dry	78.04	21.96	-
Without Chemical Purification	85	15	-
With Chemical Purification	78	18	4

Figure 4.1 displays the XRD spectrum of KCl-$MgCl_2$ salt subjected to the thermal dehydration cycle with chemical purification (added Mg metal). The phases identified are KCl, $MgCl_2 \cdot 6H_2O$, and MgO.

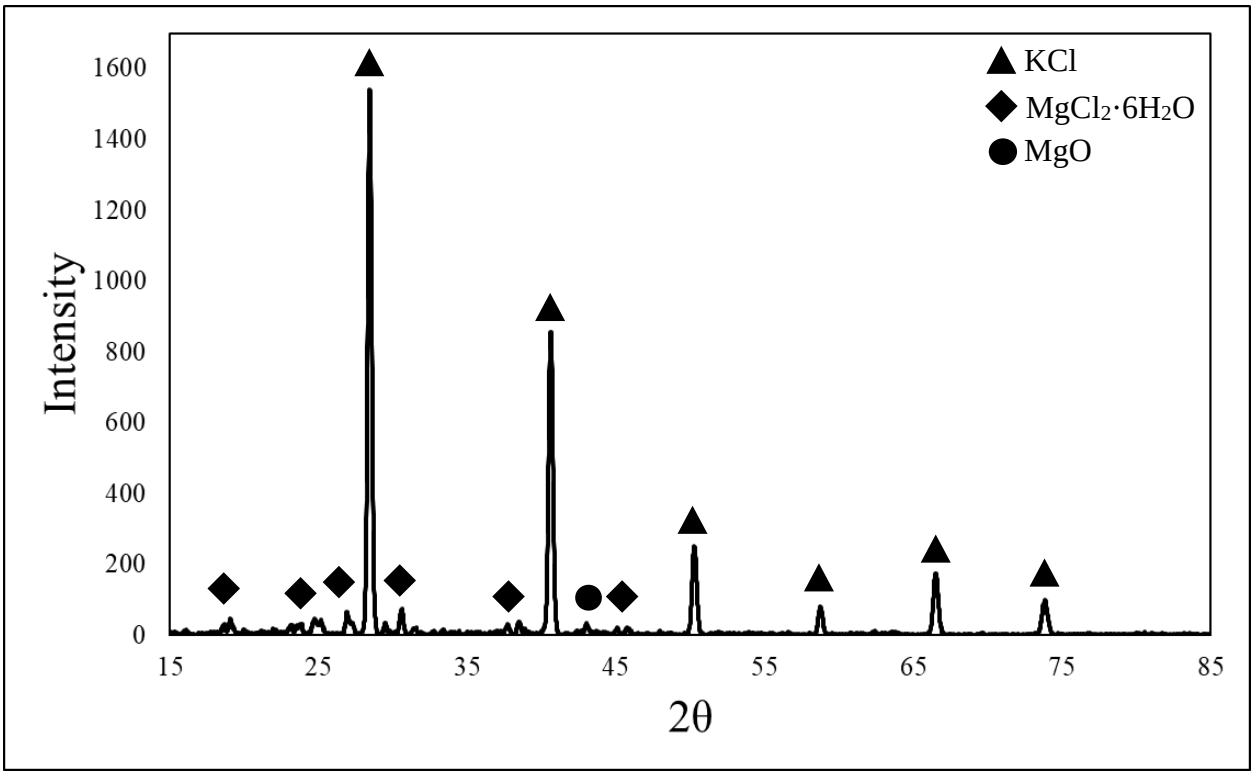

Figure 4.1: XRD spectrum acquired from KCl-$MgCl_2$ after being subjected to thermal dehydration cycle with chemical purification.

4.2 Pre-Oxidation Treatments

4.2.1 I800H

Figure 4.2 displays a BSE image of the oxide scale formed after 4 h at 1000 °C and an associated set of EDS elemental line scans acquired across the oxide/scale interface. The EDS line scans reveal an oxide scale that is enriched in Cr and Mn and depleted in Fe and Ni, relative to the alloy.

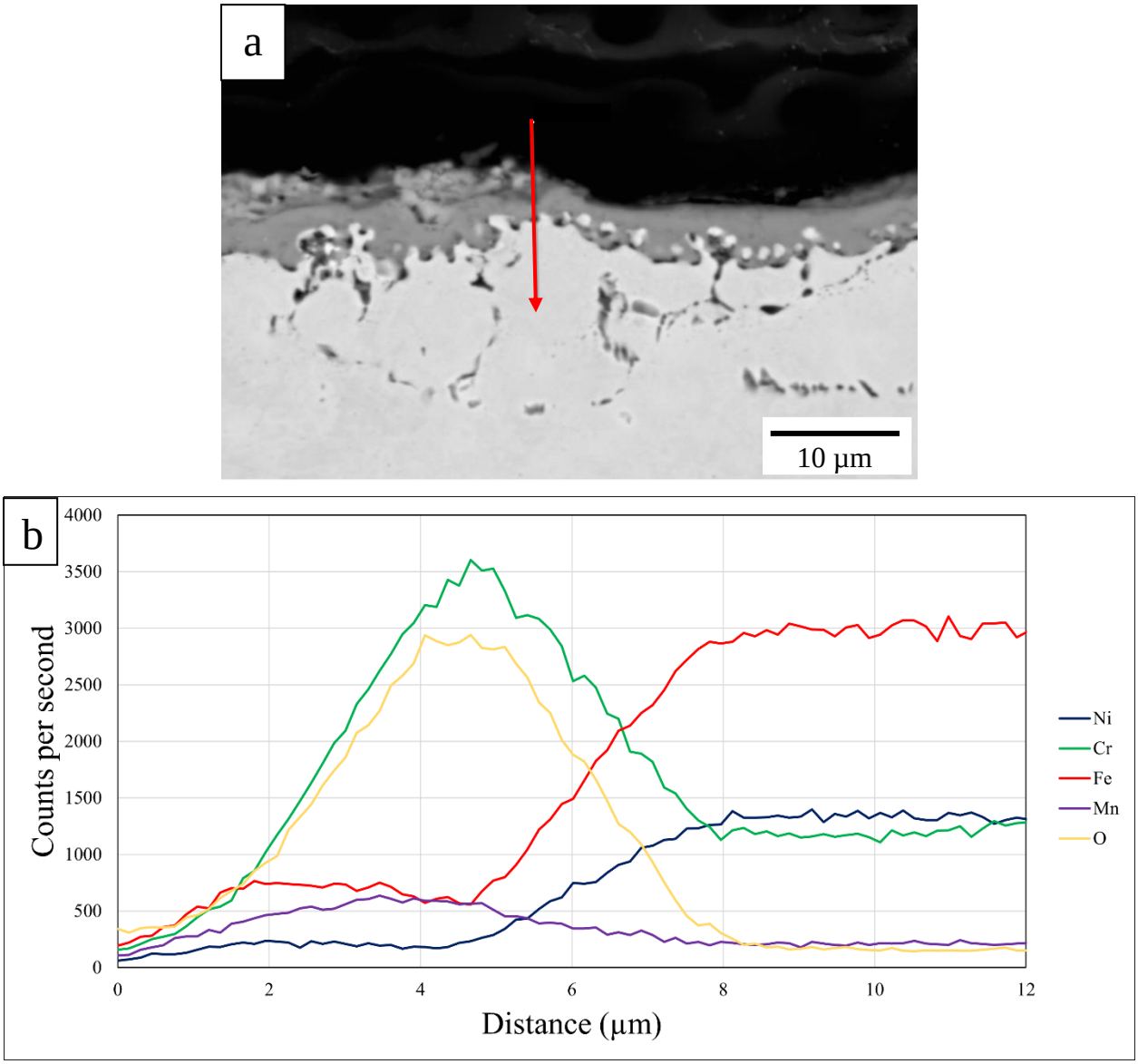

Figure 4.2: (a) BSE cross-sectional image of the oxide scale formed on I800H after thermal pre-oxidation at 1000 °C for 4 h (Treatment 2) showing location of the EDS line scan, and (b) set of elemental EDS lines scans acquired across the oxide/alloy interface.

4.2.2 H214

Figure 4.3 displays a BSE image of the oxide scale formed after 4 h at 1000 °C and an associated set of EDS elemental line scans acquired across the oxide scale/alloy interface. The line scans reveal two distinct layers: an inner layer composed of Al and O as major scale forming elements, and an outer layer enriched in Cr, Ni, Al, and O.

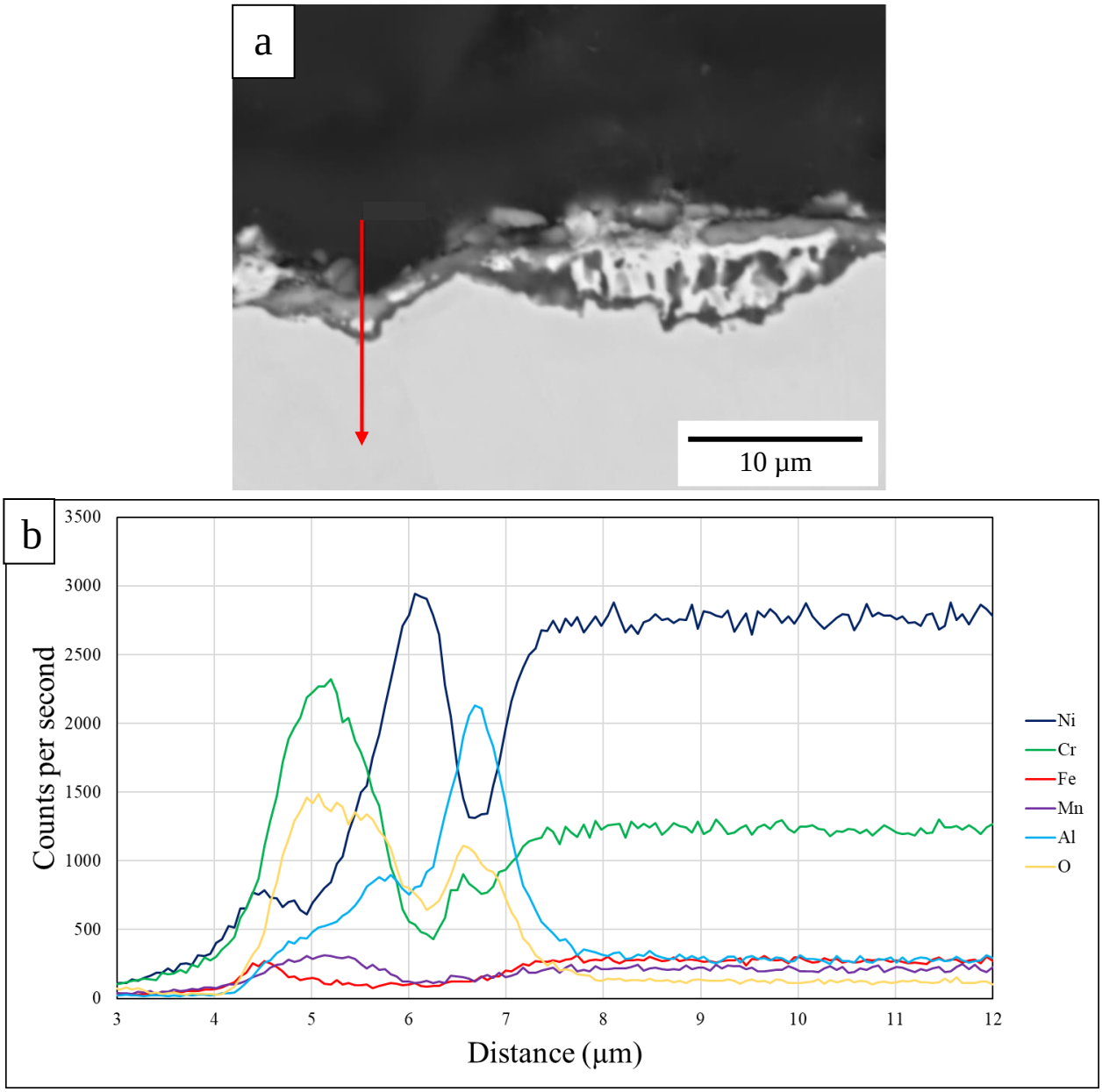

Figure 4.3: (a) BSE cross-sectional image of the oxide scale formed on H214 after thermal pre-oxidation at 1000 °C for 4 h (Treatment 2) showing location of the EDS line scan, and (b) set of elemental EDS lines scans acquired across the oxide/alloy interface.

4.2.3 SX

SEM-EDS was unable to identify the presence of an inner silica scale in the cross-section of the SX sample pre-oxidized at 800 °C for 24 h, therefore STEM-EDS was used for this purpose. Figure 4.4 (a) displays the oxide scale formed on SX after 24 h at 800 °C which is composed of large polyhedral-shaped crystals and fine particles. Figure 4.4 (b) displays the thinned cross-section of SX that was prepared for TEM examination.

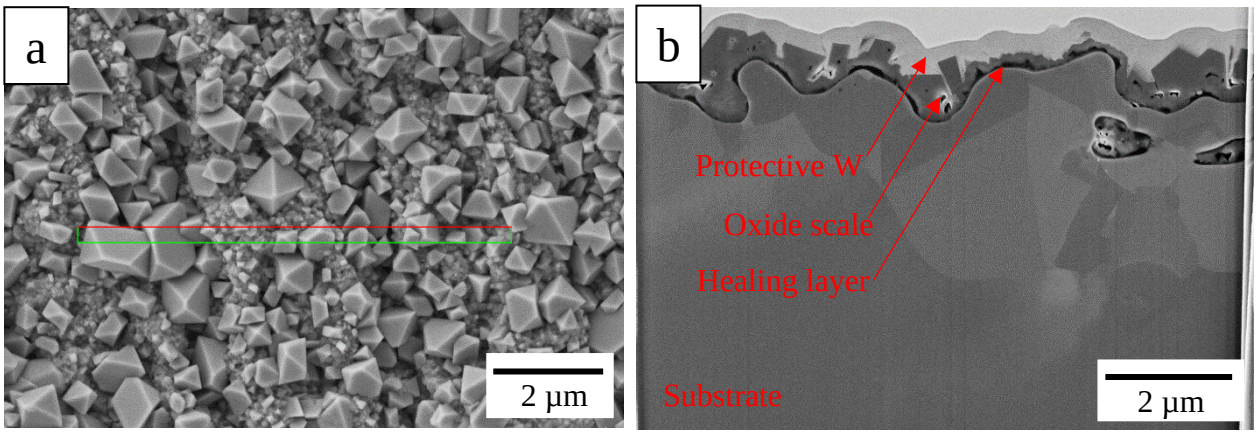

Figure 4.4: Plan view (a) and cross-section view (b) SI image of the oxide scale formed on SX after thermal pre-oxidation at 800 °C for 24 h (Treatment 3).

Figure 4.5 presents the STEM-EDS line scans that were acquired across the oxide/alloy interface after oxidation at 800 °C for 24 h. The set of scans revealed a bi-layered structure: a thicker outer layer (about 1 um thick) residing on a much thinner inner layer (about 100 nm thick). The outer layer consisted of Cr and O as major scale forming elements, whereas the inner consisted of Si and O as major scale forming elements.

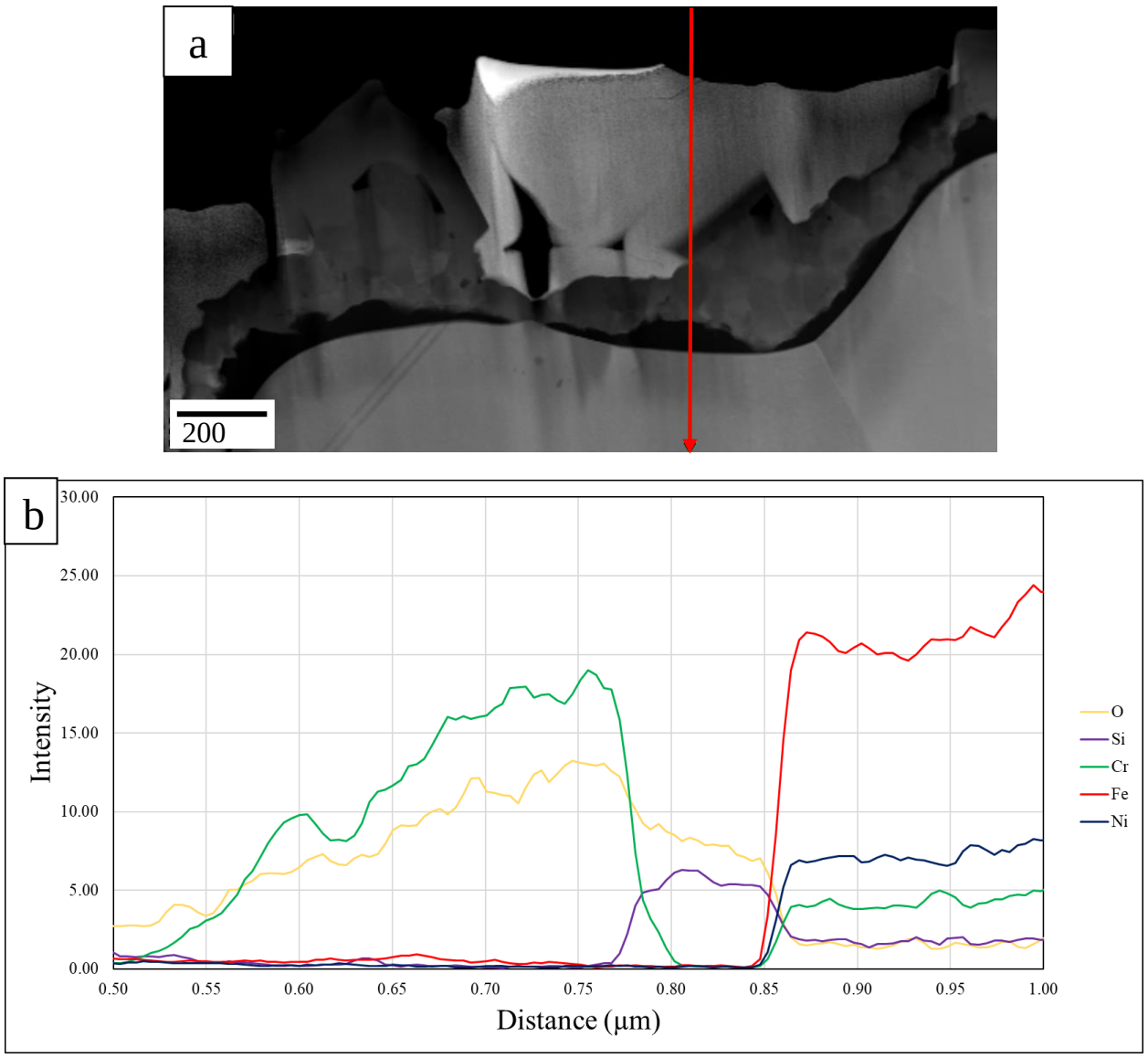

Figure 4.5: (a) BSE cross-sectional image of the oxide scale formed on SX after thermal pre-oxidation at 800 °C for 24 h (Treatment 3) showing location of EDS line scan, (b) set of elemental EDS lines scans acquired across the oxide/alloy interface.

4.3 Molten Salt Exposure Experiments

Figure 4.6 displays the crucibles filled with the salt mixture and alloy specimens before and after the molten salt exposure experiment. The crucibles were filled to 100 % capacity before the exposure experiment as displayed in Figure 4.6 (a). After the exposure experiment, the crucibles were filled to approximately 25% salt capacity as shown in Figure 4.6 (b), suggesting that the residual water in the salt evaporated during the exposure experiment. The crucibles that had additions of a Mg corrosion inhibitor were covered in black residue after the corrosion experiment indicating evidence of a reaction between Mg and the salt/alloys. These results were consistent in each molten salt expsoure experiment.

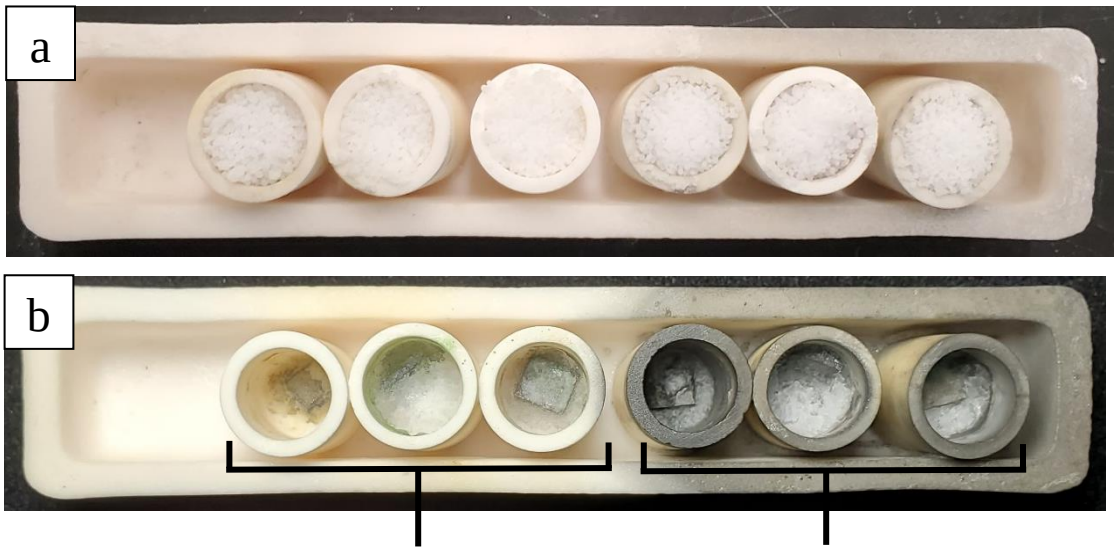

Figure 4.6: (a) crucibles filled with KCl-$MgCl_2$ salt and alloy specimens before corrosion exposure, and (b) crucibles filled with KCl-$MgCl_2$ salt and alloy specimens after corrosion exposure.

4.3.1 I800H

Figure 4.7 displays unprotected and pre-oxidized I800H before and after exposure to molten chloride salts, with and without chemical purification. The unprotected specimen exposed without chemical purification has darkened regions suggesting areas of corrosion. The unprotected specimen exposed with chemical purification has a uniform surface. The pre-oxidized sample exposed without chemical purification has a clean oxide scale. The pre-oxidized sample exposed with chemical purification has two distinct regions: a lighter region and a darker region.

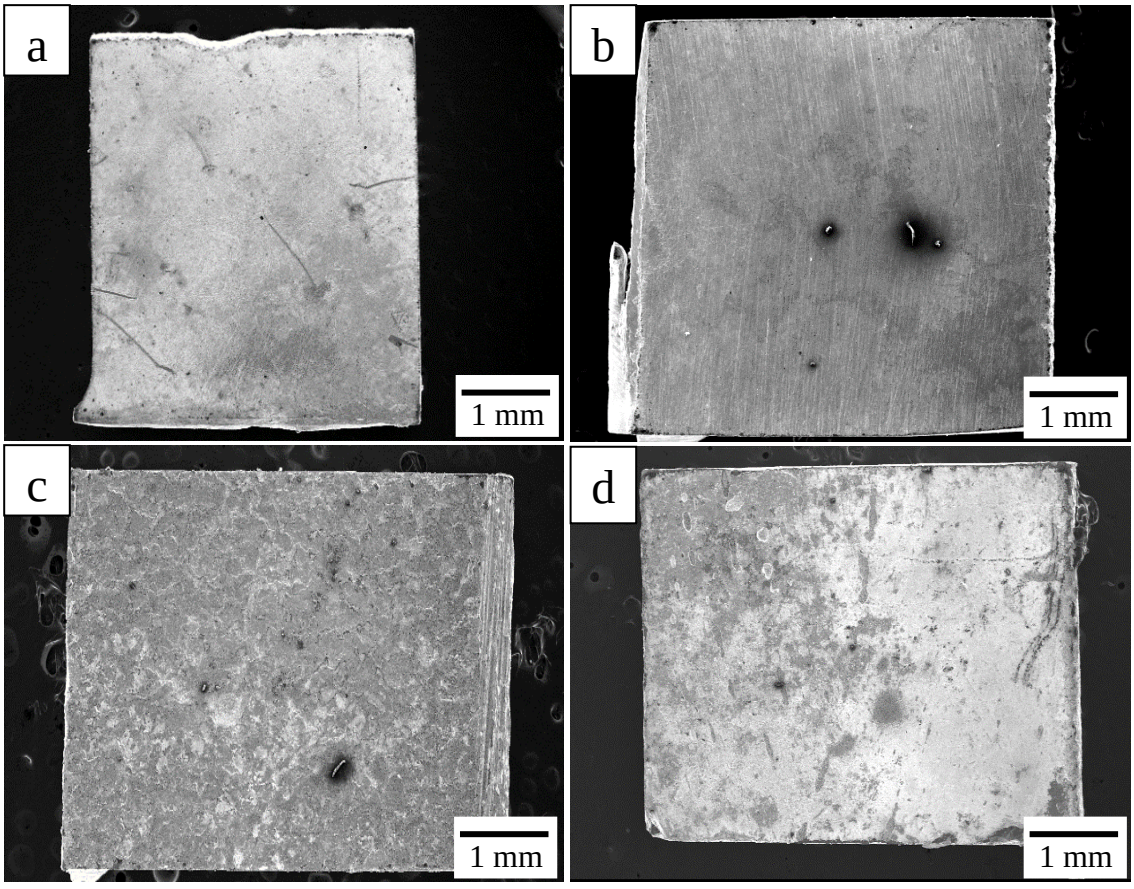

Figure 4.7: Plan view SE images showing the typical appearance of the I800H surface after immersion in molten KCl-$MgCl_2$ at 700 °C for 100 h and subsequent de-salting: (a) UP, (b) CP, (c) PO and (d) PO+CP.

Figure 4.8 displays the average mass loss of the triplicate I800H specimens that were exposed to molten chloride salt in presence and in absence of a Mg corrosion inhibitor. Standard deviation bars that are unique to each condition were calculated using 95% confidence intervals and are included for each corrosion control measure. The mass loss for unprotected I800H is 0.8 mg/cm^2. I800H has a mass gain of 0.4 mg/cm^2 when chemical purification was added to the salt mixture. This suggests that a Mg species precipitated onto the surface of the alloy during exposure. The mass loss of I800H was reduced by 100 % when a Mg corrosion inhibitor was included in the salt mixture. The significant reduction of mass loss when chemical purification is included suggests that the Mg preferentially reacted with the corrosive impurities and as a result, reduced the corrosion attack on the alloy. The mass loss of pre-oxidized I800H is 0.85 mg/cm^2 without chemical purification and 0.08 mg/cm^2 with chemical purification. The mass loss of pre-oxidized I800H was reduced by 90.6 % when a Mg corrosion inhibitor was included in the salt mixture. The mass loss is greater for the pre-oxidized alloy compared to the as-received alloy. This suggests that the chromia scale does not provide sufficient protection to the alloy against the molten chloride.

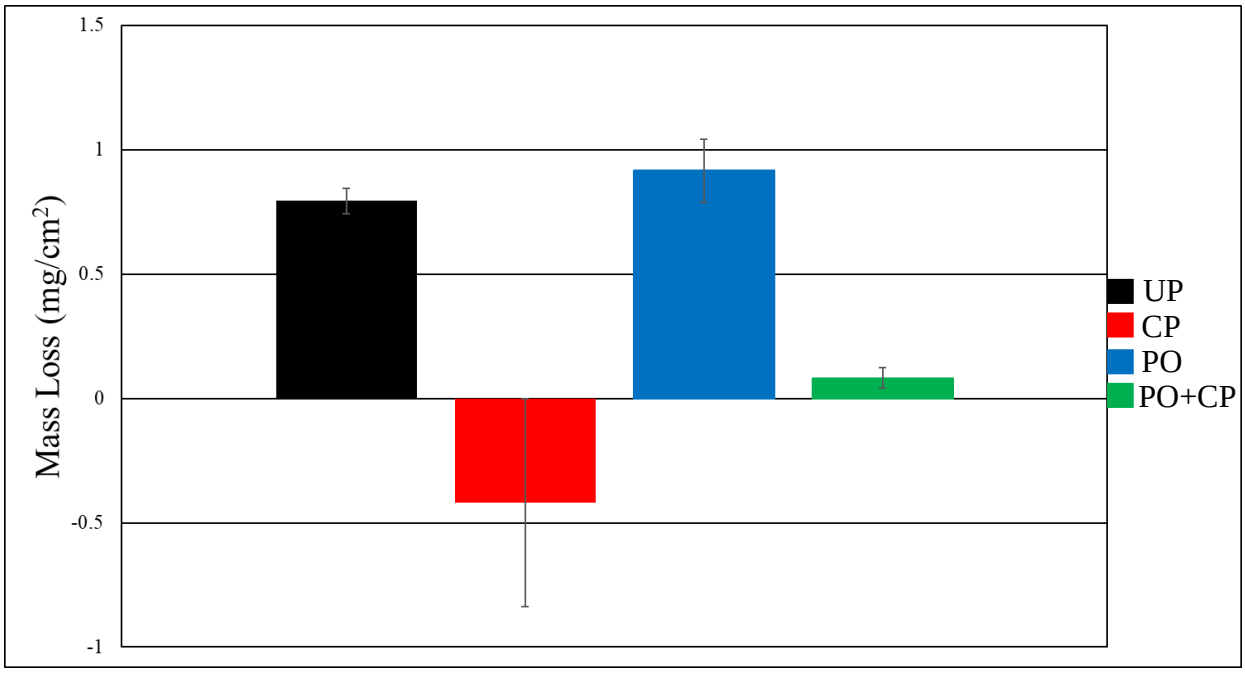

Figure 4.8: Average mass loss of I800H coupons after immersion in molten KCl-$MgCl_2$ at 700 °C for 100 h and subsequent de-salting.

Figure 4.9 displays the XRD patterns of unprotected and pre-oxidized I800H exposed to molten chloride salt with and without chemical purification. XRD measurements indicated that unprotected I800H consists of an austenite face centered cubic (FCC) phase. XRD analysis of I800H with chemical purification revealed the same austenite phase, as well as MgO. The XRD measurements of pre-oxidized I800H show three phases of austenite, chromium iron oxide, and $MgCrMnO_4$. The XRD pattern reveals the same austenite phase, as well as a MgO, and a ferrite body centered cubic (BCC) phase for the pre-oxidized sample immersed with chemical purification. These measurements verify that MgO is precipitating onto the surface of unprotected and pre-oxidized I800H when chemical purification is included in the salt mixture, which causes the sample to gain mass. The higher mass loss of the pre-oxidized sample without chemical purification could be a result of the instability of the chromia layer due to the formation of

$MgCrMnO_4$. The austenite peak of I800H exposed with chemical purification has shifted significantly to the right compared to the austenite peaks of the other sample conditions.

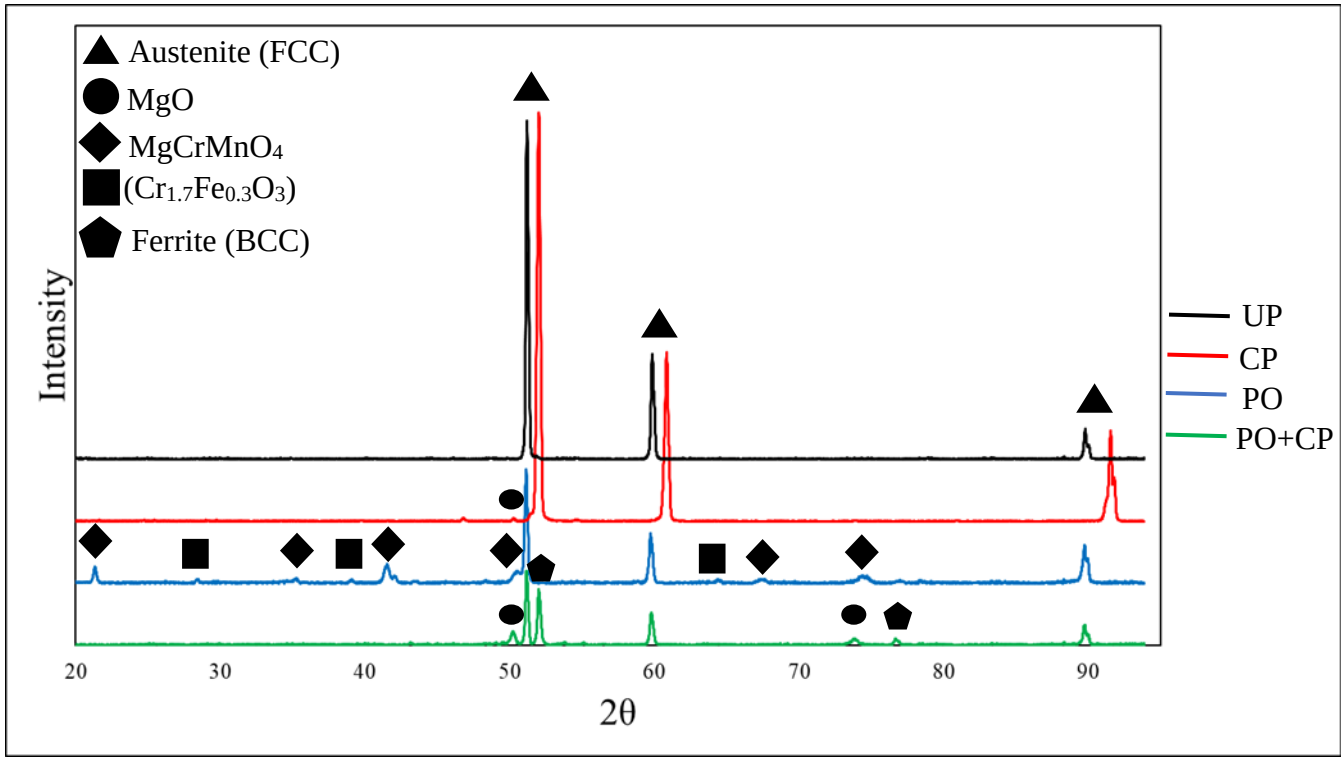

Figure 4.9: XRD spectra acquired from I800H surfaces after immersion in molten in molten KCl-$MgCl_2$ at 700 °C for 100 h and subsequent de-salting.

Figure 4.10 displays the plan-view SE images of unprotected and pre-oxidized I800H after immersion in molten chloride salts with and without chemical purification. The surface of unprotected I800H displays evidence of localized corrosion due to the presence of uniformly distributed pores that range from <1 µm to 3 µm in size. The surface of I800H with chemical purification no longer has pores but a dense surface that is covered in small, spherical structures. The surface of pre-oxidized I800H has areas of a clean oxide scale, as well as a darker region devoid of polyhedral-shaped crystals. The surface of pre-oxidized I800H after exposure with chemical purification has a clean oxide scale consisting of polyhedral-shaped crystals.

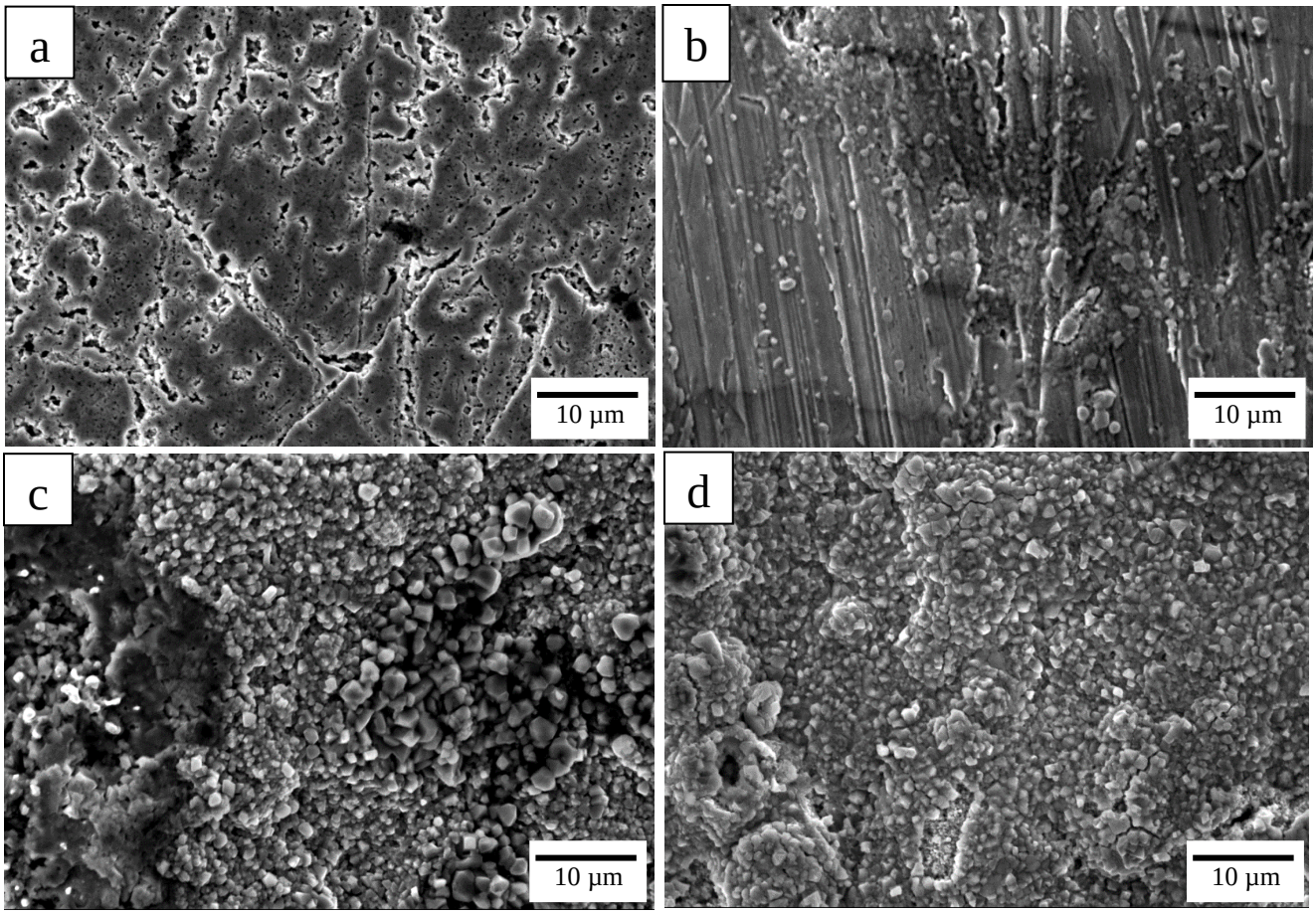

Figure 4.10: Plan-view SE images of I800H surfaces after immersion in molten KCl-$MgCl_2$ at 700 °C for 100 h and subsequently de-salting: (a) UP, (b) CP, (c) PO and (d) PO+CP.

Figure 4.11 below displays the EDS elemental maps of the cross-section of unprotected I800H after exposure to molten KCl-$MgCl_2$ at 700 °C for 100 hours. A 2 µm thick layer composed of Mg and O is present on the surface of the sample. Underneath the Mg and O layer, a porous and uniform corrosion layer is observed. Cr and Mn were both depleted 15 µm from the substrate. Both Fe and Ni were unaffected by the corrosion exposure and show no signs of depletion. Mg and O are detected as far as 5 µm into the substrate. There is an enrichment of Si and O at the surface of the cross-section, and an enrichment of Al and O in between the corroded layer and the substrate indicating the preferential oxidation of these alloying elements. Trace amounts of Cl is present in the sample substrate.

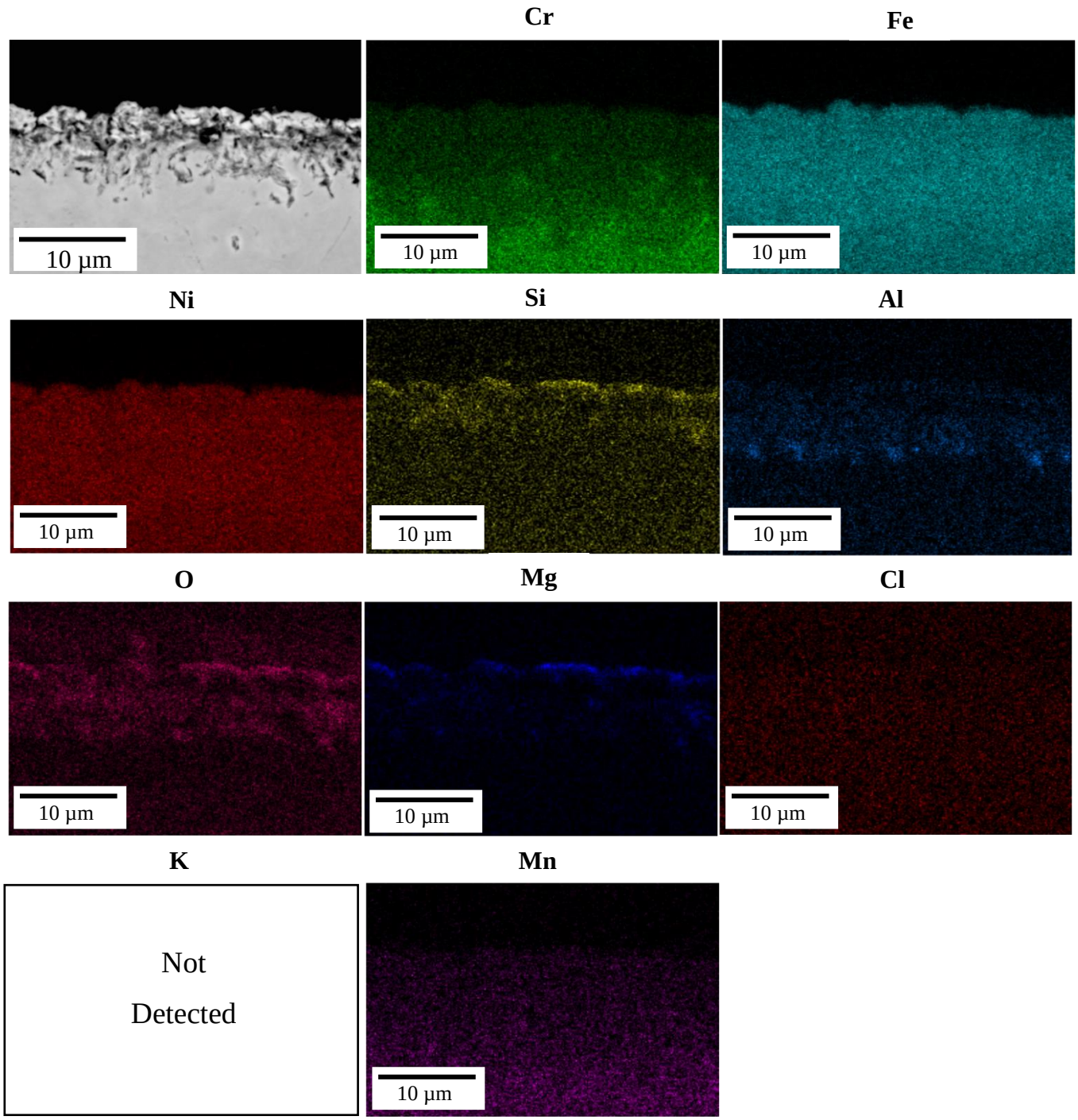

Figure 4.11: BSE cross-sectional image, and associated EDS elemental maps, of the I800H UP surface after immersion in molten KCl-$MgCl_2$ at 700 °C for 100 h and subsequent de-salting.

Figure 4.12 below displays the cross-section of I800H after exposure to molten chloride salts with chemical purification additions. Cr and Mn no longer show signs of depletion when chemical purification is added to the salt mixture. Fe and Ni remain unaffected by the exposure. A 5 µm thick O layer is present at the surface of the alloy, and Mg is no longer detected in the sample. Al and Si are evenly distributed throughout the sample substrate. Cl and K were not detected in the cross-section.

Figure 4.13 displays the EDS elemental maps of the cross-section of pre-oxidized I800H after corrosion exposure. The thickness of the chromia scale before exposure was 5 µm thick after pre-oxidation treatment. The chromia scale is 3.5 µm thick after exposure to molten chloride salt, therefore 1.5 µm of the chromia scale dissolved into the salt mixture. Complete dissolution of the chromia scale left an area of exposed substrate. Cr has been depleted form the grain boundaries due to intergranular oxidation extending 29 µm into the alloy. The intergranular oxidation extended 14 µm into the substrate after pre-oxidation treatment, therefore intergranular oxidation attack extended 15 µm deeper after exposure. Mg and O are identified within the chromia scale and are found as deep as 32 µm into the substrate. In the regions where Mg is found in the substrate, there is a depletion of Cr, Fe, and Ni. Ni and Fe remain unaffected by the exposure except for the two regions where Mg is found beneath the oxide layer. There is an enrichment of Si in the oxide layer, and an enrichment of Al between the oxide scale and the substrate. Trace amounts of Cl are detected in the cross-section.

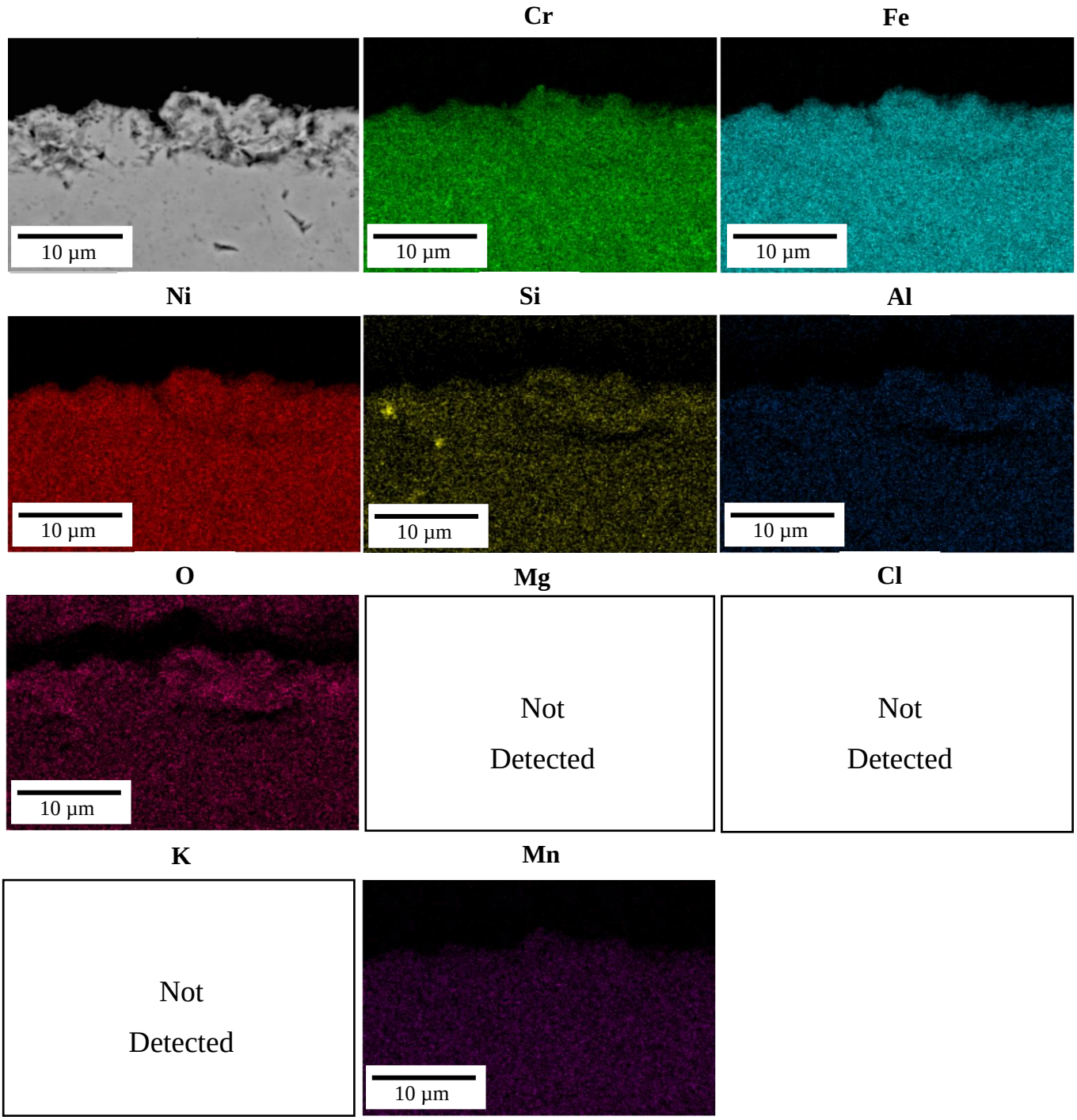

Figure 4.12: BSE cross-sectional image, and associated EDS elemental maps, of the I800H CP surface after immersion in molten KCl-$MgCl_2$ at 700 °C for 100 h and subsequent de-salting.

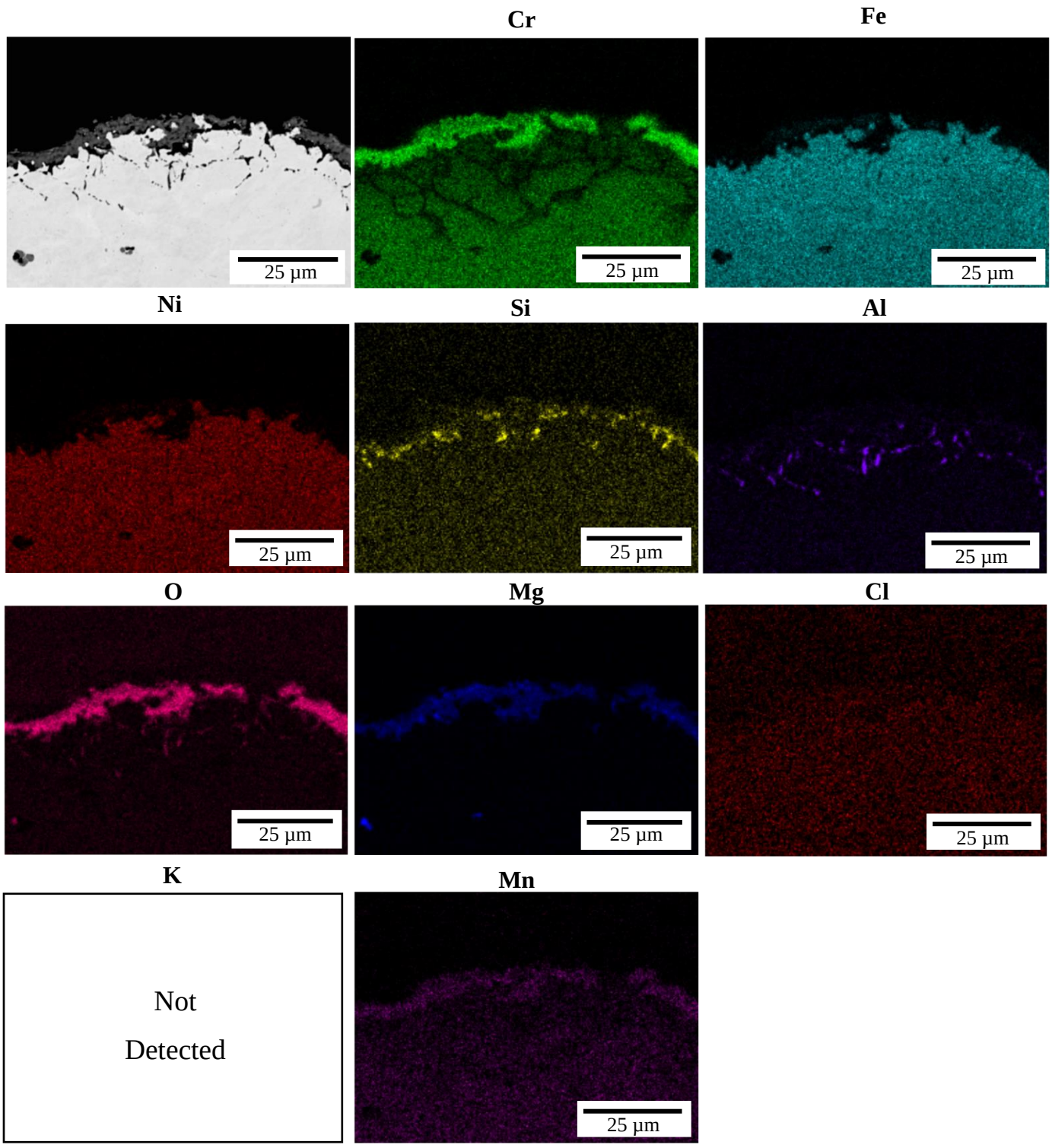

Figure 4.13: BSE cross-sectional image, and associated EDS elemental maps, of the I800H PO surface after immersion in molten KCl-$MgCl_2$ at 700 °C for 100 h and subsequent de-salting.

Figure 4.14 presents the EDS elemental maps of the cross-section of pre-oxidized I800H after exposure to molten chloride salt with the addition of a Mg corrosion inhibitor. The Cr oxide layer is approximately 5 μm thick meaning that the oxide scale remained the same thickness after exposure. Mg and O are prominent in the Cr oxide scale and are found as deep as 10.5 μm into the substrate. In the regions where Mg is found in the substrate, Cr, Ni, and Fe are depleted. There is also an enriched Mg and O layer on the outer surface of the alloy. The intergranular oxidation extends 14 μm into the substrate. The deepest depth of intergranular oxidation measured in this specimen is the same depth of the intergranular oxidation measured after pre-oxidation treatment, indicating that the intergranular attack did not extend further after exposure. O is found to extend out linearly, suggesting that it is following the path of the intergranular oxidation that developed during pre-oxidation treatment. Al is found along the grain boundaries in the same regions that oxygen is found beneath the oxide layer. Trace amounts of Cl are present in the cross-section.

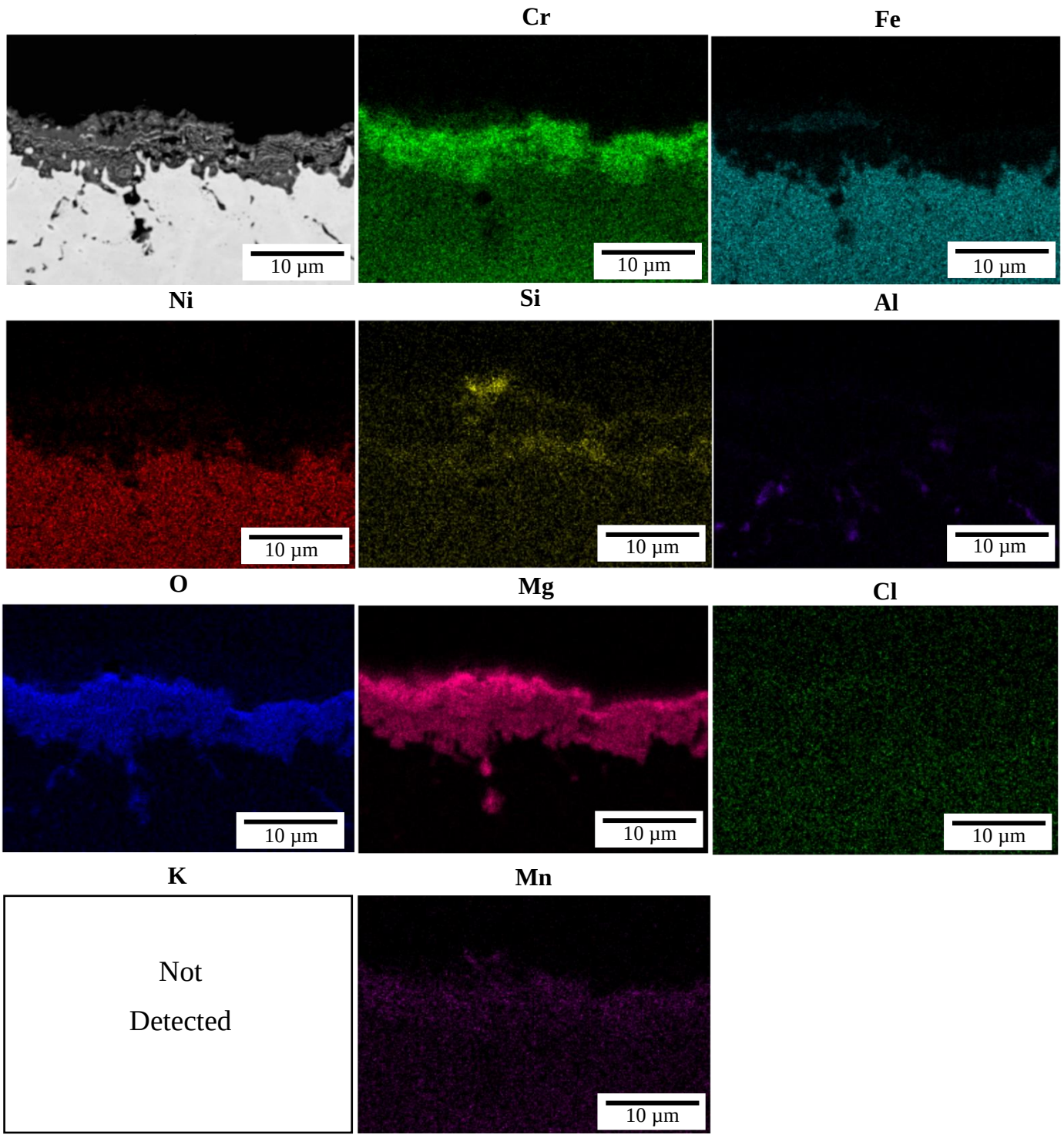

Figure 4.14: BSE cross-sectional image, and associated EDS elemental maps, of the I800H PO+CP surface after immersion in molten KCl-$MgCl_2$ at 700 °C for 100 h and subsequent de-salting.

Figure 4.15 displays the EDS depth profiles through the cross-section of UP I800H. Cr is depleted 20 µm from the surface. Al, Mg, and O are enhanced at the sites of internal oxidation, with the deepest site being 12 µm into the alloy.

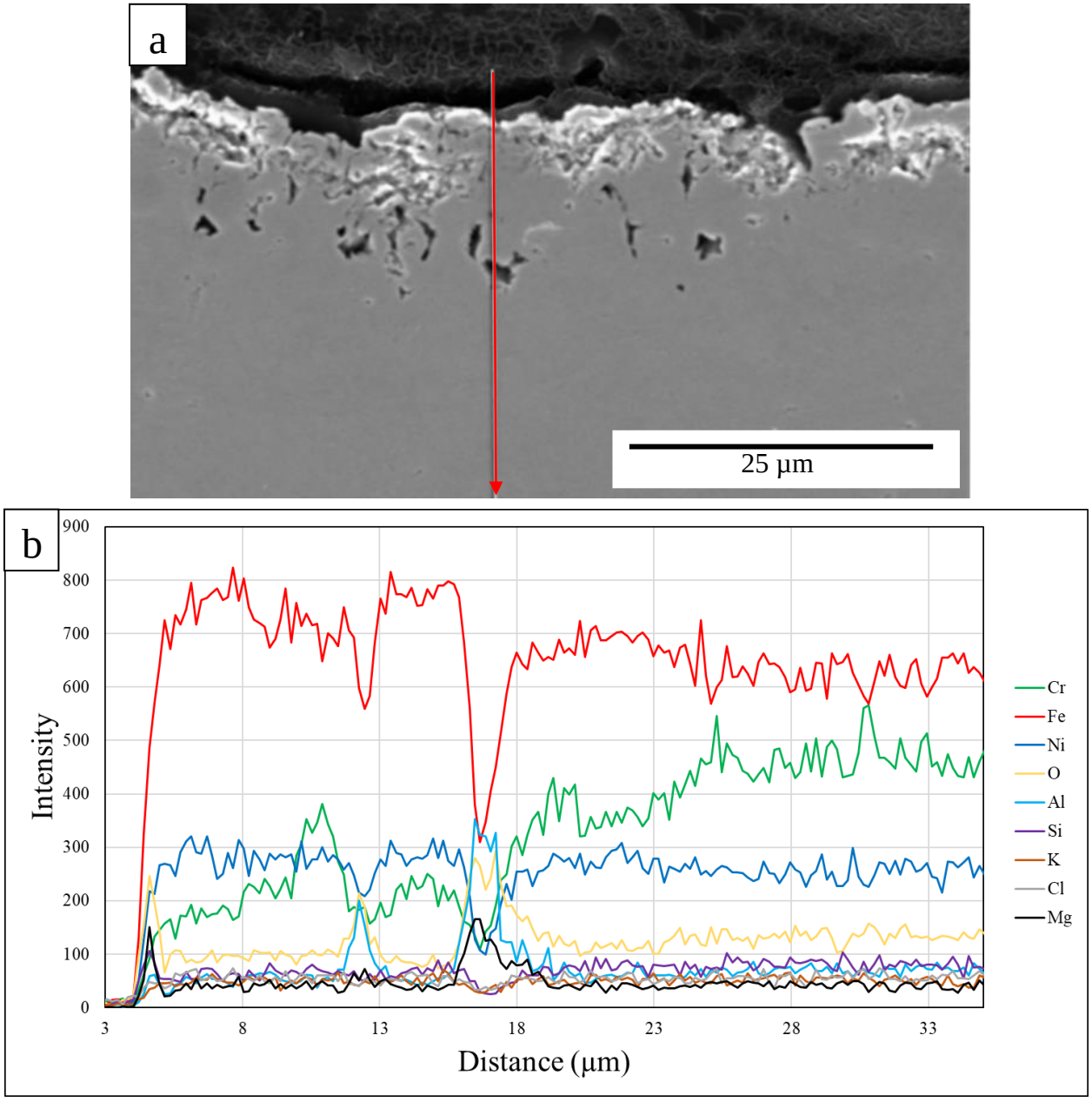

Figure 4.15: (a) BSE cross-sectional image of UP I800H after immersion in molten chloride salt mixture at 700 °C for 100 h showing location of the EDS line scan, and (b) set of elemental EDS lines scans acquired through the cross-section.

Figure 4.16 displays the EDS depth profiles through the cross-section of CP I800H. Cr is depleted 6 µm from the surface. Mg is not enriched at the surface and a 5 µm thick layer of O is present at the surface.

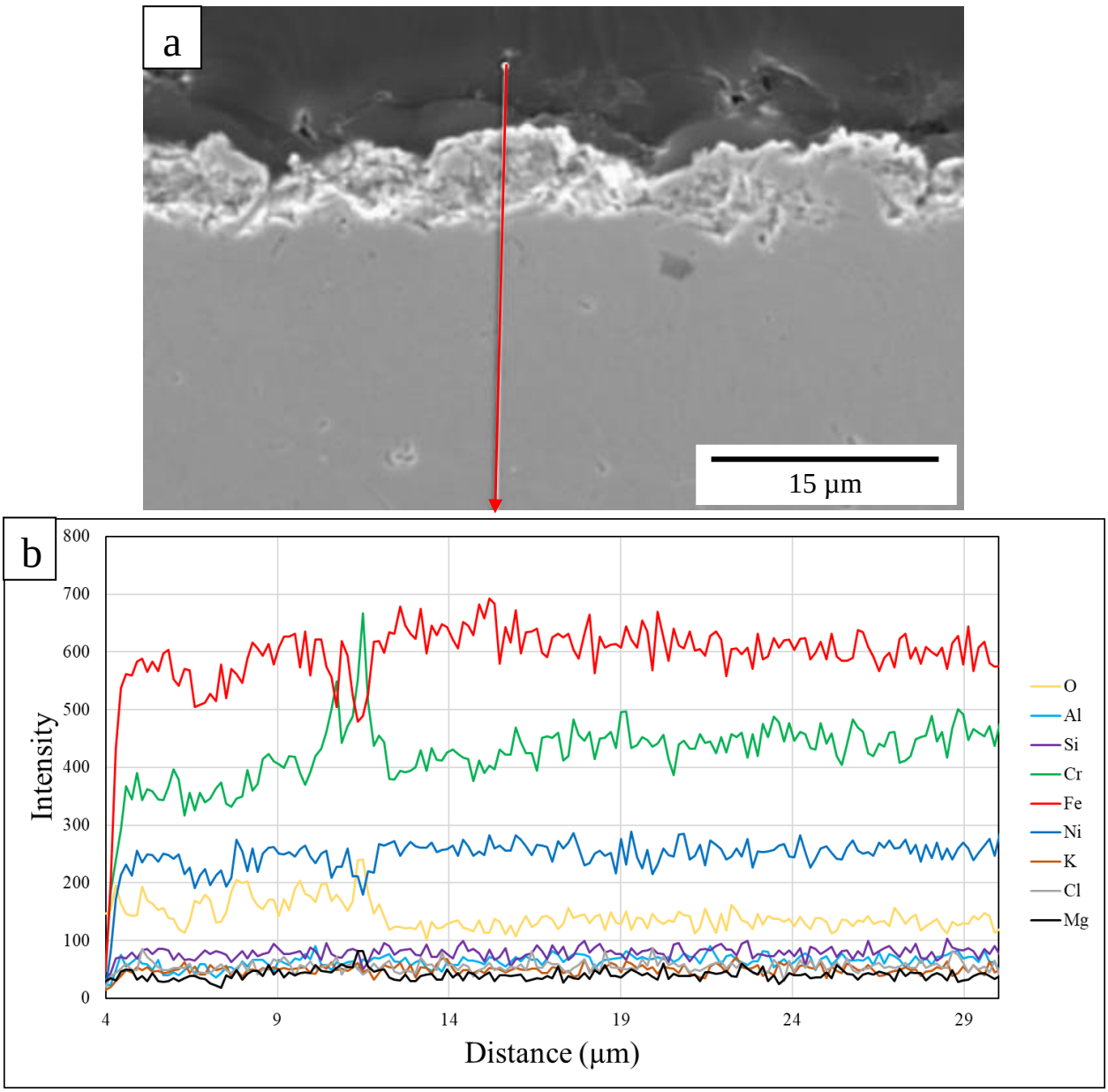

Figure 4.16: (a) BSE cross-sectional image of CP I800H after immersion in molten chloride salt mixture at 700 °C for 100 h showing location of the EDS line scan, and (b) set of elemental EDS lines scans acquired through the cross-section.

Figure 4.17 displays the EDS depth profiles through the cross-section of PO I800H. Cr is depleted 11 µm beneath the oxide scales. The oxide scale is enriched in Mg, Cr, and Si. Al, Mg, and O are enriched at the corroded grain boundaries.

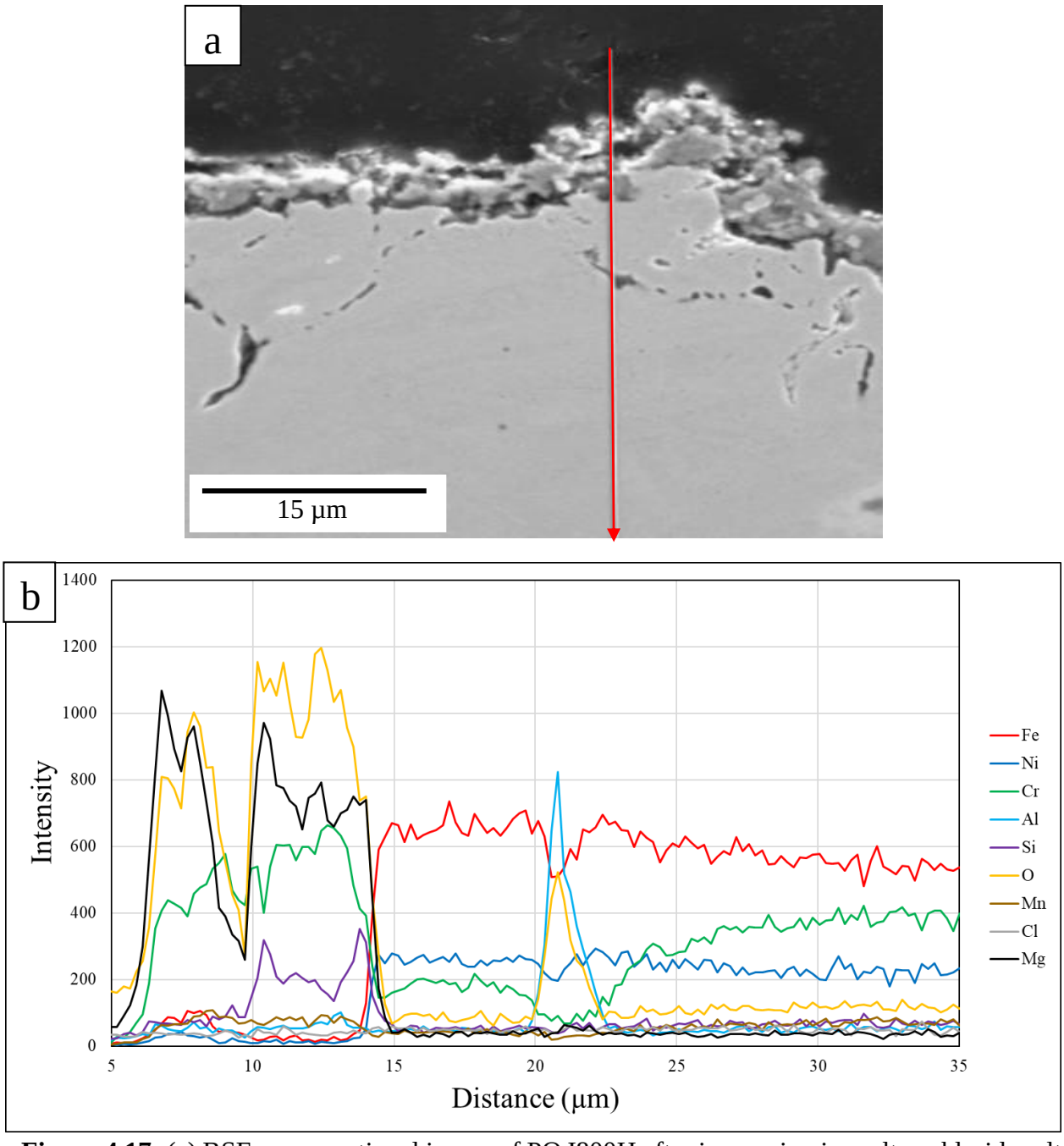

Figure 4.17: (a) BSE cross-sectional image of PO I800H after immersion in molten chloride salt mixture at 700 °C for 100 h showing location of the EDS line scan, and (b) set of elemental EDS lines scans acquired through the cross-section.

Figure 4.18 displays the EDS depth profiles through the cross-section of PO+CP I800H. Cr is depleted 9 µm beneath the oxide scales. The oxide scale is enriched in Mg, and Cr. Al, Mg, and O are enriched at the corroded grain boundaries.

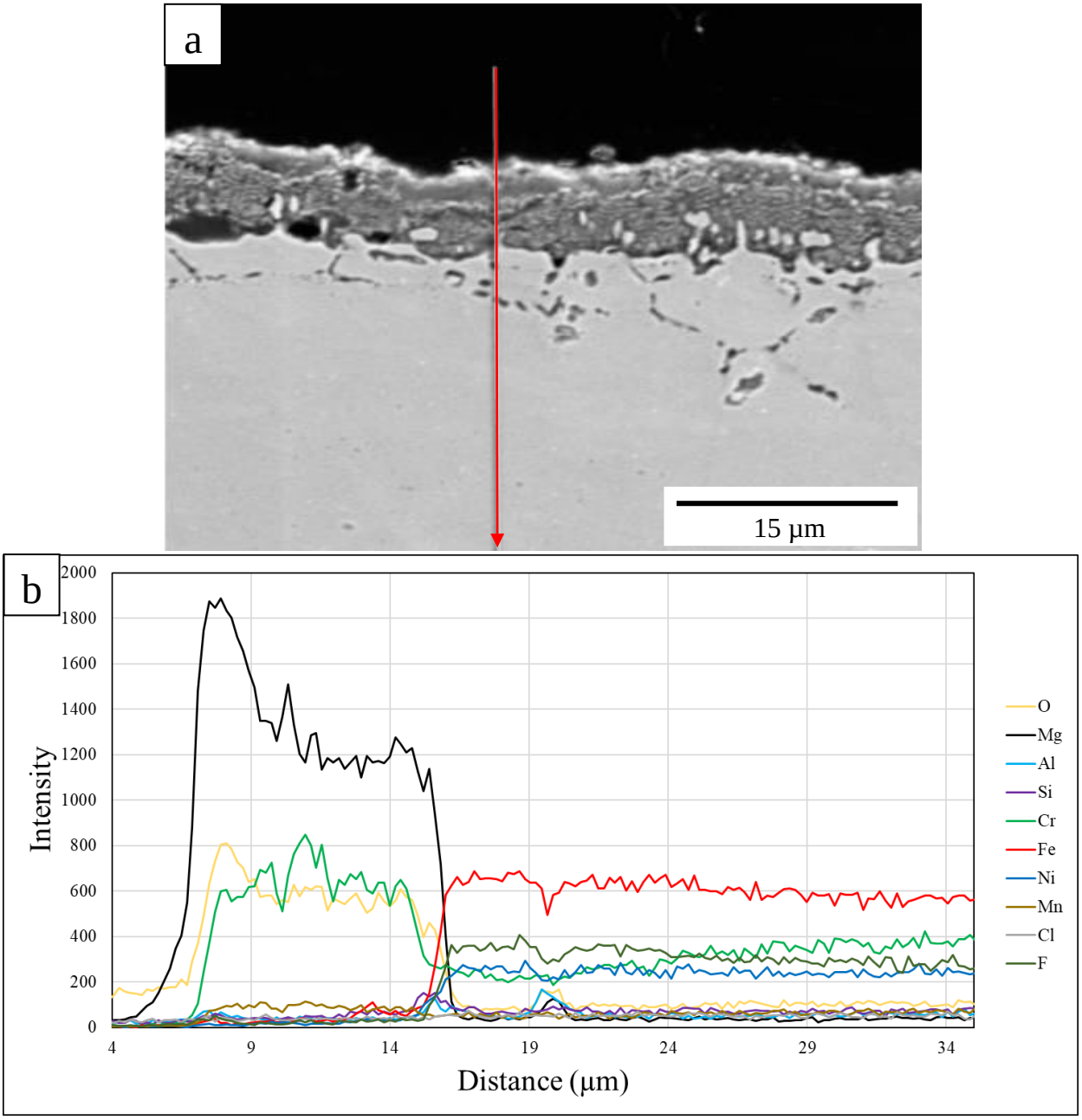

Figure 4.18: (a) BSE cross-sectional image of PO+CP I800H after immersion in molten chloride salt mixture at 700 °C for 100 h showing location of the EDS line scan, and (b) set of elemental EDS lines scans acquired through the cross-section.

4.3.2 H214

Figure 4.19 displays the plan-view SE images of unprotected and pre-oxidized H214 samples before and after exposure to molten chloride salts, with and without chemical purification. The unprotected specimen displays a clean surface and the specimen exposed with chemical purification shows darkened regions. The pre-oxidized specimen exposed without chemical purification displays a surface where the light oxide scale has been almost completely removed. The pre-oxidized specimen exposed with chemical purification has clean oxide scale.

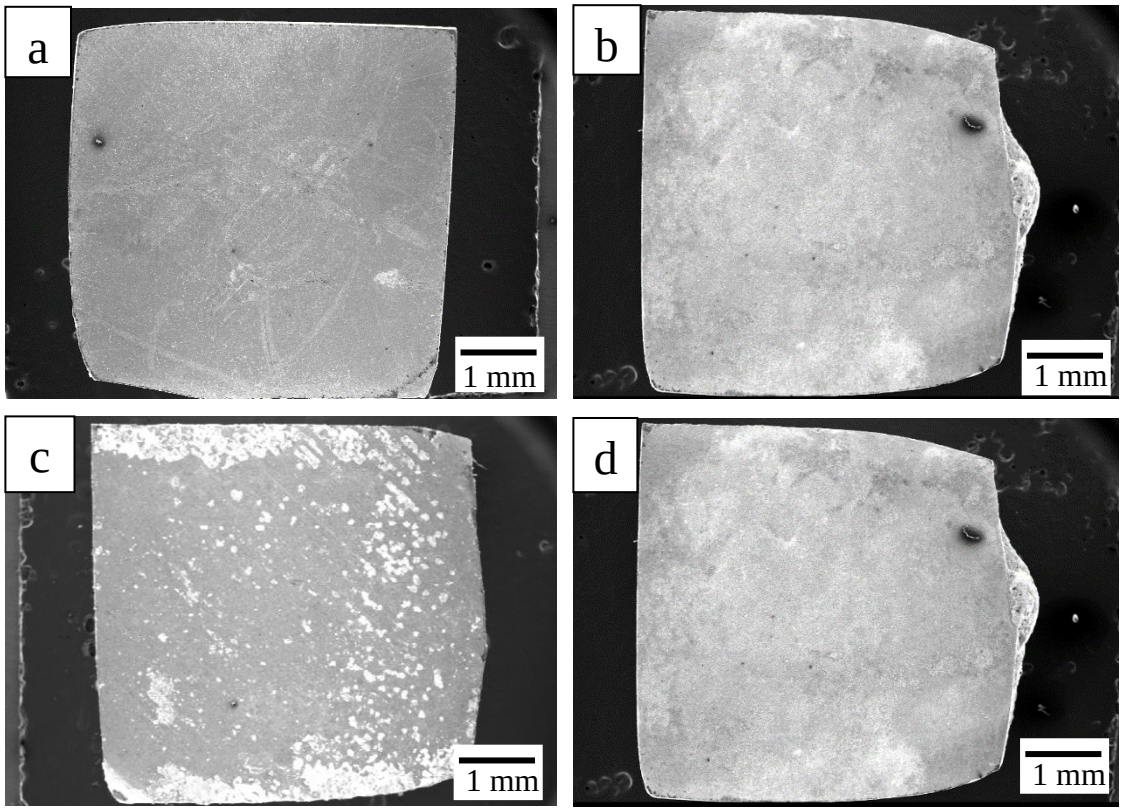

Figure 4.19: Figure 4.6: Plan view SE images showing the typical appearance of the H214 surface after immersion in molten KCl-$MgCl_2$ at 700 °C for 100 h and subsequent de-salting: (a) UP, (b) CP, (c) PO and (d) PO+CP.

Figure 4.20 displays the average mass loss of the triplicate H214 specimens that were exposed to molten chloride salt in presence and in absence of a Mg corrosion inhibitor. Standard deviation bars that are unique to each condition were calculated using 95% confidence intervals and are included for each corrosion control measure. The mass loss for unprotected H214 is 1.35 mg/cm^2. H214 has a mass gain of 0.4 mg/cm^2 when chemical purification was added to the salt mixture. This suggests that a Mg species precipitated onto the surface of the alloy during exposure. The mass loss of H214 was reduced by 100% when a Mg corrosion inhibitor was included in the salt mixture. The significant reduction of mass loss when chemical purification was included suggests that the Mg preferentially reacted with the corrosive impurities and as a result, reduced the corrosion attack on the alloy. The mass loss of pre-oxidized H214 was 0.95 mg/cm^2 without chemical purification, and pre-oxidized H214 had a mass gain of 0.1 mg/cm^2 with chemical purification. The mass loss of pre-oxidized H214 was reduced by 100 % when a Mg corrosion inhibitor was included in the salt mixture. Pre-oxidized H214 without chemical purification had a lower mass loss than unprotected H214 without chemical purification. This suggests that the pre-oxidized alloy can provide better protection to H214 than the bare metal. Pre-oxidized H214 without chemical purification still experienced considerable mass loss, most likely due to the dissolution of the mixed oxide scale.

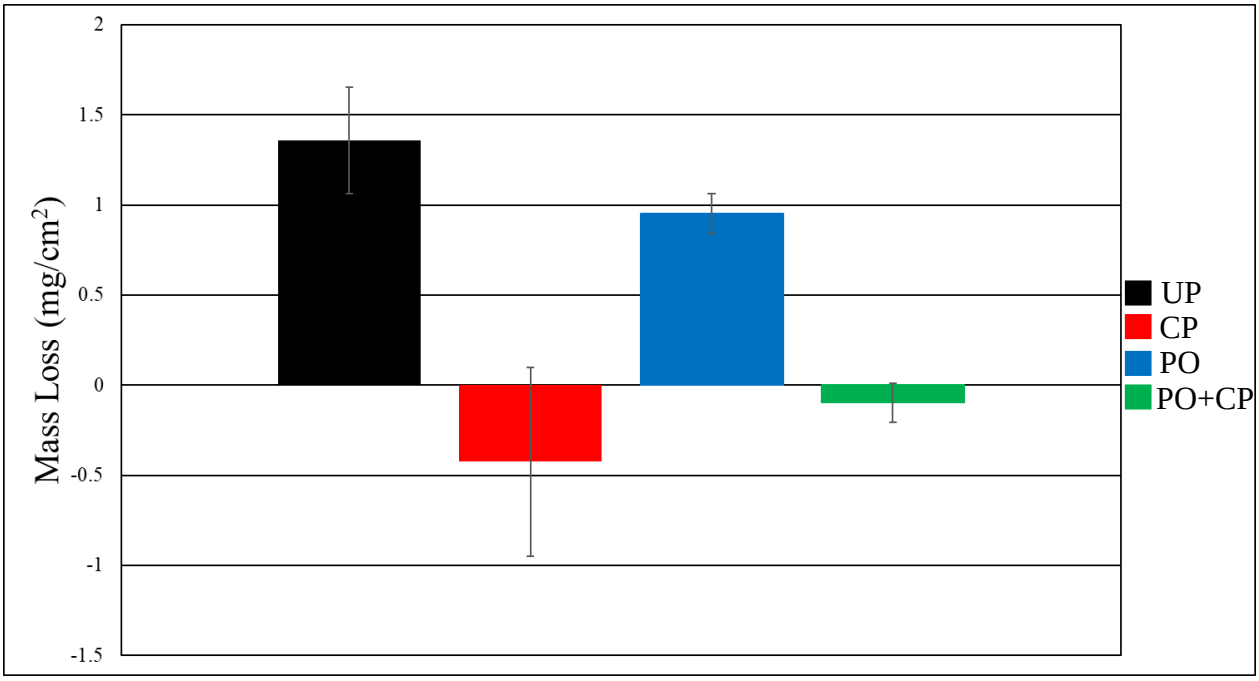

Figure 4.20: Average mass loss of H214 coupons after immersion in molten KCl-$MgCl_2$ at 700 °C for 100 h and subsequent de-salting.

Figure 4.21 presents the XRD measurements of unprotected and pre-oxidized H214 after immersion in molten chloride salt with and without chemical purification. XRD measurements indicated that the unprotected H214 sample without chemical purification consists of an austenite FCC phase. The specimen immersed with chemical purification consists of the same austenite FCC phase, as well as MgO. The XRD measurement of the pre-oxidized sample without chemical purification has an austenite FCC phase. XRD analysis of the pre-oxidized alloy with chemical purification indicates the phases present are an austenite FCC phase, a MgO phase, as well as a ferrite BCC phase. These results confirm that MgO is precipitating onto the surface of the unprotected and pre-oxidized H214 exposed with chemical purification during exposure.

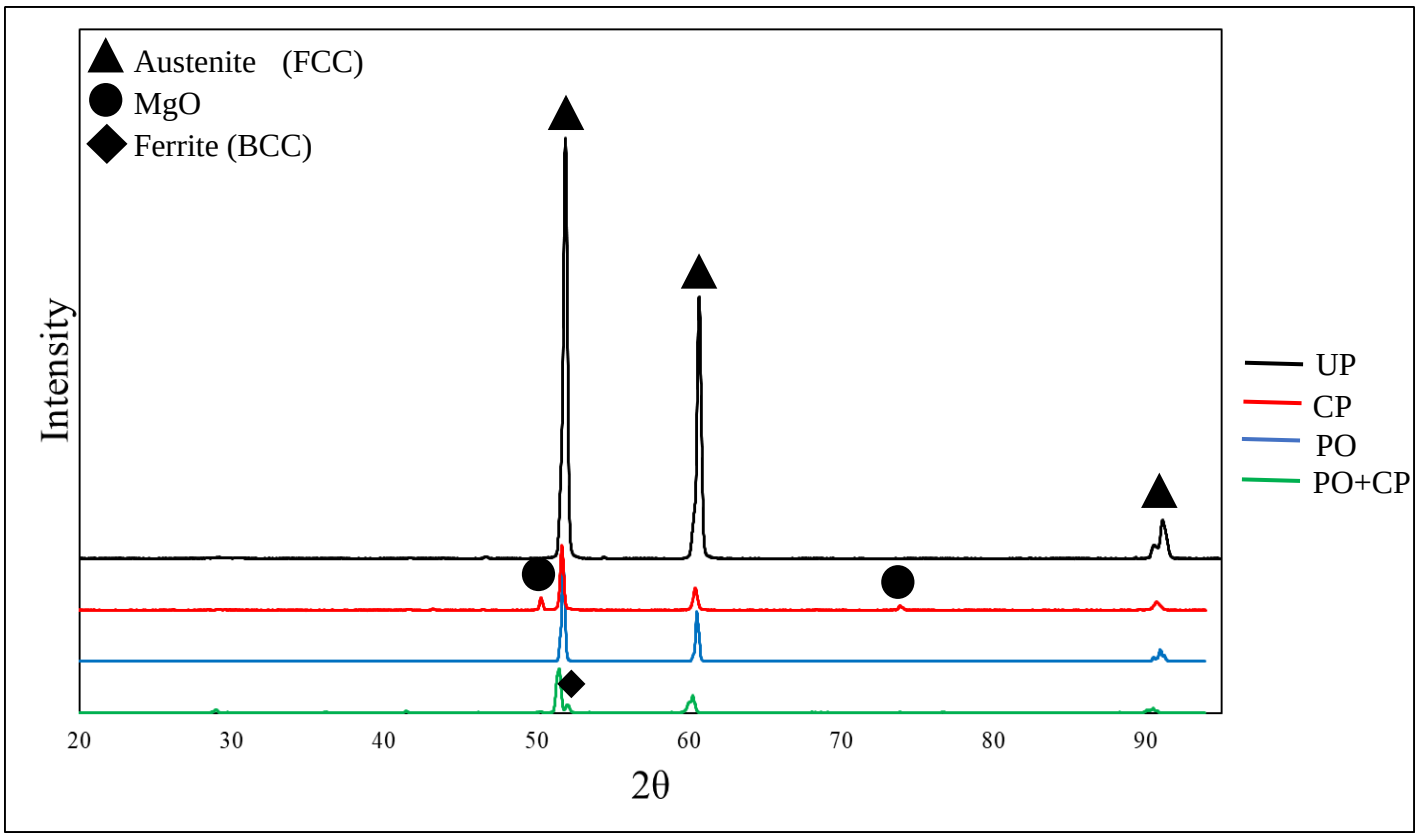

Figure 4.21: XRD spectra acquired from H214 surfaces after immersion in molten in molten KCl-$MgCl_2$ at 700 °C for 100 h and subsequent de-salting.

Figure 4.22 displays the plan-view SE images of unprotected and pre-oxidized H214 after exposure to molten chloride salt with and without chemical purification. The surface of unprotected H214 drastically changes between the sample with and without chemical purification. Corrosion occurred preferentially along the grain boundaries of unprotected H214. SE images of H214 with chemical purification reveals sponge-like structures on the surface. The SE image of pre-oxidized H214 without chemical purification reveals the grains of the alloy due to intergranular oxidation, and localized corrosion resulted in a distribution of pores along the grain boundaries. Pre-oxidized H214 exposed with chemical purification has a sponge-like structure that covers the surface of the alloy.

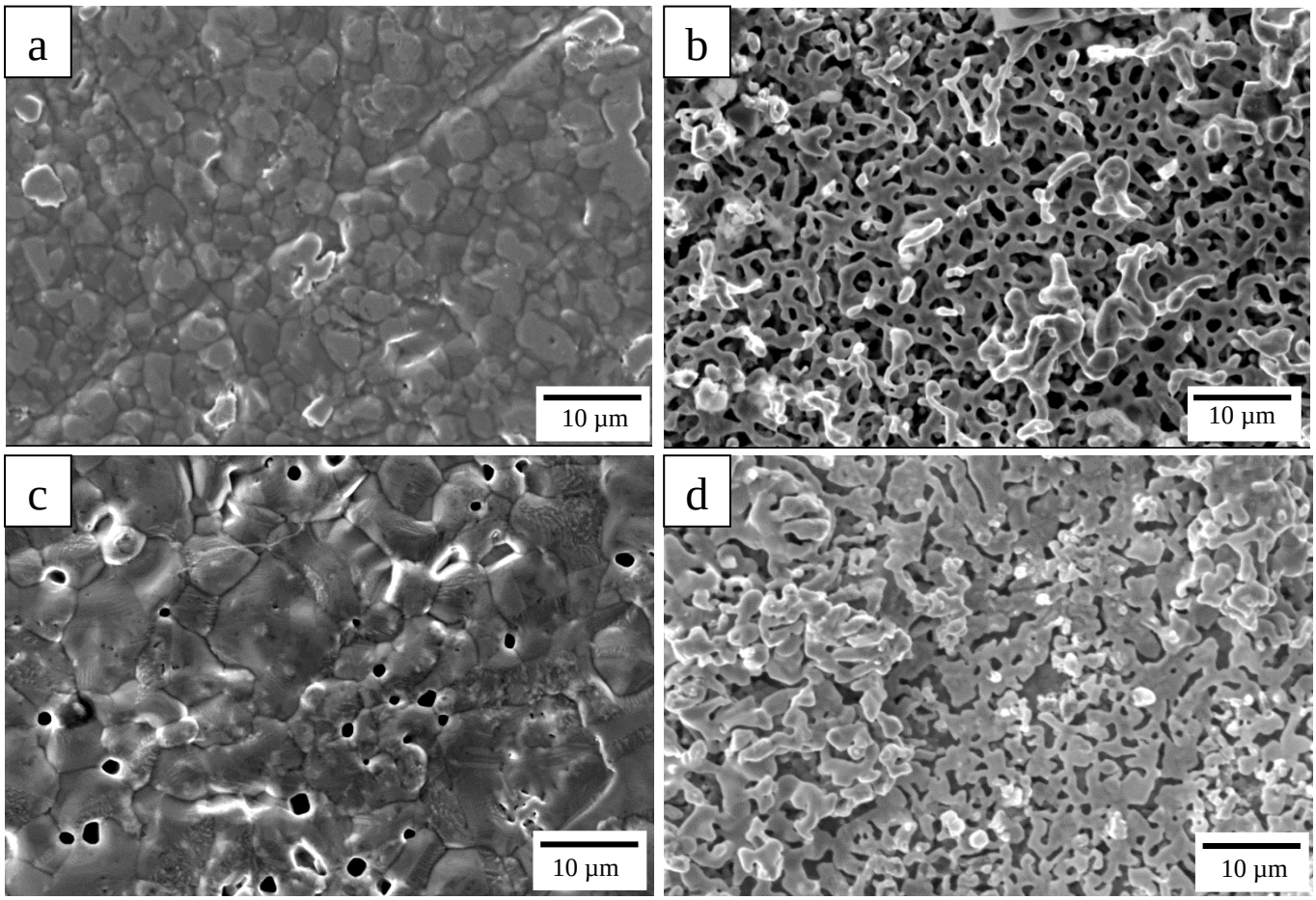

Figure 4.22: Plan-view SE images of H214 surfaces after immersion in molten KCl-$MgCl_2$ at 700 °C for 100 h and subsequently de-salting: (a) UP, (b) CP, (c) PO and (d) PO+CP.

Figure 4.23 displays the EDS elemental maps of the cross-section of unprotected H214 after exposure to molten chloride salts. A 5 µm thick corroded layer is observed with localized corrosion extending 13 µm into the substrate. The regions of localized corrosion are enriched with Mg, O, and Al. Cr is depleted 14.5 µm into the substrate. Fe and Ni only show signs of depletion in the localized corrosion regions. Trace amounts of Cl is detected in the cross-section.

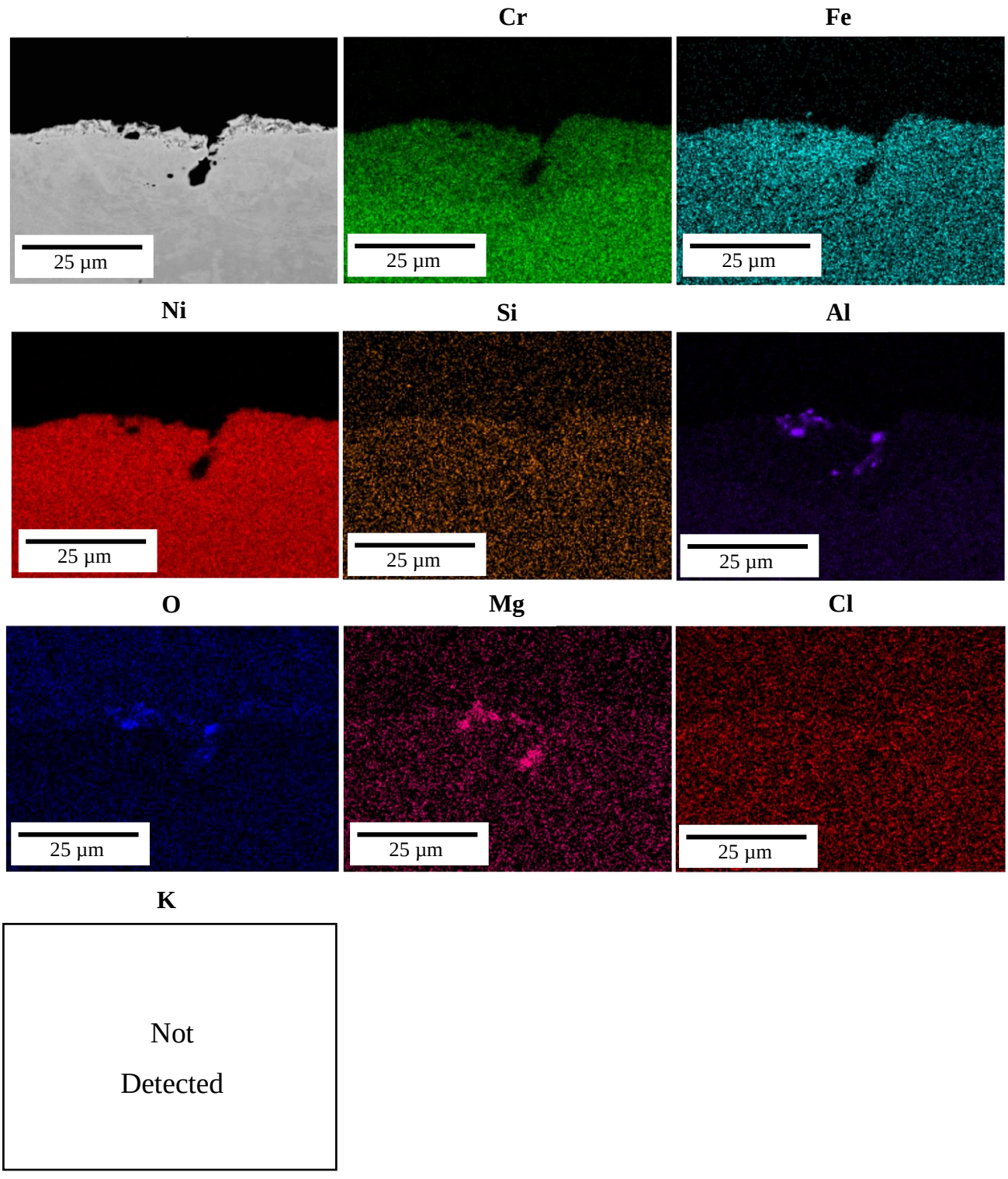

Figure 4.23: BSE cross-sectional image, and associated EDS elemental maps, of the H214 UP surface after immersion in molten KCl-$MgCl_2$ at 700 °C for 100 h and subsequent de-salting.

Figure 4.24 below presents the EDS elemental maps of the cross-section of H214 after exposure to molten chloride salt with Mg additions. A 5 μm thick discontinuous layer consisting of Al, O, and Mg is observed on the sample surface. Cr depletion extends 5 μm into the alloy substrate. Ni and Fe are unaffected by the exposure underneath the Al, O, and Mg layer. Trace amounts of Cl are detected in the cross-section.

Figure 4.25 displays the EDS elemental maps of the cross-section of pre-oxidized H214 after exposure to molten chloride salts without chemical purification. The thickness of the outer mixed oxide scale and inner alumina scale was measured to be 8 μm and 2.5-3 μm thick respectively. This indicates that the alumina scale grew about 0.5-1 μm during the corrosion exposure. Ni, Fe, and Al are present in between the inner and outer oxide layers. Mg is identified only within the mixed oxide scale and is not found within the inner alumina scale. Cr, Ni, and Fe are unaffected under the alumina scale indicating that corrosion was stopped before the substate. Trace amounts of Cl are detected in the cross-section.

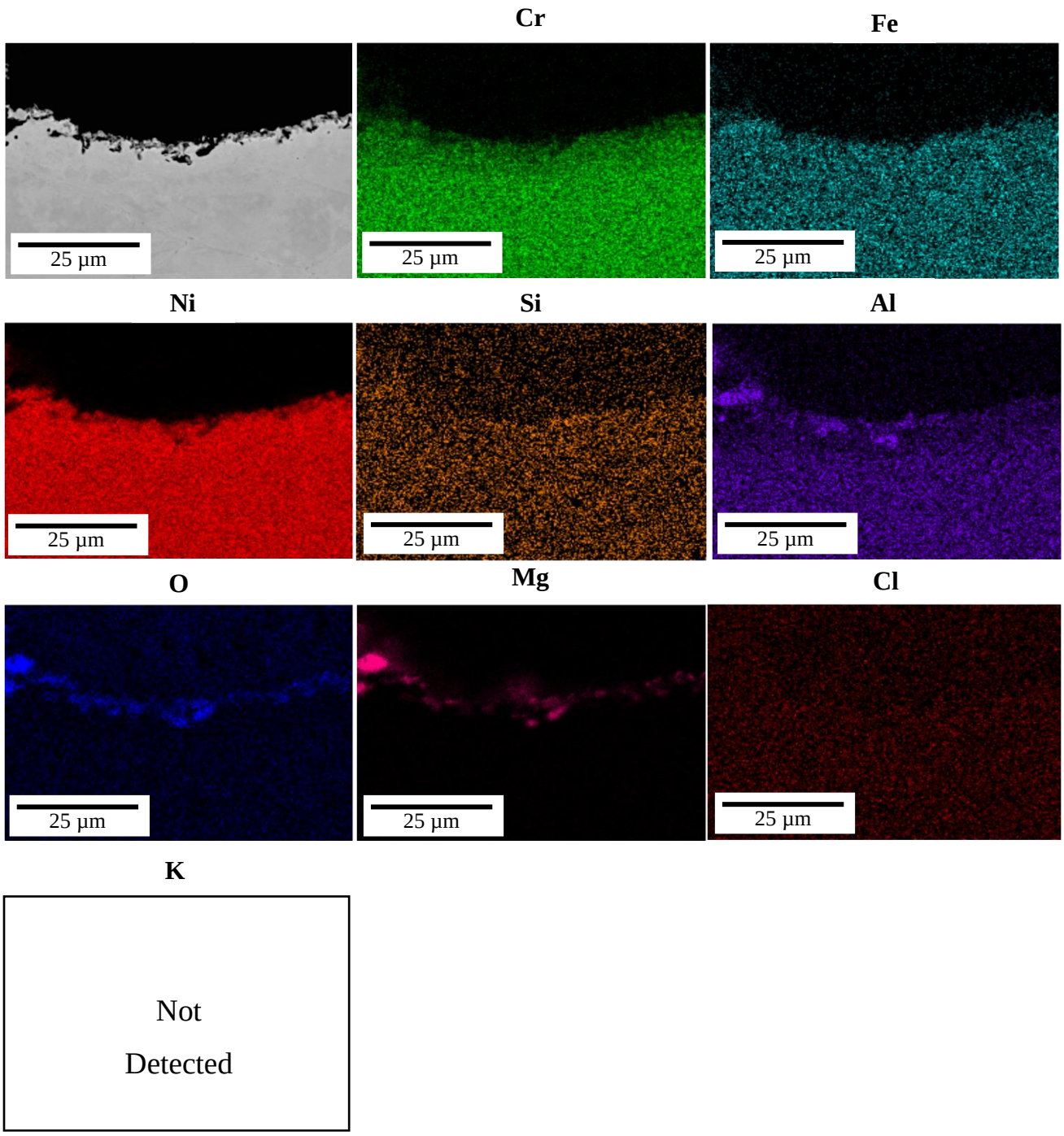

Figure 4.24: BSE cross-sectional image, and associated EDS elemental maps, of the H214 CP surface after immersion in molten KCl-$MgCl_2$ at 700 °C for 100 h and subsequent de-salting.

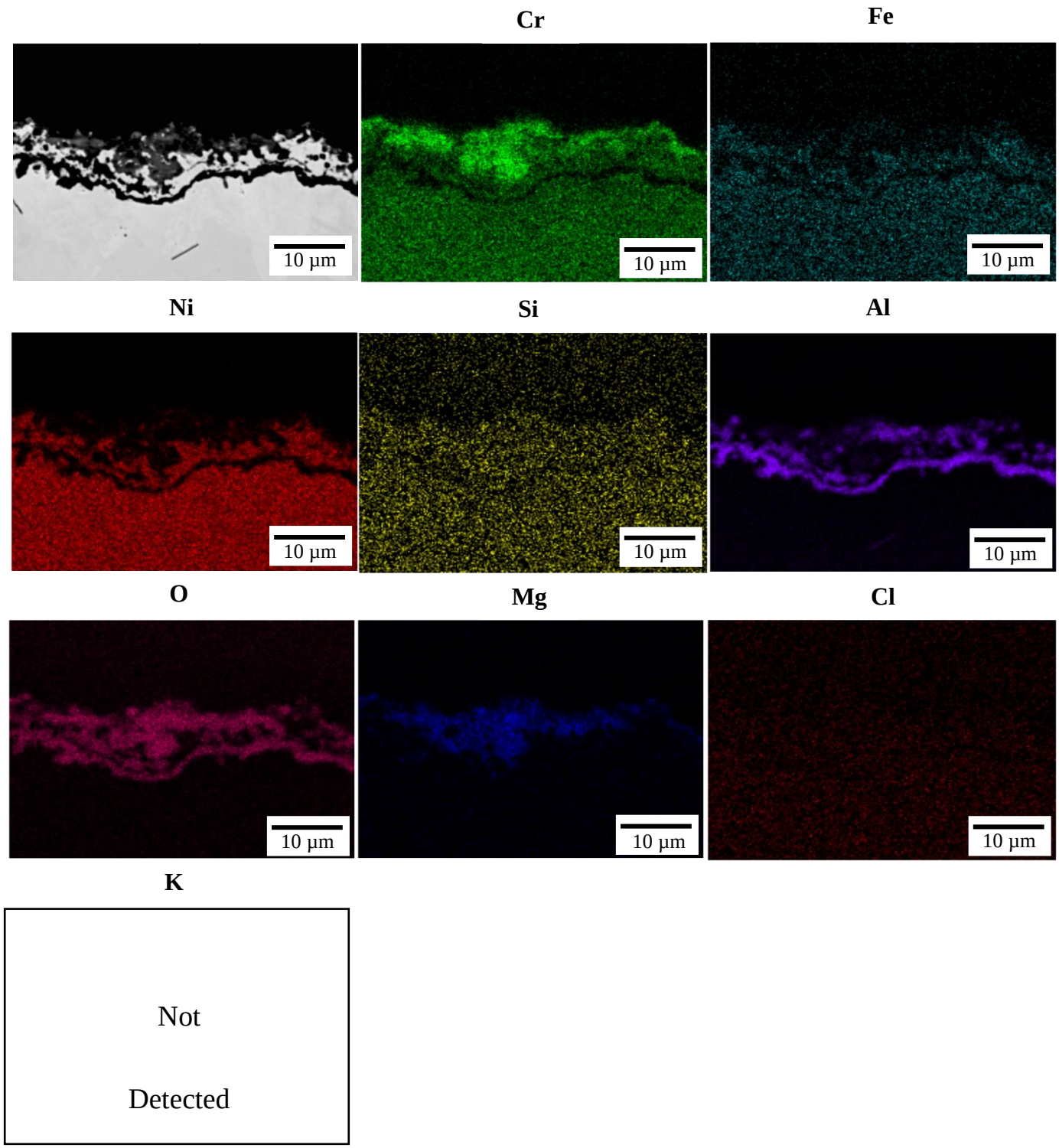

Figure 4.25: BSE cross-sectional image, and associated EDS elemental maps, of the H214 PO surface after immersion in molten KCl-$MgCl_2$ at 700 °C for 100 h and subsequent de-salting.

Figure 4.26 presents the EDS elemental maps of the cross-section of pre-oxidized H214 after exposure to molten chloride salts with chemical purification. The thickness of the outer mixed oxide and inner alumina scale was measured to be 7.5 μm and 1.6 μm thick respectively. Mg is detected within the outer mixed oxide scale but does not extend past the alumina scale into the substrate. Cr, Fe, and Ni are found within the oxide scales and are unaffected beneath the alumina scale. Trace amounts of Cl are detected in the cross-section.

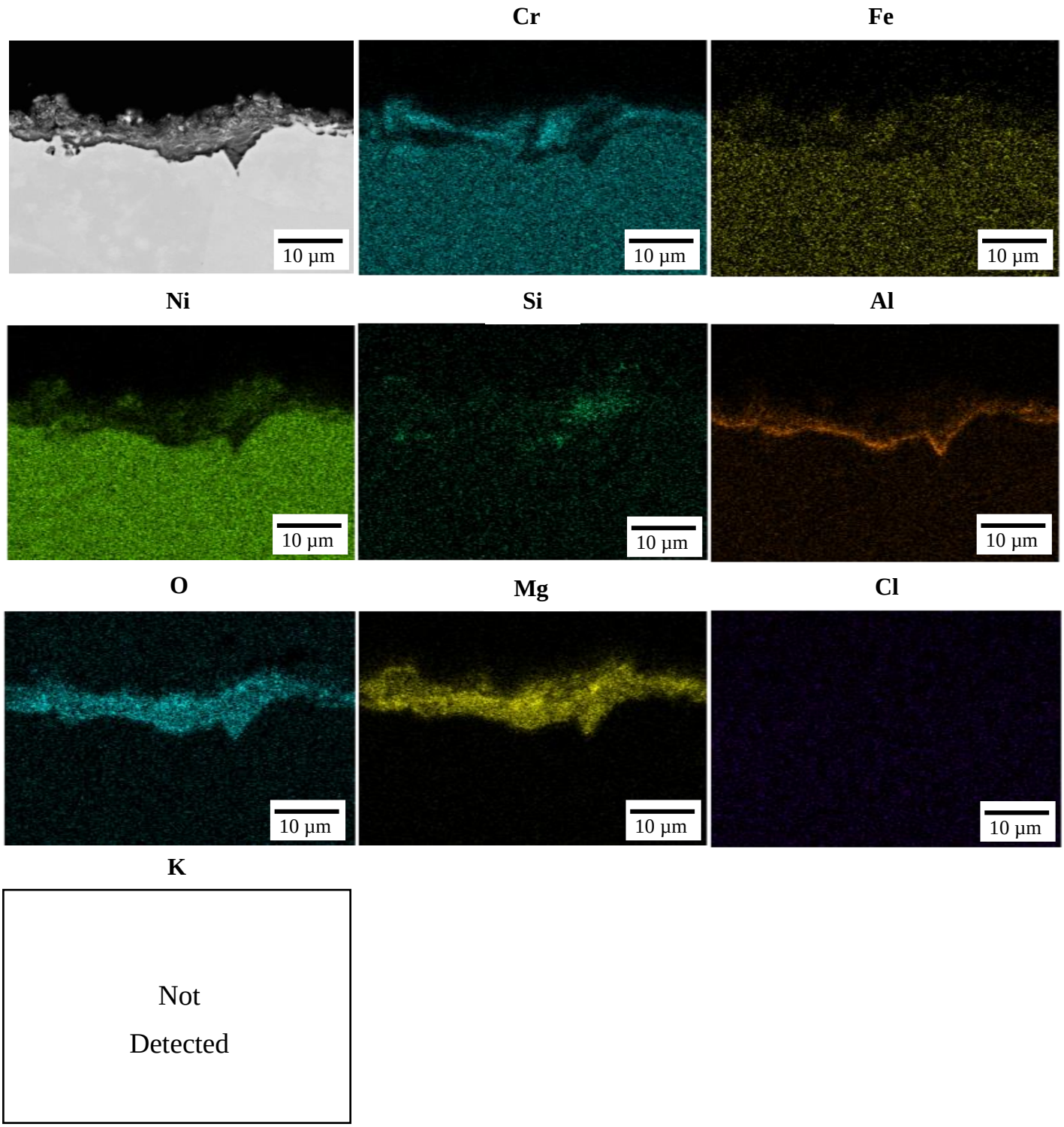

Figure 4.26: BSE cross-sectional image, and associated EDS elemental maps, of the H214 PO+CP surface after immersion in molten KCl-$MgCl_2$ at 700 °C for 100 h and subsequent de-salting.

Figure 4.27 displays the EDS depth profiles through the cross-section of UP H214. Cr is depleted 15 µm from the surface. Al and O are enriched at the site of internal oxidation.

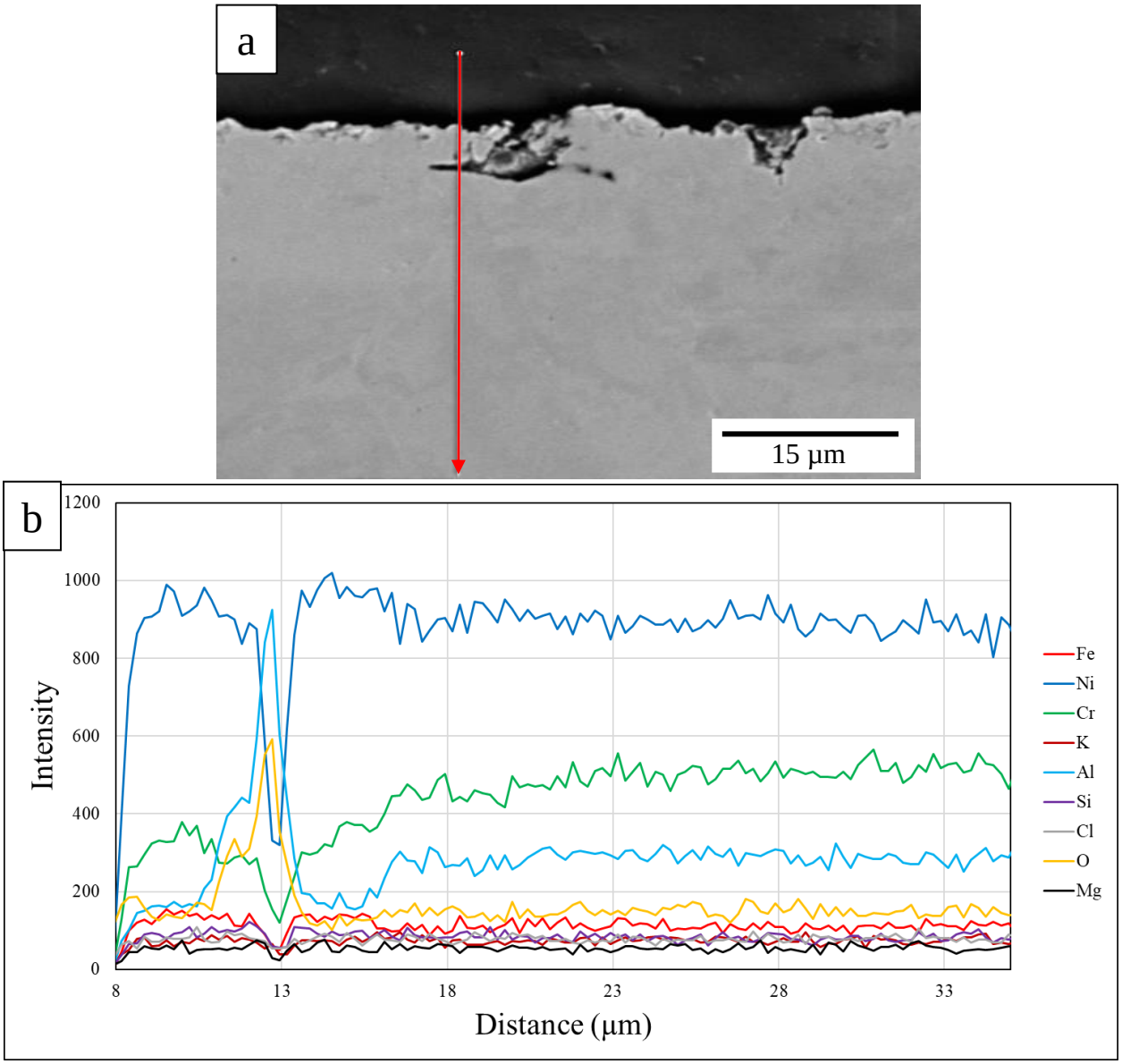

Figure 4.27: (a) BSE cross-sectional image of UP H214 after immersion in molten chloride salt mixture at 700 °C for 100 h showing location of the EDS line scan, and (b) set of elemental EDS lines scans acquired through the cross-section.

Figure 4.28 displays the EDS depth profiles through the cross-section of CP H214. Cr is depleted 10 µm from beneath the oxide scales. Mg, Ni, Al, Cr, and O are detected as scale forming elements. The intensity of Mg significantly decreases as the intensity of Al increases in the oxide scale.

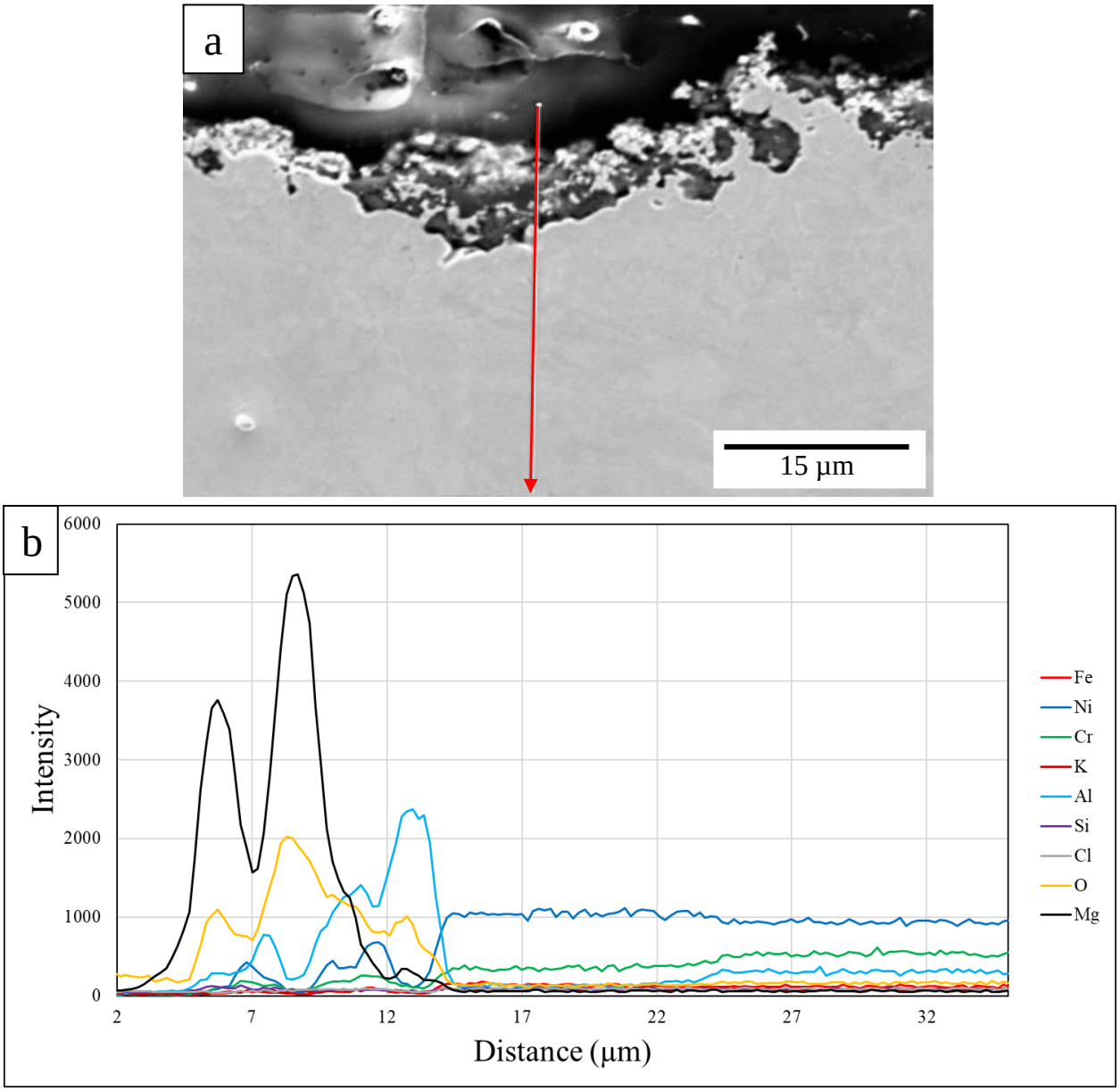

Figure 4.28: (a) BSE cross-sectional image of CP H214 after immersion in molten chloride salt mixture at 700 °C for 100 h showing location of the EDS line scan, and (b) set of elemental EDS lines scans acquired through the cross-section.

Figure 4.29 displays the EDS depth profiles through the cross-section of PO H214. Cr is depleted 2 µm from beneath the oxide scales. Mg, Ni, Al, Cr, and O are detected as scale forming elements. Mg is not identified past the inner alumina scale.

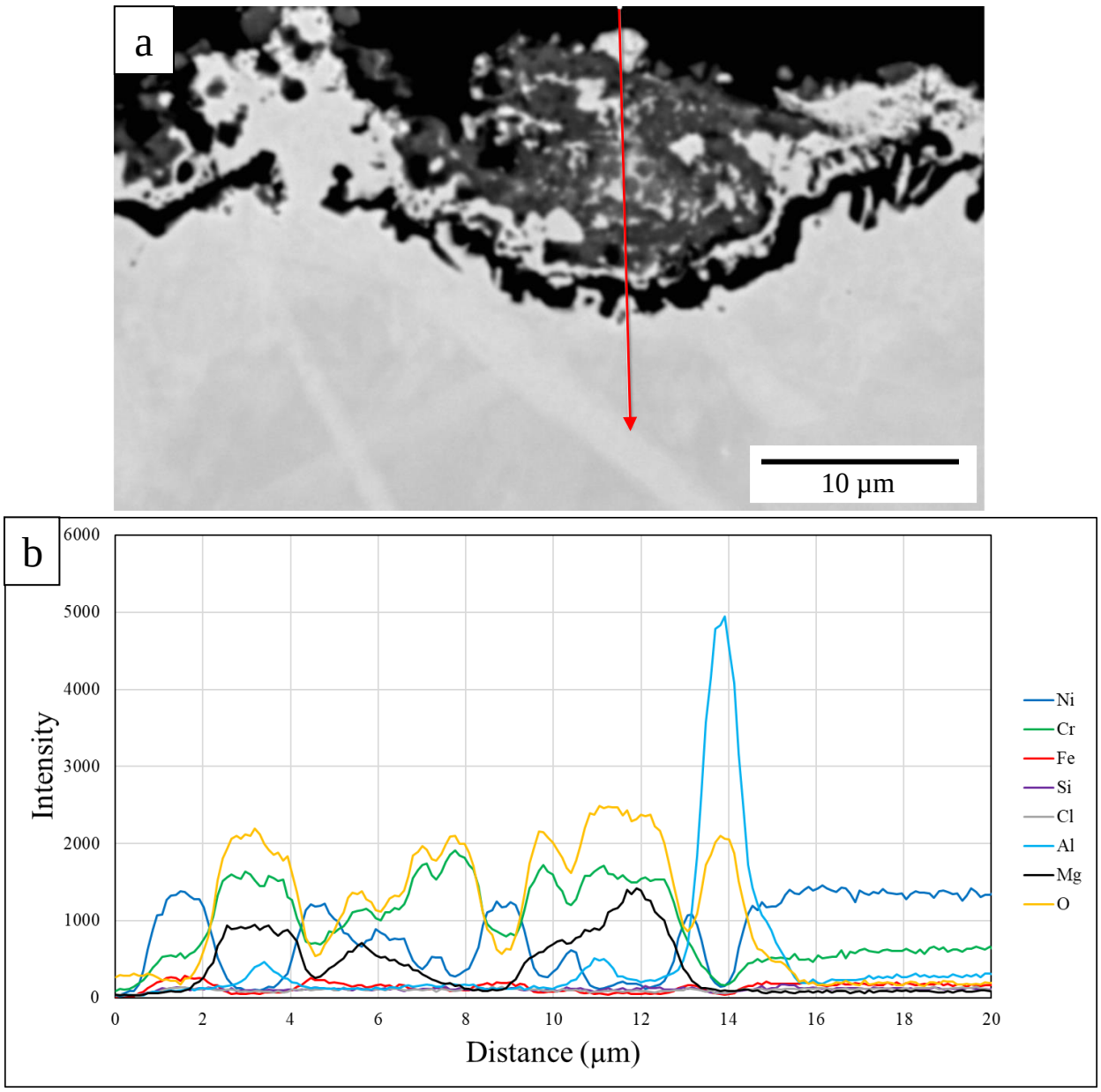

Figure 4.29: (a) BSE cross-sectional image of PO H214 after immersion in molten chloride salt mixture at 700 °C for 100 h showing location of the EDS line scan, and (b) set of elemental EDS lines scans acquired through the cross-section.

Figure 4.30 displays the EDS depth profiles through the cross-section of PO+CP H214. Cr is depleted 0 µm from beneath the oxide scales. Mg, Ni, Al, Cr, and O are detected as scale forming elements. Mg is not identified past the inner alumina scale.

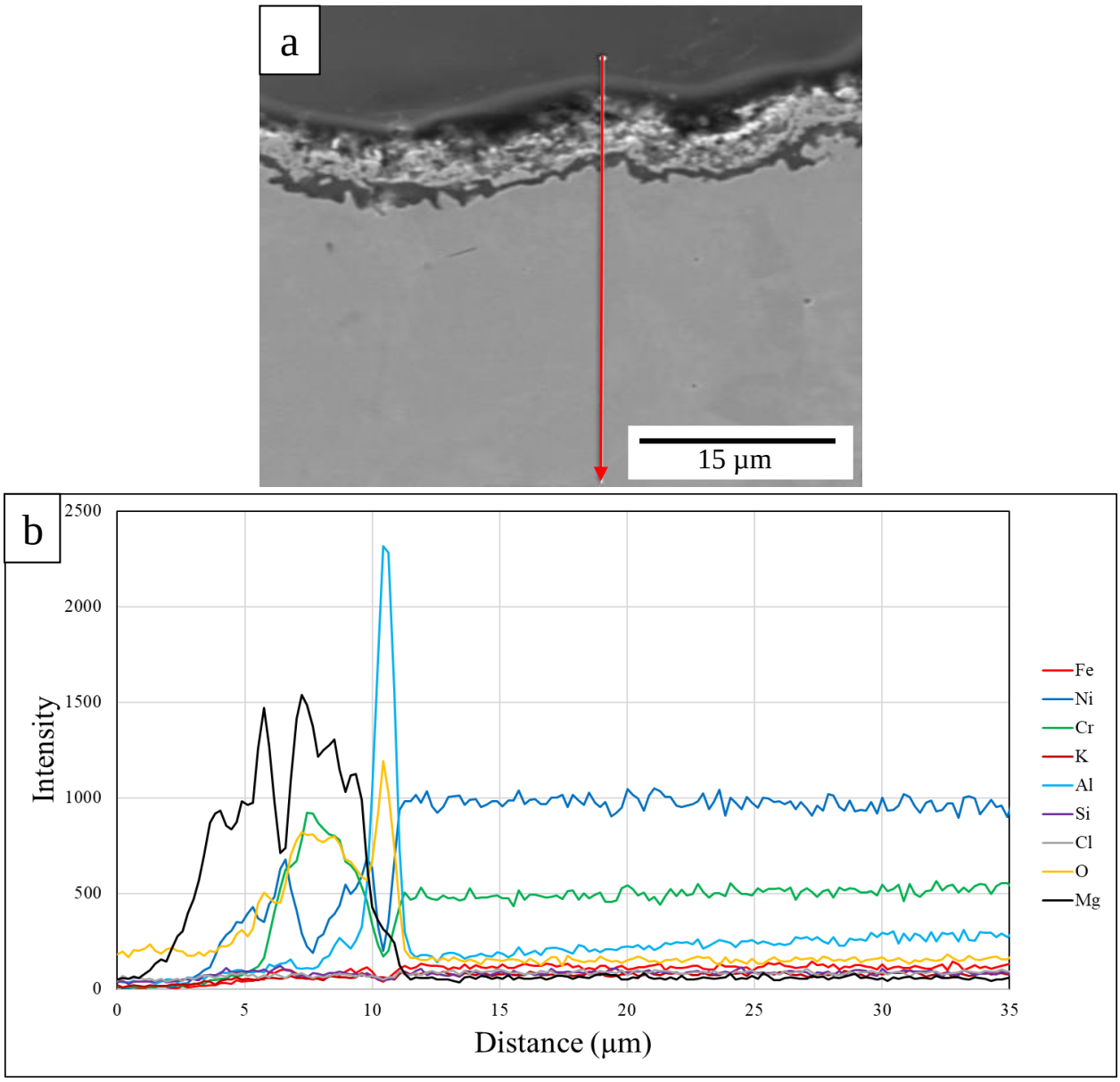

Figure 4.30: (a) BSE cross-sectional image of PO+CP H214 after immersion in molten chloride salt mixture at 700 °C for 100 h showing location of the EDS line scan, and (b) set of elemental EDS lines scans acquired through the cross-section.

4.3.3 SX

Figure 4.31 displays the plan-view SE images unprotected and pre-oxidized SX before and after exposure to molten chloride salts, with and without chemical purification. The unprotected specimen has two distinct light and dark regions. The specimen exposed with chemical purification has massive polyhedral shaped crystals on the surface (0.2-0.5 mm in length). EDS elemental maps revealed these large structures are composed of Ni and Si. The pre-oxidized specimens exposed with and without chemical purification both have lighter and darker regions distributed on the surface of the specimens.

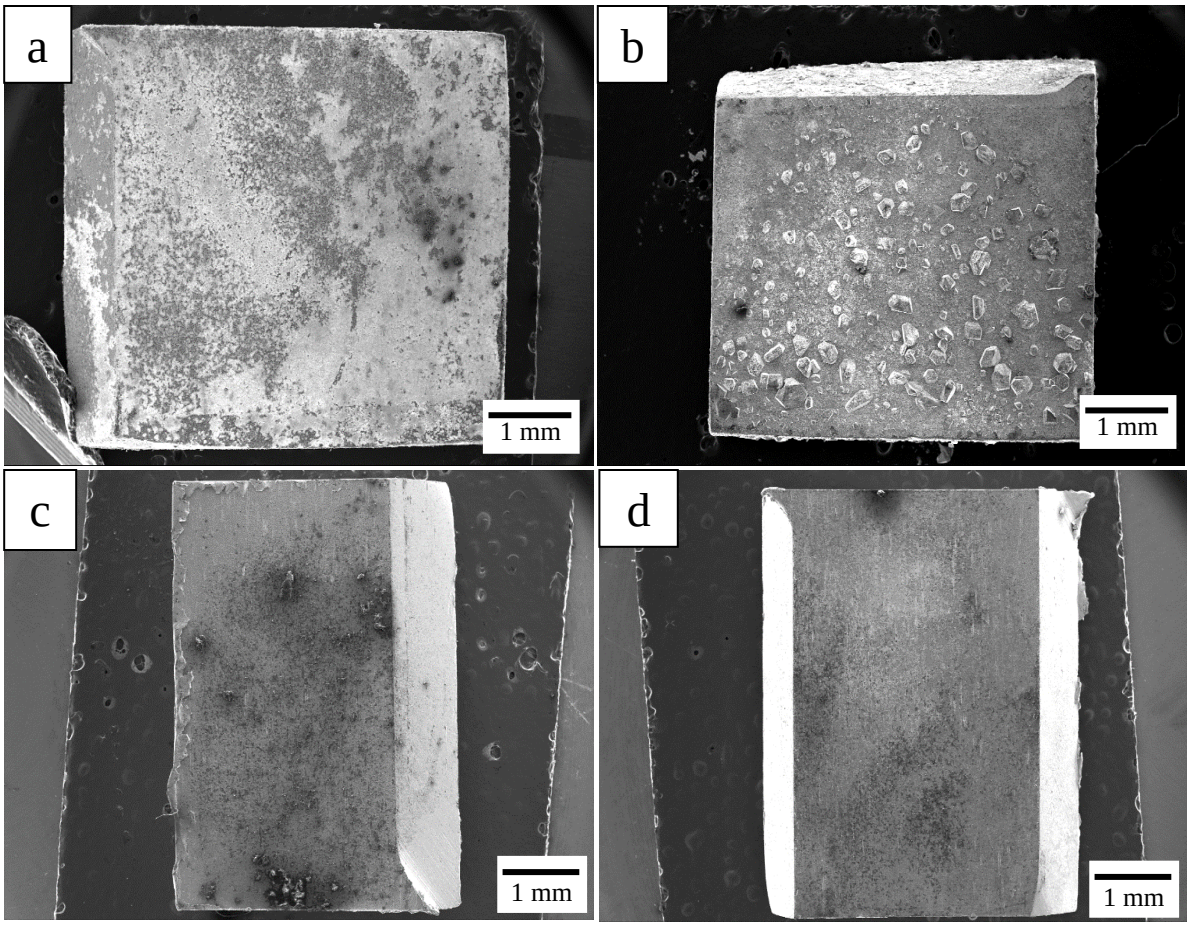

Figure 4.31: Plan view SE images showing the typical appearance of the SX surface after immersion in molten KCl-$MgCl_2$ at 700 °C for 100 h and subsequent de-salting: (a) UP, (b) CP, (c) PO and (d) PO+CP.

Figure 4.32 displays the average mass loss of the triplicate SX specimens that were exposed to molten chloride salt in presence and in absence of a Mg corrosion inhibitor. Standard deviation bars that are unique to each condition were calculated using 95% confidence intervals and are included for each corrosion control measure. The mass loss for unprotected SX without and with chemical purification is 3.4 mg/cm^2 and 0.25 mg/cm^2 respectively. The mass loss of SX was reduced by 92.6 % when a Mg corrosion inhibitor was included in the salt mixture. The significant reduction of mass loss when chemical purification was included suggests that Mg preferentially reacted with the corrosive impurities and as a result, reduced the corrosion of the alloy. The mass loss of pre-oxidized SX without and with chemical purification was 0.5 mg/cm^2 and 0.2 mg/cm^2 respectively. The mass loss of pre-oxidized SX was reduced by 60 % when a Mg corrosion inhibitor was included in the salt mixture. Pre-oxidized SX without chemical purification had a significantly lower mass loss than unprotected SX without chemical purification. This suggests that pre-oxidized alloy can provide better protection to SX than the bare metal.

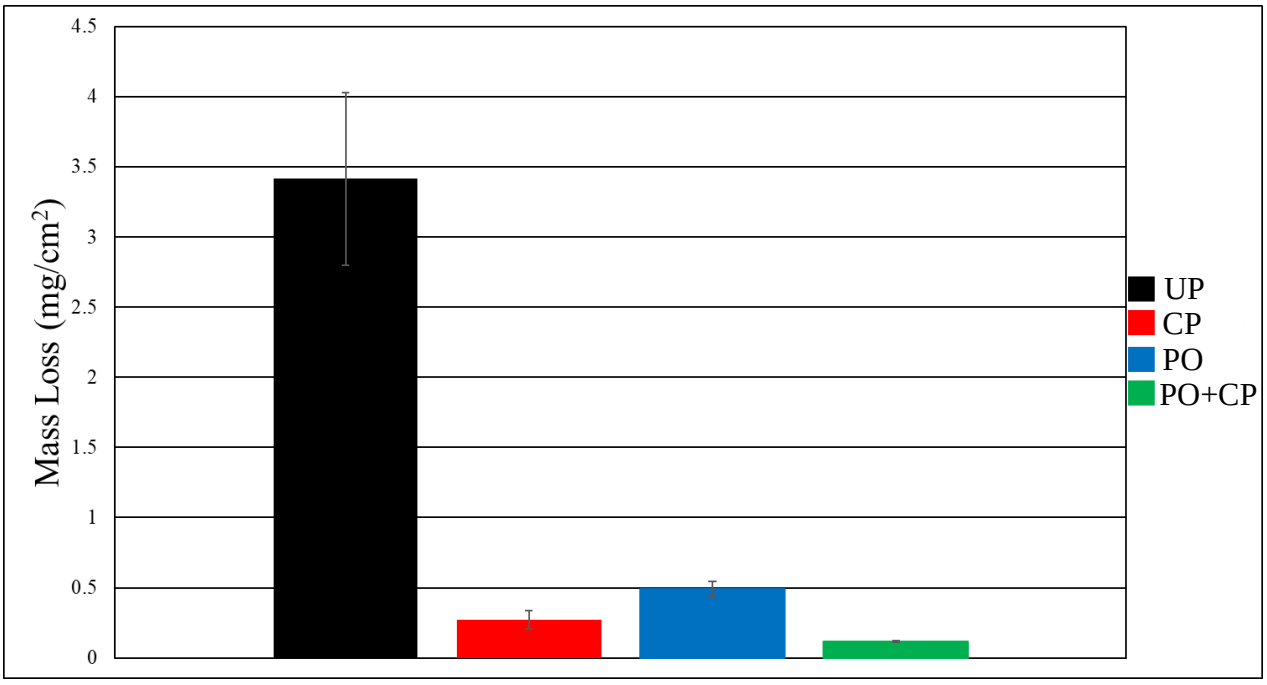

Figure 4.32: Average mass loss of SX coupons after immersion in molten KCl-$MgCl_2$ at 700 °C for 100 h and subsequent de-salting.

Figure 4.33 presents the XRD spectra of unprotected and pre-oxidized SX after exposure to molten chloride salt, with and without chemical purification. Unprotected SX has an austenite (FCC) phase, as well as a Mg_2SiO_4 phase. XRD analysis of the surface of SX immersed with chemical purification shows the three main phases present are an austenite phase, a MgO phase, and a $Mg(SiO_3)$ phase. The pre-oxidized sample without chemical purification is composed of an austenite phase. Pre-oxidized SX with chemical purification is composed of an austenite phase, a MgO phase, a Cr, Ni, and Si phase, and a Mg, Ni, and Si phase.

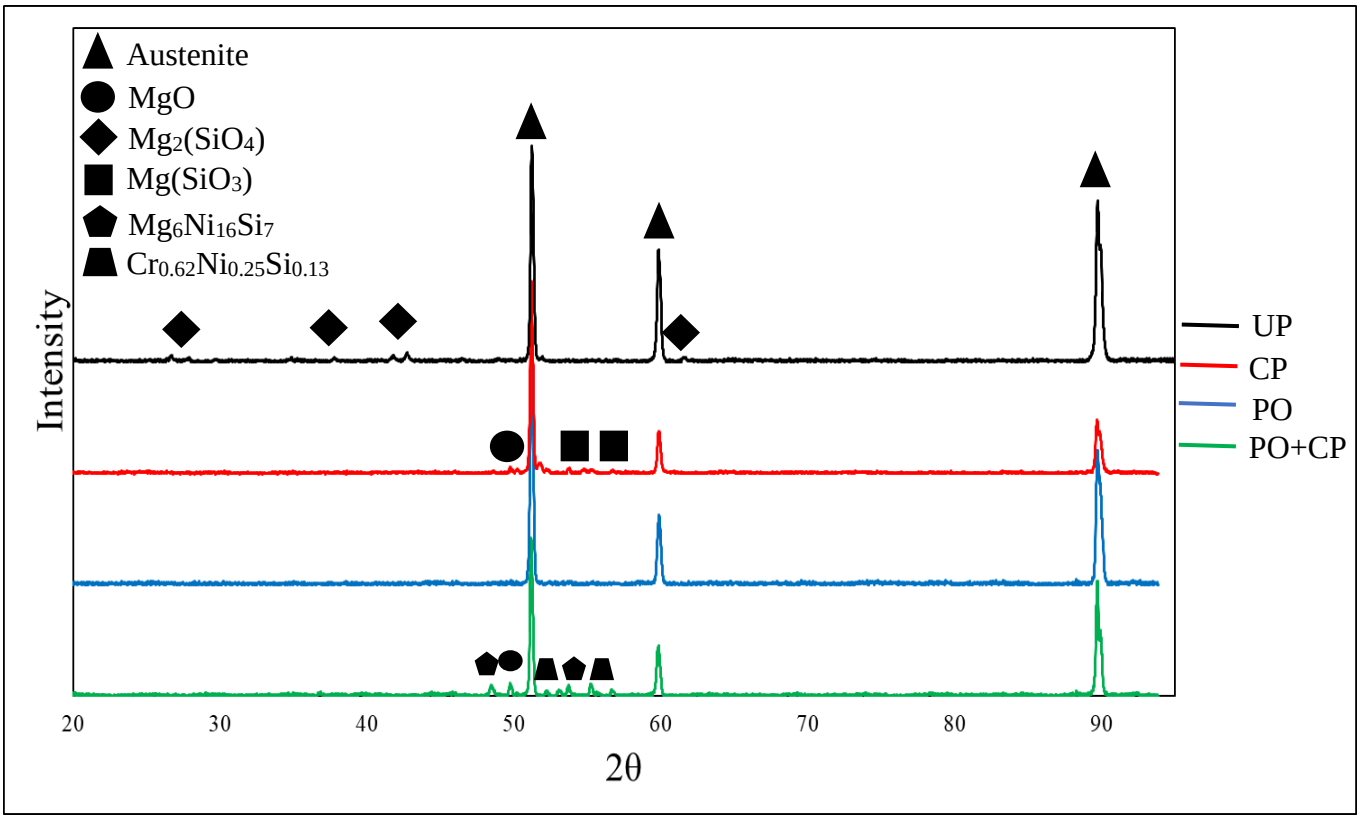

Figure 4.33: XRD spectra acquired from SX surfaces after immersion in molten in molten KCl-$MgCl_2$ at 700 °C for 100 h and subsequent de-salting

Figure 4.34 displays the SE images of unprotected and pre-oxidized SX after immersion in molten chloride salt with and without chemical purification. The surface of unprotected SX reveals two distinct phases: one is composed of small polyhedral-shaped crystals, and the other consists of large sponge-like structures. The surface of SX immersed with chemical purification reveals large sponge-like structures covered in small polyhedral-shaped crystals. Pre-oxidized SX without chemical purification has a clean surface with intergranular oxidation and small spherical structures present on the grain boundaries. Pre-oxidized SX with chemical purification displays a clean oxide scale with small spherical particles distributed on the surface.

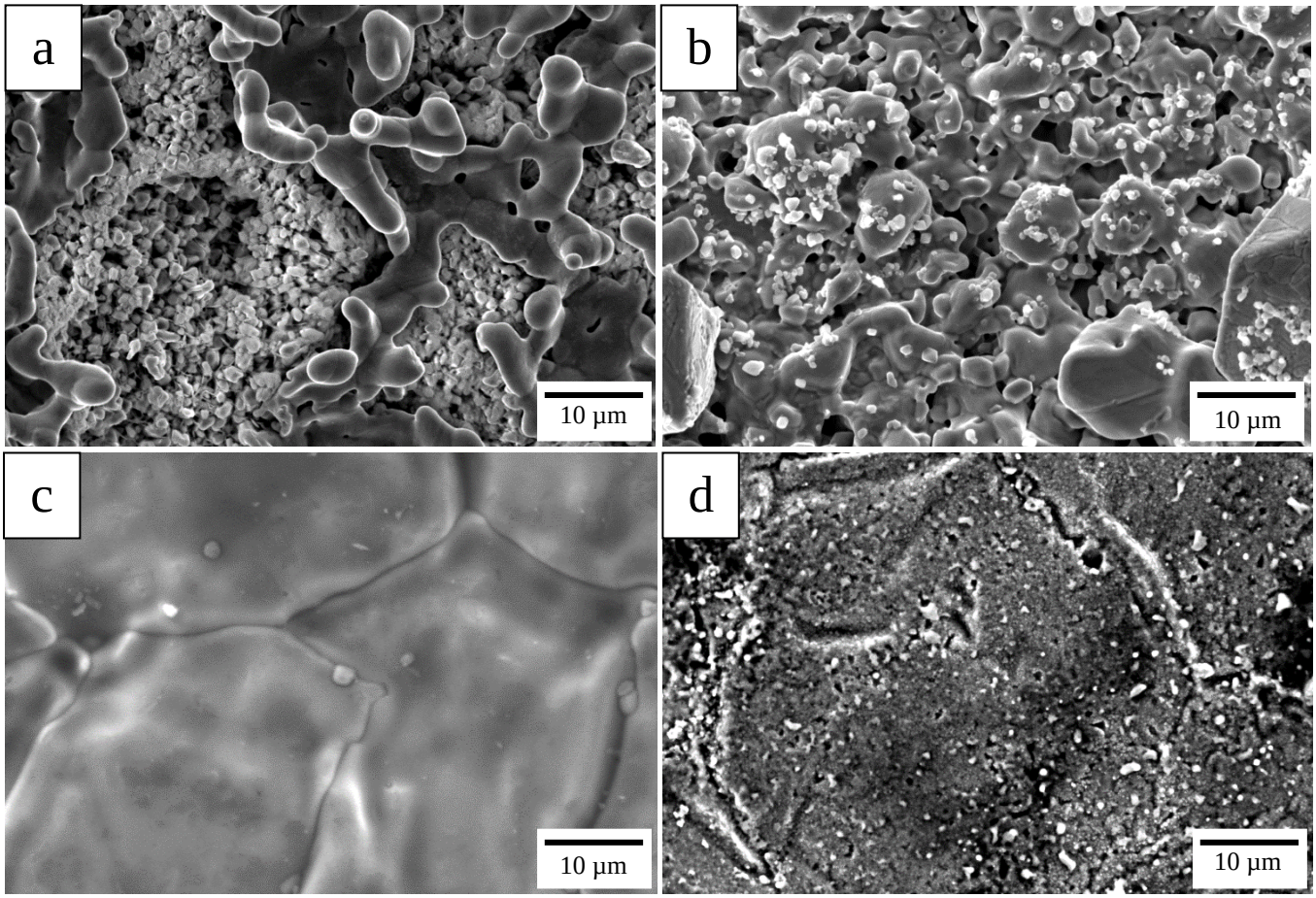

Figure 4.34: Plan-view SE images of SX surfaces after immersion in molten KCl-$MgCl_2$ at 700 °C for 100 h and subsequently de-salting: (a) UP, (b) CP, (c) PO and (d) PO+CP.

Figure 4.35 presents the cross section of unprotected SX after exposure to molten chloride salt. The BSE image displays a uniformly corroded layer that is between 5 – 8 µm thick. The EDS elemental maps reveal that Cr and Si are each depleted 8 µm from the surface of the alloy. Fe and Ni are unaffected by the exposure, and O is observed near the surface of the alloy. Cl is detected in trace amounts in the cross-section. Mg and K are not detected in the cross-section.

Figure 4.36 displays the cross section of SX after exposure to molten chloride salt with chemical purification. The EDS elemental maps reveal that the Cr and Si depletion are reduced to less than 1 µm into the substrate when chemical purification is added to the salt mixture. A 2-3 µm thick layer of O is located on the surface of the alloy. Fe and Ni are unaffected by the exposure when a Mg corrosion inhibitor is added to the salt mixture.

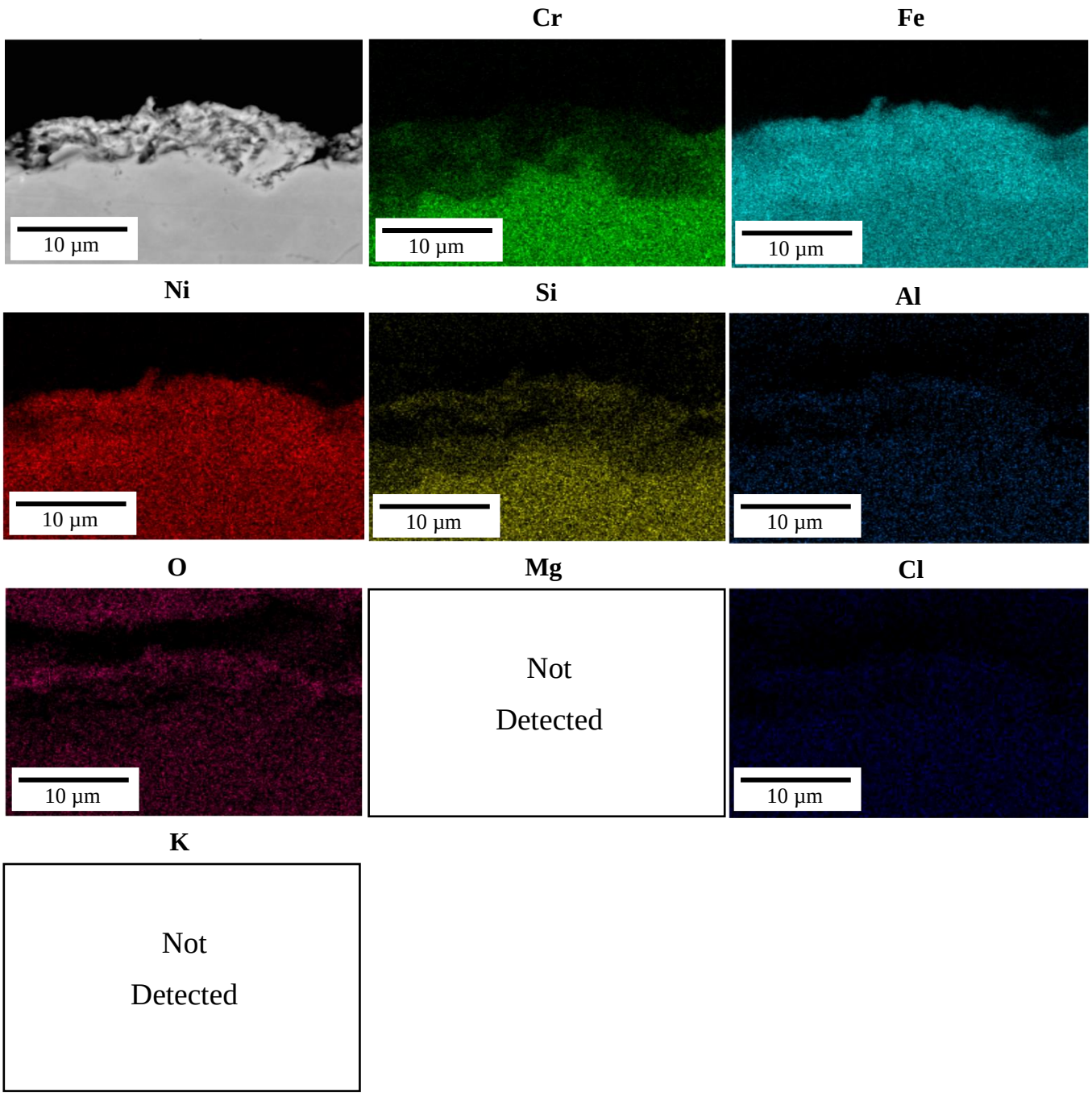

Figure 4.35: BSE cross-sectional image, and associated EDS elemental maps, of the SX UP surface after immersion in molten KCl-$MgCl_2$ at 700 °C for 100 h and subsequent de-salting.

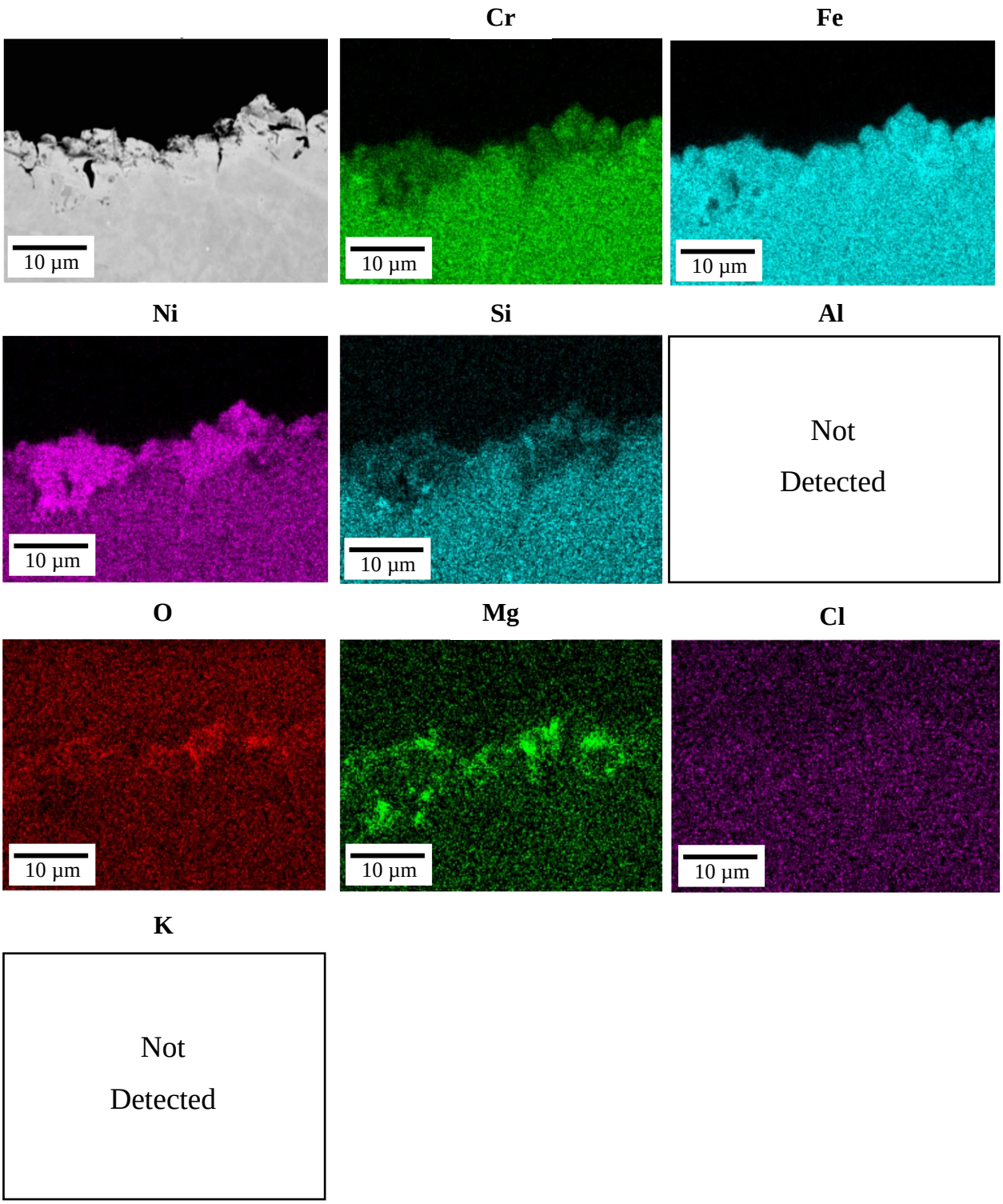

Figure 4.36: BSE cross-sectional image, and associated EDS elemental maps, of the SX CP surface after immersion in molten KCl-$MgCl_2$ at 700 °C for 100 h and subsequent de-salting.

Figure 4.37 displays the EDS elemental maps of the cross-section of pre-oxidized SX without chemical purification. The cross-section shows no evidence of a Si or Cr oxide scale on the surface of the alloy suggesting that both oxides were dissolved during exposure. Cr has been depleted 8.5 µm into the substrate. Cr particles are found on a grain boundary in the substrate. Fe and Ni are unaffected by the exposure to molten chloride salt.

Figure 4.38 displays the EDS elemental maps of the pre-oxidized cross-section of SX immersed with chemical purification. A 0.3 µm Cr oxide scale is detected on the surface of the alloy and there is no evidence of a Si oxide inner scale. A 0.7 µm thick layer composed of Mg and O is present on the surface of the sample. Small Cr particles are found within the Mg and O layer, suggesting that Cr is diffusing out through the Mg and O layer into the salt mixture. A large Cr and Fe rich particle is located on a grain boundary in the cross section. Cr is depleted 5.8 µm into the substrate of the alloy. Ni and Fe are unaffected by the exposure to molten chloride salt.

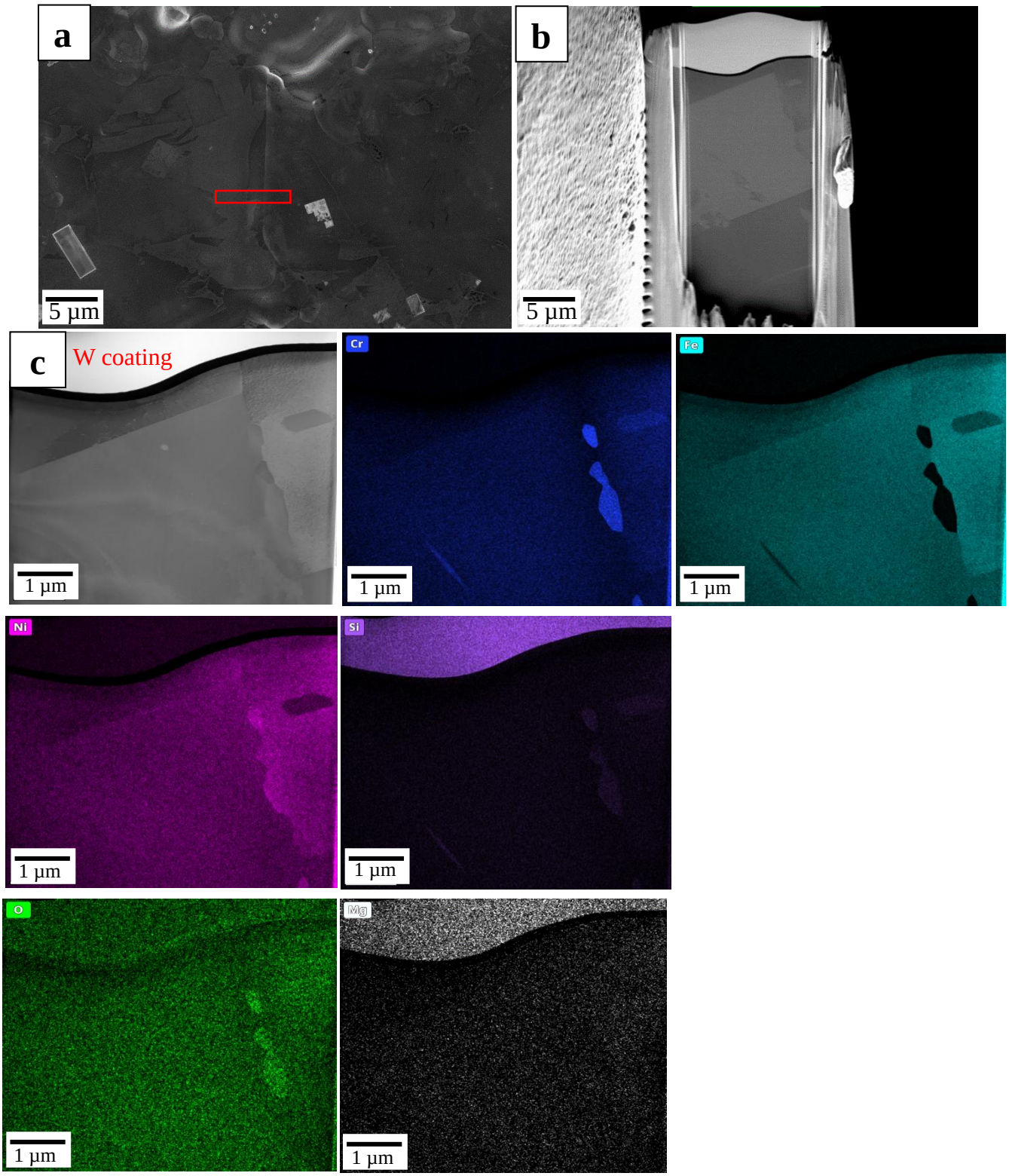

Figure 4.37: (a) Plan view SI image of the SX PO surface after immersion in molten KCl-$MgCl_2$ at 700 °C for 100 h and subsequent de-salting showing site-specific location that was chosen to prepare the thin film cross-section for TEM by FIB milling, (b) SI image of the FIB-prepared thinned cross-section attached to Cu TEM grid, (c) STEM-BSE cross-sectional image, and associated EDS elemental maps, of the surface.

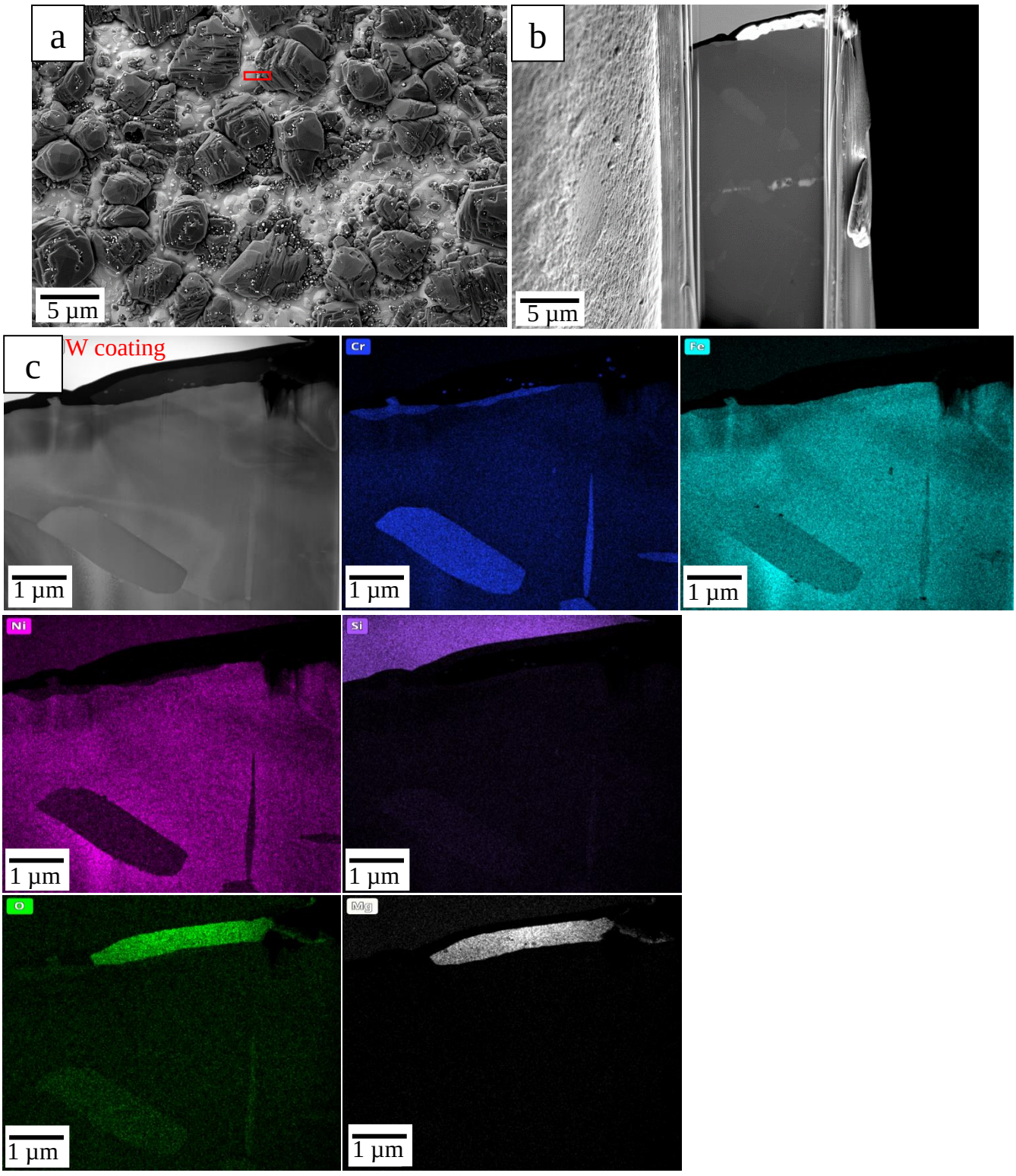

Figure 4.38: (a) Plan view SI image of the SX PO+CP surface after immersion in molten KCl-$MgCl_2$ at 700 °C for 100 h and subsequent de-salting showing site-specific location that was chosen to prepare the thin film cross-section for TEM by FIB milling, (b) SI image of the FIB-prepared thinned cross-section attached to Cu TEM grid, (c) STEM-BSE cross-sectional image, and associated EDS elemental maps, of the surface.

Figure 4.39 displays the EDS depth profiles through the cross-section of UP SX. Cr is depleted 10 µm from the surface. O and Si are enriched at the surface. Particles within the alloy are enriched in Cr, and Si.

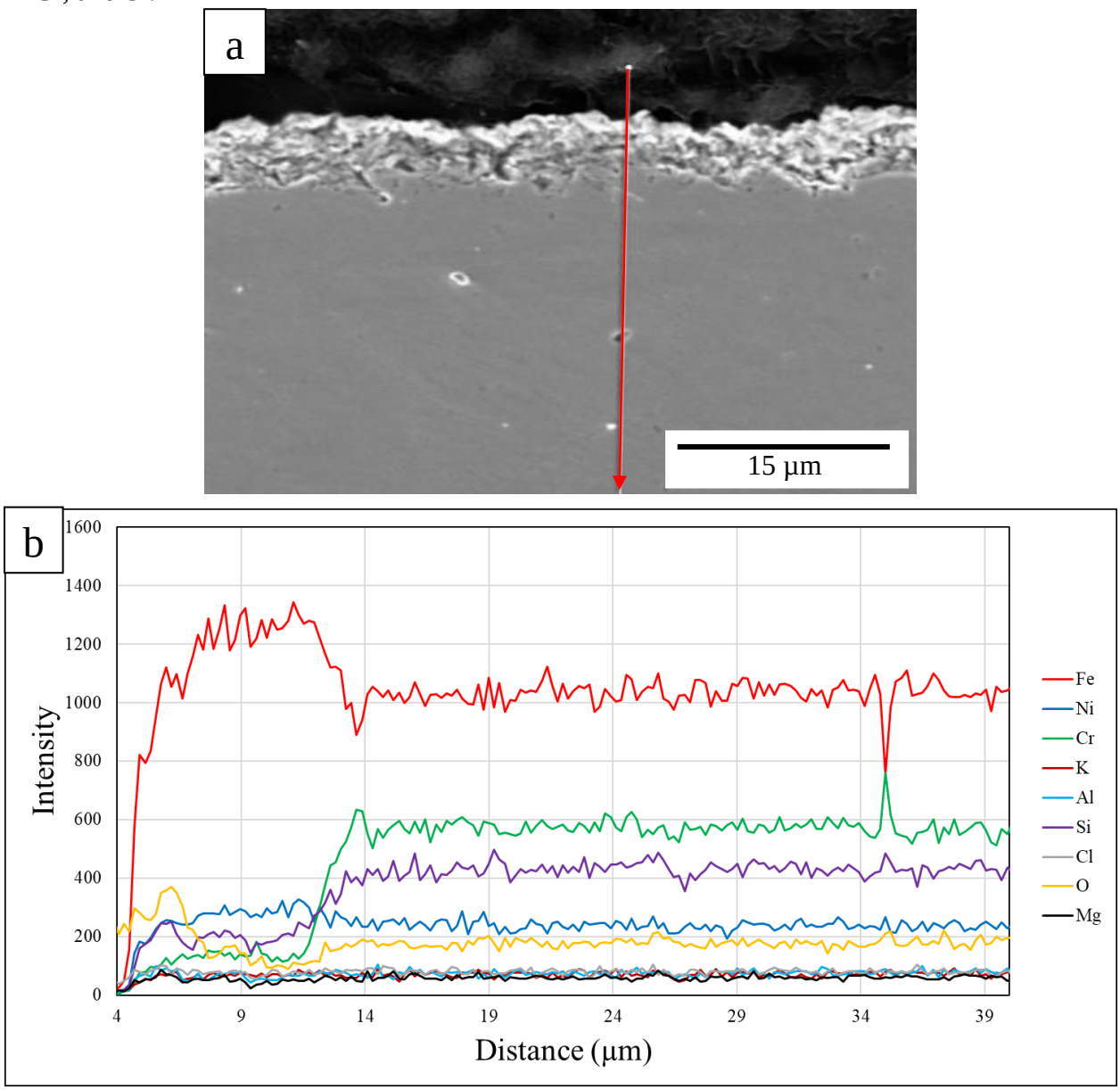

Figure 4.39: (a) BSE cross-sectional image of UP SX after immersion in molten chloride salt mixture at 700 °C for 100 h showing location of the EDS line scan, and (b) set of elemental EDS lines scans acquired through the cross-section.

Figure 4.40 displays the EDS depth profiles through the cross-section of CP SX. Cr is depleted 8 µm from the surface. Particles within the alloy are enriched in Cr, and Si.

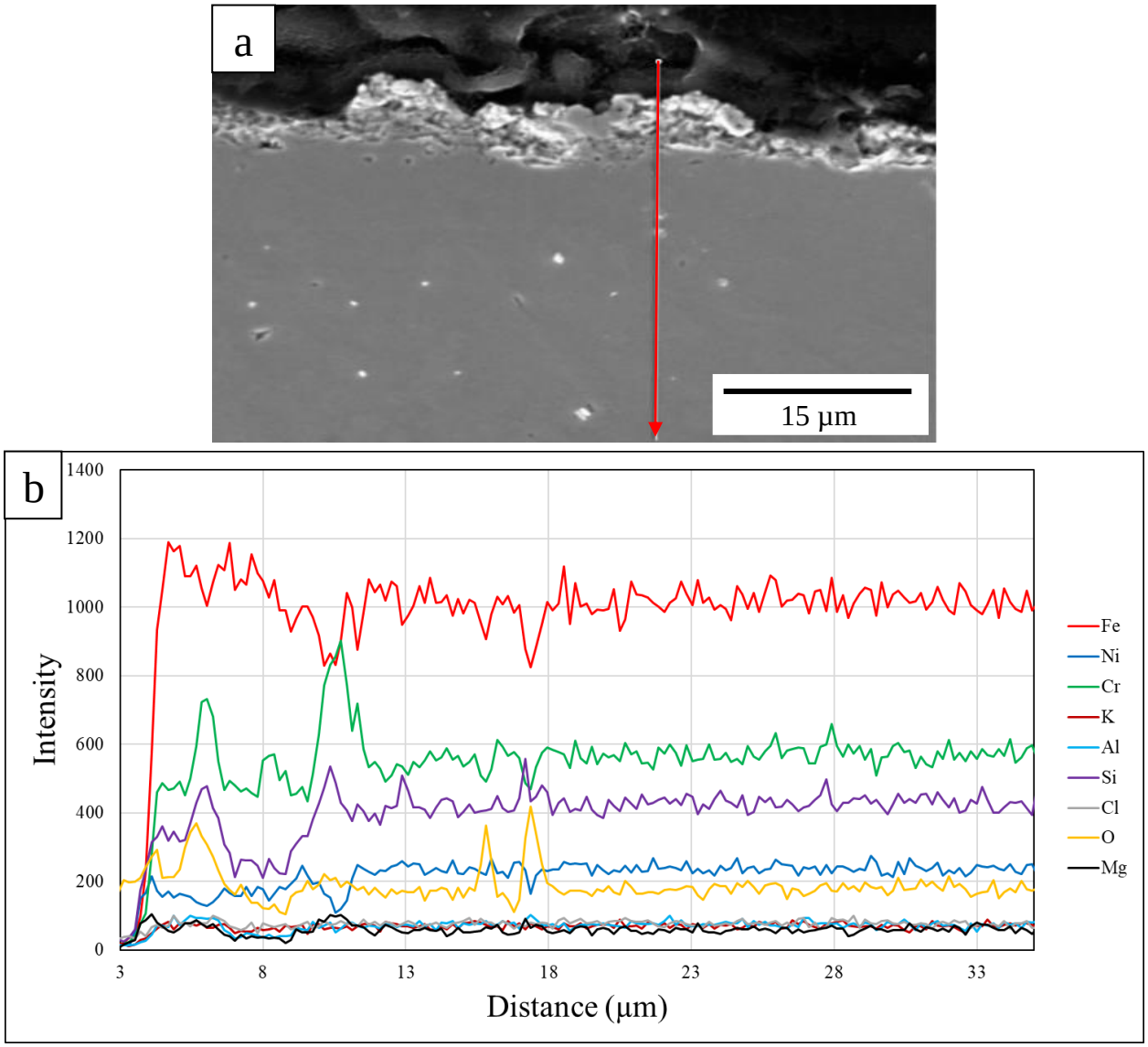

Figure 4.40: (a) BSE cross-sectional image of CP SX after immersion in molten chloride salt mixture at 700 °C for 100 h showing location of the EDS line scan, and (b) set of elemental EDS lines scans acquired through the cross-section.

Figure 4.41 displays the EDS depth profiles through the cross-section of PO SX. Cr is depleted 4 µm from the surface. There is no evidence of a chromia or silica oxide layer beneath the protective W coating. Particles along the grain boundary are enriched in Cr, and Si.

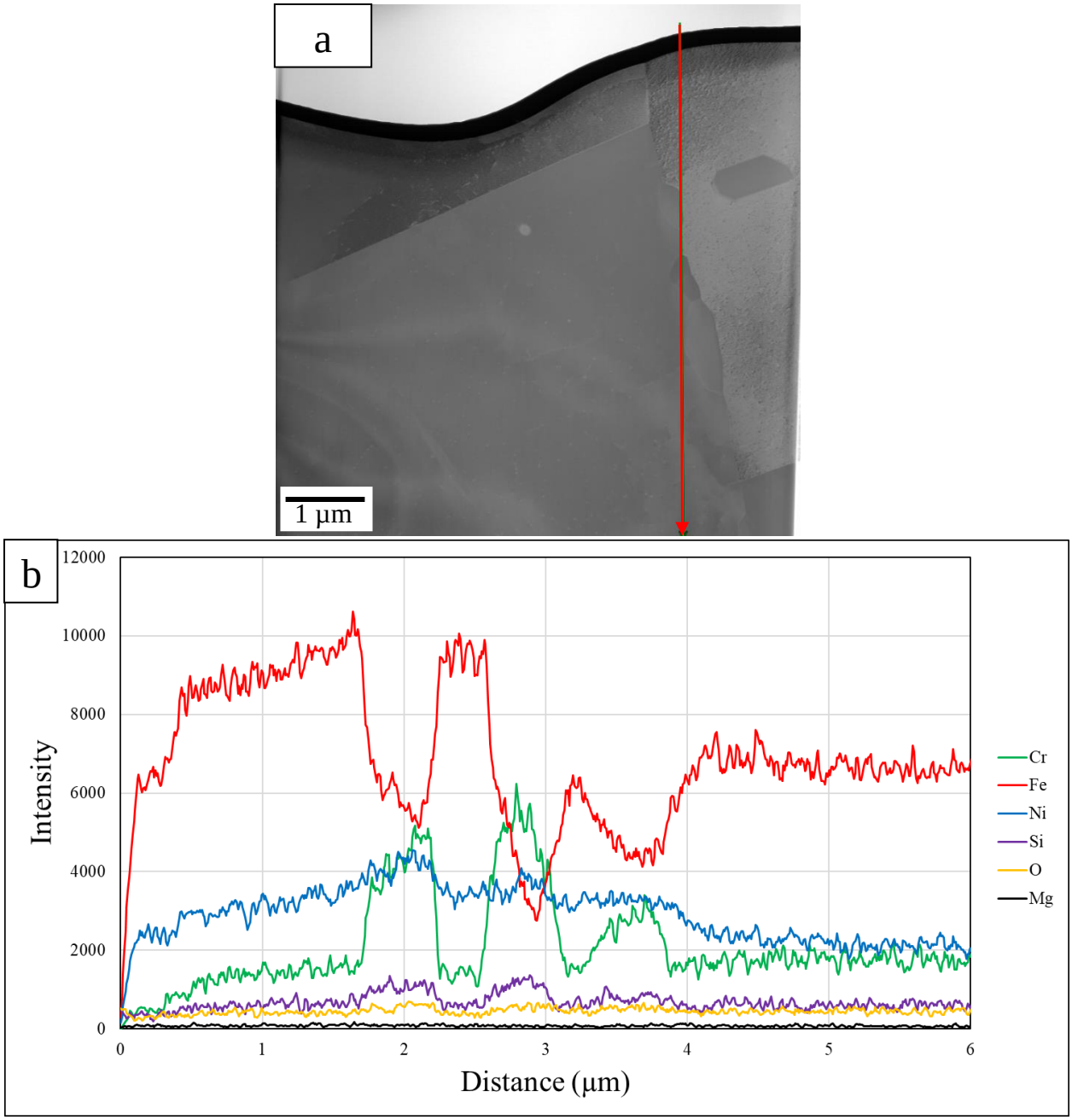

Figure 4.41: (a) BSE cross-sectional image of PO SX after immersion in molten chloride salt mixture at 700 °C for 100 h showing location of the EDS line scan, and (b) set of elemental EDS lines scans acquired through the cross-section.

Figure 4.42 displays the EDS depth profiles through the cross-section of PO+CP SX. Cr is depleted 1.5 µm beneath the oxide layers. There is an outer scale containing Mg and O, and an inner scale containing Cr and O. A small particle is identified withing the Mg and O layer that consists of Cr and Si. A large particle located along a grain boundary is enriched in Cr, and Si.

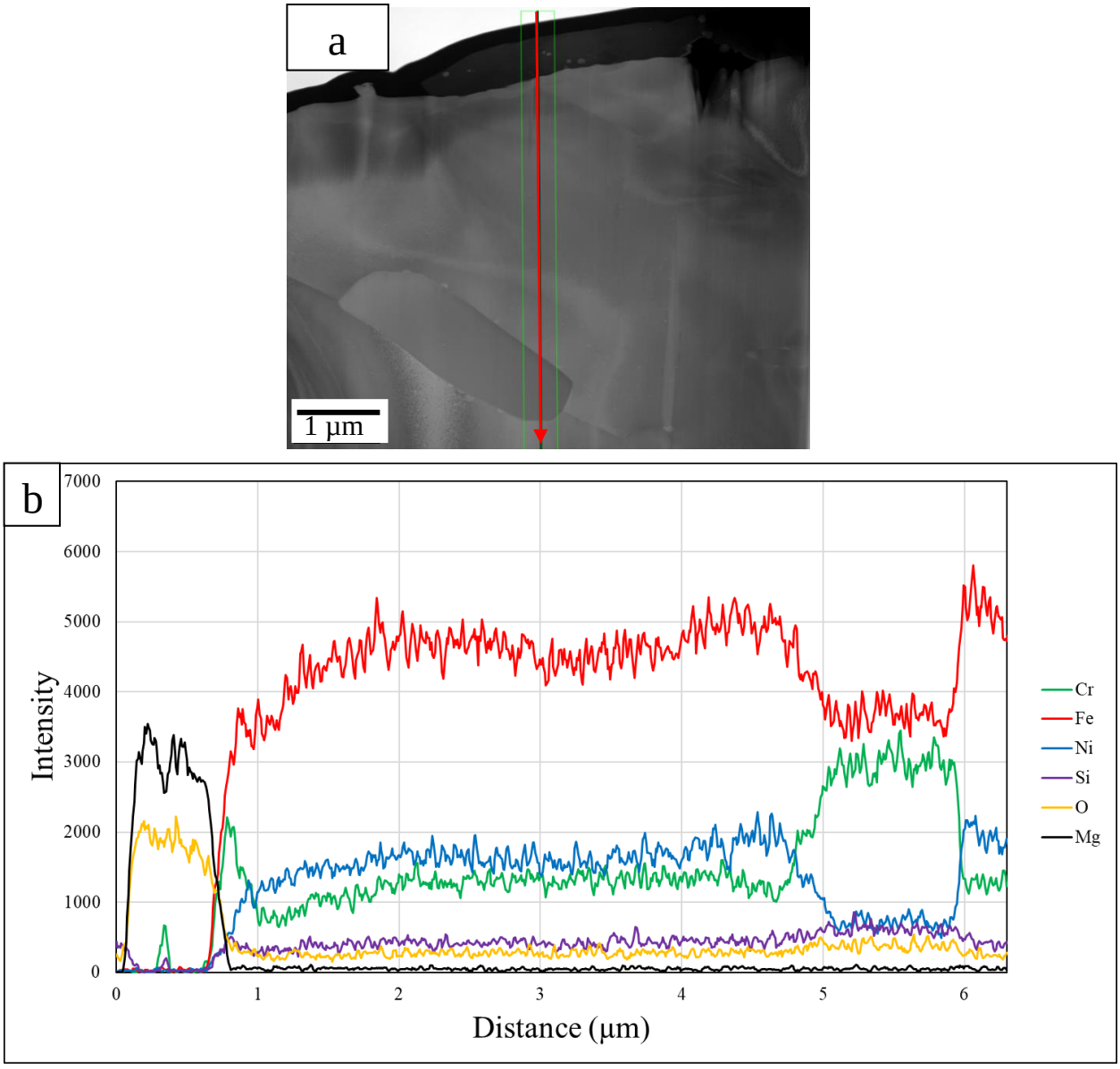

Figure 4.42: (a) BSE cross-sectional image of PO+CP SX after immersion in molten chloride salt mixture at 700 °C for 100 h showing location of the EDS line scan, and (b) set of elemental EDS lines scans acquired through the cross-section.

5.0 Discussion

5.1 Corrosion Comparison Overview

The mass loss of each alloy after immersion in molten KCl-$MgCl_2$ salt was not chosen as the comparable corrosion metric. This is because the corrosion extent could not be sufficiently compared since many of the alloys gained mass due to the growth of an MgO scale as seen in Figures 4.8, 4.20, and 4.32. The metric that was used to determine the corrosion extent of the alloys after immersion in molten KCl-$MgCl_2$ salt with and without the two corrosion control measures (CP and PO) was the difference in Cr intensity between the depleted zone and the bulk of the alloy as shown in Figure 5.1. The Cr intensity is related to concentration; therefore, a higher relative Cr intensity means there is a higher relative Cr concentration. The corrosion extent was determined by calculating the average intensity of Cr in the depleted region (starting from the surface of the alloys, and beneath the oxide scales of the pre-oxidized alloys) and comparing it to the average intensity of the bulk as described by Equation (5.1).

$$Corrosion\ Extent = \frac{(Average\ intensity\ of\ depleted\ zone) - (Average\ intensity\ of\ bulk)}{(Average\ intensity\ of\ bulk)} \times 100\% \qquad 5.1$$

Figure 5.1 reveals that the best performing condition is CP, PO+CP, and CP for I800H, H214, and SX respectively.

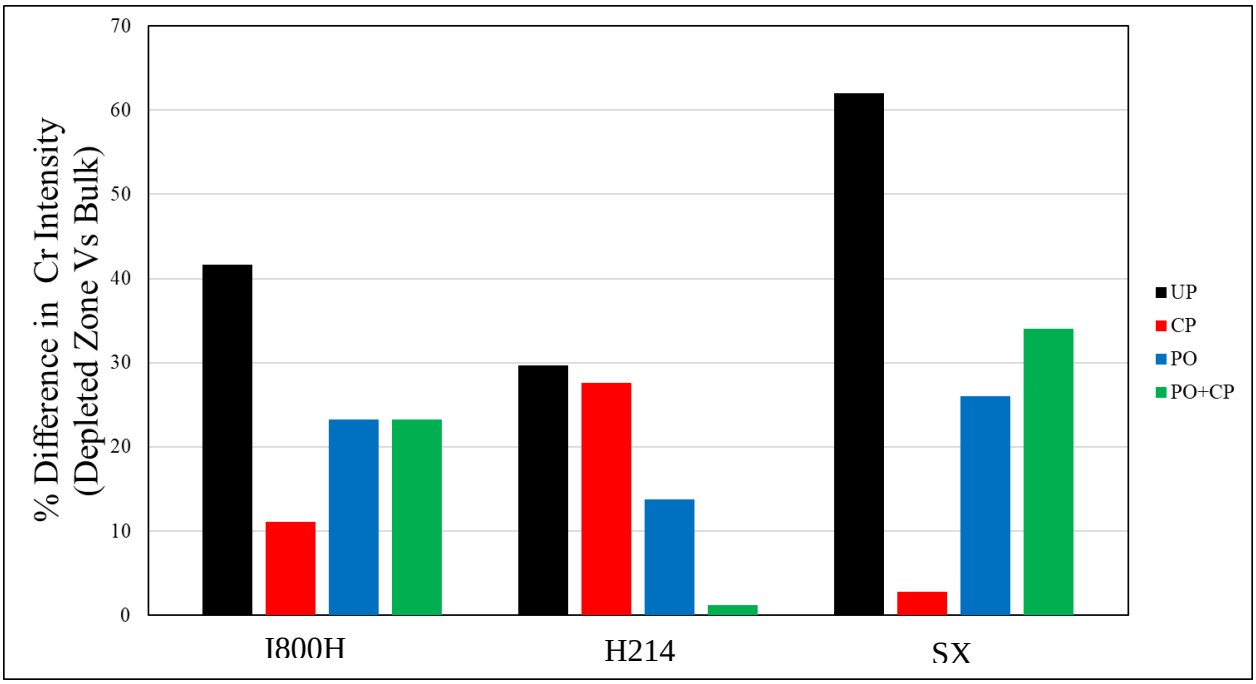

Figure 5.1: Difference in Cr intensity between depleted zone and the bulk after immersion in KCl-$MgCl_2$ salt at 700 °C with and without the corrosion control measures (UP = unprotected, CP = chemical purification (Mg metal addition), and PO = thermally pre-oxidized).

Table 5.1 presents the extent of corrosion inhibition of the two corrosion control measures, relative to the UP case based on the difference in Cr intensity presented in Figure 5.1. CP significantly increases the intensity of Cr of I800H and SX. This aligns well with research done by Ding *et al.* [5], Zhao *et al.* [9], and D'Souza *et al.* [10] that show how adding a Mg metal as a corrosion inhibitor to the molten chloride salt mixture is an effective method to mitigate corrosion of Cr-containing alloys. PO and PO+CP significantly increase the intensity of Cr in H214. Therefore, the alumina scale that formed during PO provides better protection against corrosion than the native oxide scale formed on the UP alloy. This aligns well with research done by Ding *et al.* [5], and Gomez-vidal *et al.* [11] that show how alumina scales effectively resist the preferential depletion of Cr.

Table 5.1: Corrosion inhibition of CP, PO, and PO+CP relative to UP based on the difference in Cr intensity between the depleted zone and the bulk.

	Corrosion Inhibition Efficiency (%)		
Alloy	**CP**	**PO**	**PO+CP**
I800H	73.3	44.0	44.0
H214	7.1	53.5	96.0
SX	95.5	58.1	45.2

Figure 5.2 displays the depth profiles of Cr through the cross-sections of I800H immersed in molten KCl-$MgCl_2$ salt mixtures. The intensity of Cr in the depleted zone is much greater for the CP alloy relative to the UP alloy. PO+CP has a stronger Cr intensity in the depleted zone relative to the PO alloy.

Figure 5.3 displays the depth profiles of Cr through the cross-sections of H214 after immersion in the molten KCl-$MgCl_2$ salt mixture. UP has a stronger Cr intensity than CP in the depleted zone. PO and PO+CP have about 5 μm and 0 μm of Cr depletion beneath the oxide scales respectively.

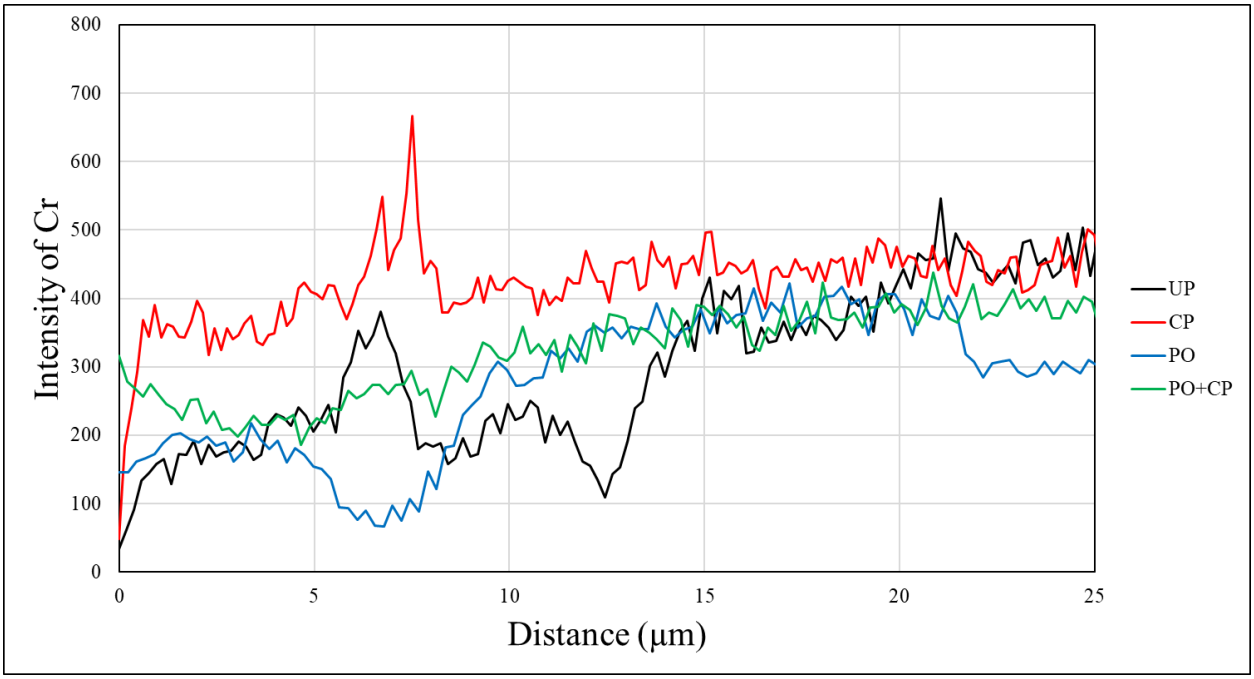

Figure 5.2: Set of Cr EDS lines scans acquired through the cross-sections of I800H.

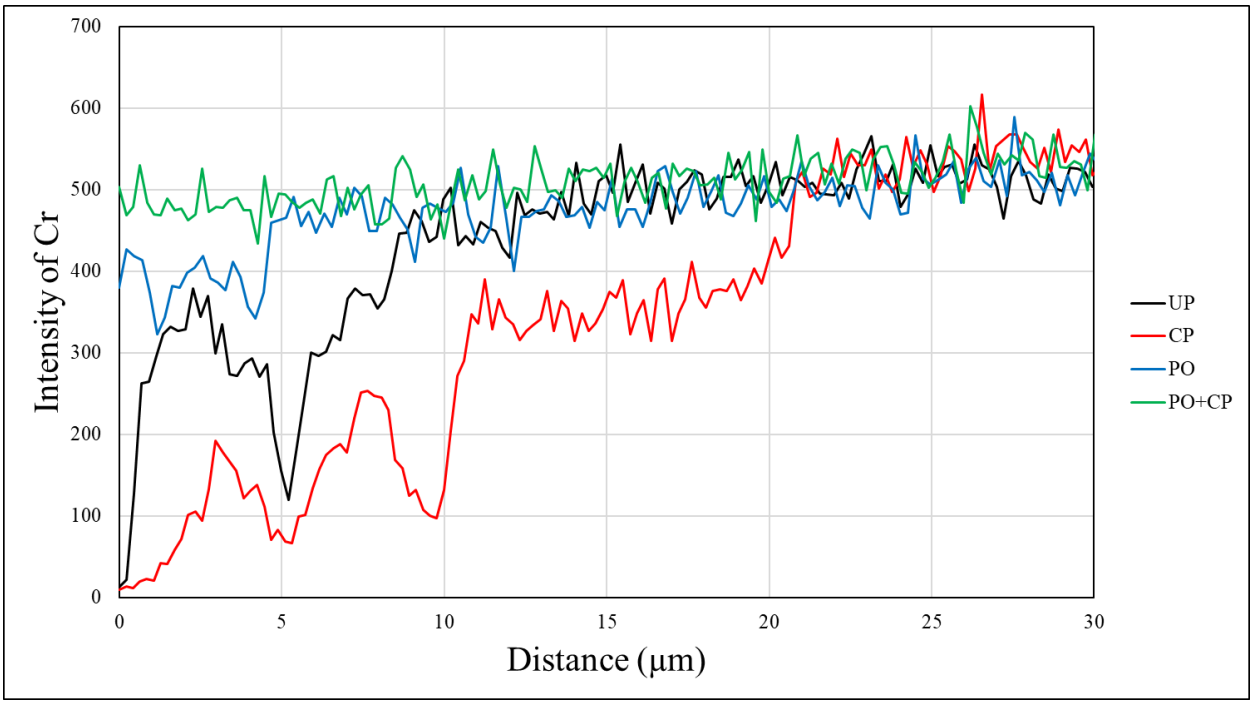

Figure 5.3: Set of Cr EDS lines scans acquired through the cross-sections of H214.

Figure 5.4 displays the depth profiles of Cr through the cross-sections of UP and CP SX after immersion in molten KCl-$MgCl_2$ salt mixtures. UP has a significantly lower intensity of Cr in the depleted zone relative to the CP case.

Figure 5.5 displays the depth profiles of Cr through the cross-sections of PO and PO+CP SX after immersion in the molten KCl-$MgCl_2$ salt mixture. Cr is enhanced in three regions of the PO SX sample indicating the scan has passed through a Cr particle along the grain boundary as seen in Figure 4.41 (a). PO and PO+CP have a significantly lower intensity of Cr through the cross-section relative to the UP and CP cases. The PO and PO+CP line scans were acquired through the cross-sections of TEM prepared samples, therefore the distance is much shorter compared to the UP and CP samples where the line scans were acquired using SEM-EDS.

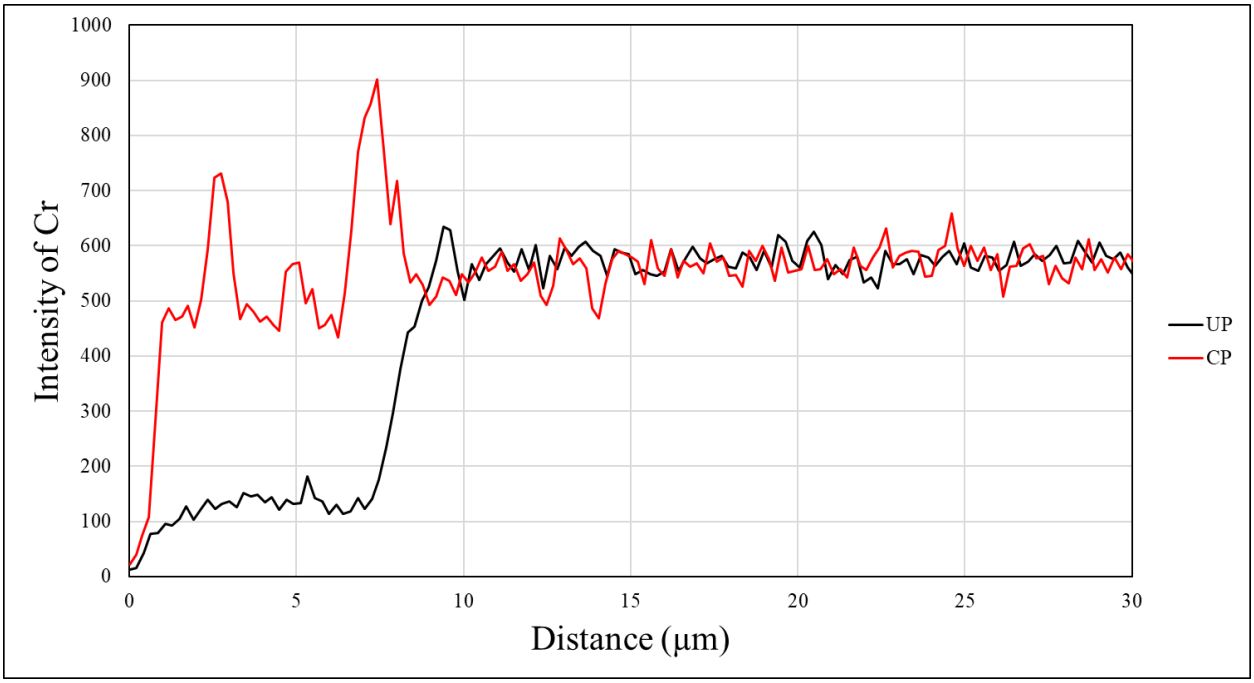

Figure 5.4: Set of Cr EDS lines scans acquired through the cross-sections of UP and CP SX.

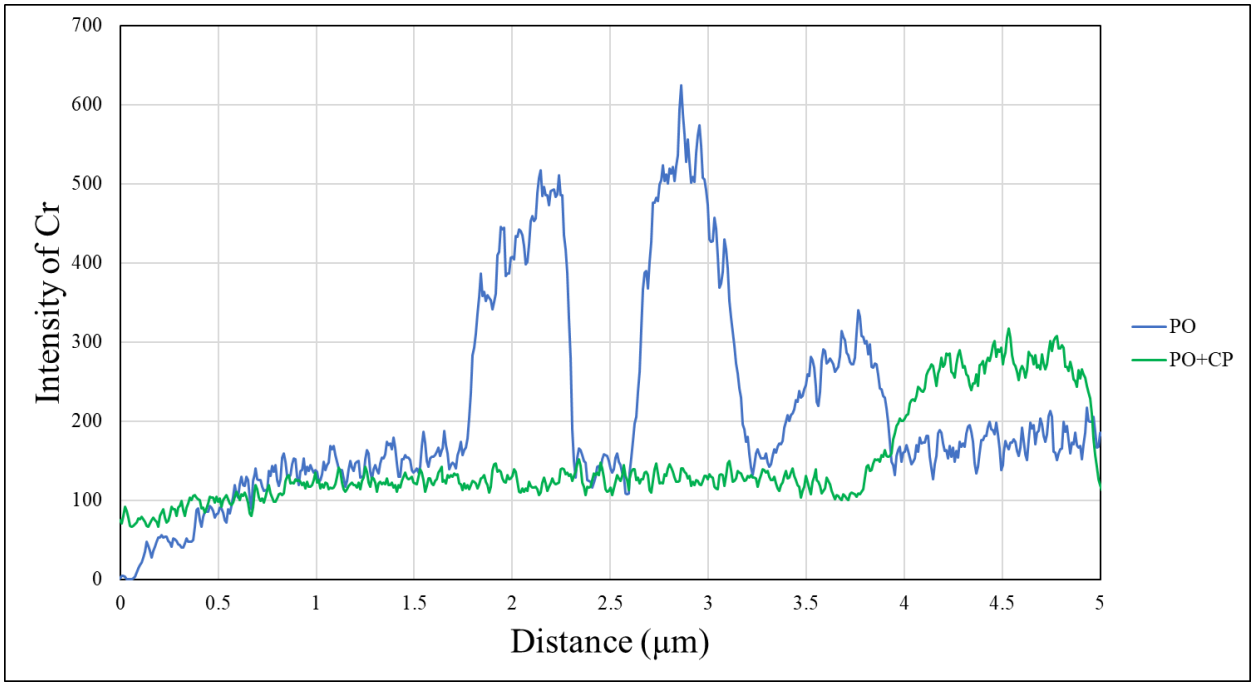

Figure 5.5: Set of Cr EDS lines scans acquired through the cross-sections of PO and PO+CP SX.

Figure 5.6 displays the depth of Cr depletion zone for each alloy after immersion in molten KCl-$MgCl_2$. The depth of Cr depletion was measured starting from the surface of the alloys, and beneath the oxide scales of the PO alloys. Each UP alloy had the largest depth of Cr depletion compared to the corrosion inhibition conditions. The best performing corrosion control measure was CP, PO+CP, and PO+CP for I800H, H214, and SX respectively. PO+CP H214 had the least amount of Cr depletion, since Cr was unaffected beneath the alumina scale as shown in Figure 5.3.

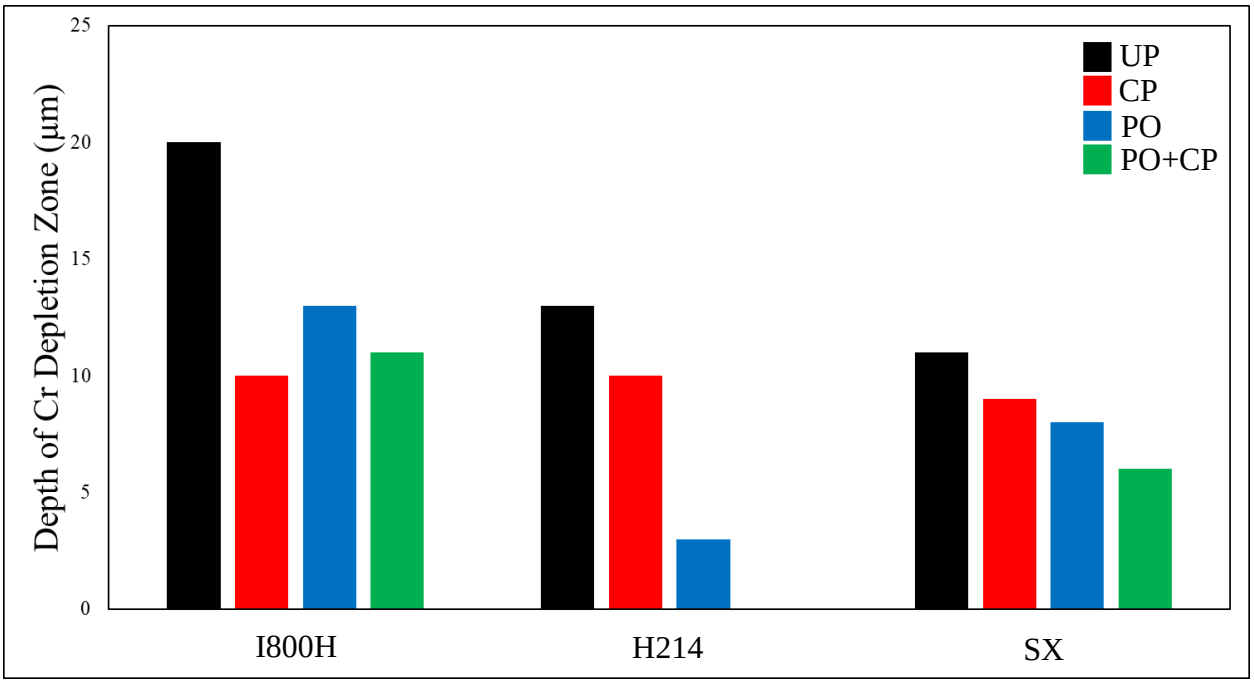

Figure 5.6: Depth of Cr depletion zone after immersion in KCl-$MgCl_2$ salt at 700 °C with and without the corrosion control measures (UP = unprotected, CP = chemical purification (Mg metal addition), and PO = thermally pre-oxidized).

Table 5.2 presents the extent of corrosion inhibition of the two corrosion control measures, relative to the UP case based on the depth of Cr depletion presented in Figure 5.6. These results generally follow the same trend as Table 5.1, which is that the best performing alloys are CP I800H, PO+CP H214, and PO+CP SX.

Table 5.2: Corrosion inhibition of CP, PO, and PO+CP relative to UP based on the depth of Cr depletion.

	Corrosion Inhibition Efficiency (%)		
Alloy	**CP**	**PO**	**PO+CP**
I800H	50	35	40
H214	21.5	71.4	100
SX	16.7	25	50

5.2 Corrosion Control

5.2.1 UP

It is well known that covalent metal halides like $MgCl_2$ are easily hydrated when in contact with air or moisture due to their strong hygroscopicity [5, 9-10]. As a result, oxidizing impurities are produced due to hydrolysis reactions that occur at elevated temperatures as described by Equations (5.2) to (5.4) [5, 9-10].

$$MgCl_2 + H_2O \rightarrow MgOHCl + HCl(g) \quad 5.2$$

$$MgOHCl \rightarrow MgO + HCl(g) \quad 5.3$$

$$MgOHCl \rightarrow MgOH^+ + Cl^- \quad 5.4$$

Each alloy exposed to KCl-$MgCl_2$ salt mixture corroded when unprotected (UP). Cr depletion was observed in each alloy with and without CP. Cr has the most negative electromotive force (EMF) value of the set of major alloying elements present in the three commercial alloys studied, and therefore is preferentially dissolved into the molten chloride salt mixture, as shown in Equations (5.5) and (5.6).

$$Cr\ (s) + 2MgOH^+ \rightarrow Cr^{2+} + 2MgO(s) + H_2(g) \quad 5.5$$

$$Cr\ (s) + 2HCl\ (g) \rightarrow CrCl_2(g) + H_2(g) \quad 5.6$$

Cr depletion is observed in each alloy after immersion in molten KCl-$MgCl_2$ salt mixture as shown in Figure 5.6. The alloy that performed the best in the UP case was H214 since it has the lowest difference in Cr intensity between the depleted zone and the bulk. This can be explained by comparing the bulk compositions of each alloy. H214 has the highest Ni content, lowest Fe, and

lowest Cr content. Previous research has shown that alloys with higher Ni content perform better in molten chloride salt mixtures than alloys with high Fe and Cr content [34-36, 38-40, 95]. This is because Ni has the least negative Gibbs free energy of metal chloride formation, therefore it is less prone to selective dissolution from a driving force perspective.

5.2.2 CP

Mg metal acts as a corrosion inhibitor because it preferentially reacts with the produced corrosive impurities in a molten $MgCl_2$-containing salt as described by Equation (5.7) [5, 9-10].

$$Mg + 2MgOH^+ \rightarrow Mg^{2+} + 2MgO(s) + H_2(g) \qquad 5.7$$

The corrosion layers are greatly reduced when a Mg inhibitor was present in the molten salt mixture considered herein, but corrosion was still observed in all three alloys after immersion. This could be because the excess Mg metal drives the hydrolysis reaction (Equation (5.2)), and the dissolved excess Mg cations drive Equation (5.7) based on Le Chatelier's Principle. Therefore, corrosion is dependent on the rate of MgOHCl formation, as well as the rate of $MgOH^+$ consumption.

A considerable amount of MgO is produced as seen in Equations (5.2) to (5.7). The SEM-EDS cross-sectional analysis of the alloys exposed with CP revealed a thin MgO layer on each surface. XRD identified this layer to be MgO. MgO has a low solubility in molten chlorides [88-89], therefore it tends to precipitate as a MgO layer on the surface of the alloys. The precipitation of MgO onto the alloy surfaces accounts for the recorded weight gain of alloys when exposed in the UP condition. MgO has a porous structure [3] but may act as a semi-protective diffusion barrier against the molten chloride salt mixture.

The alloy that performed the best with CP as the corrosion control measure was SX because it had the smallest difference in Cr intensity between the depleted zone and the bulk. The improved protection of SX may be attributed to the massive polyhedral structures (0.2-0.5 mm in length) distributed on the surface of the alloy as seen in Figure 5.7 (a). Figure 5.7 (b) displays EDS elemental maps of these structures which reveal that they are composed of mainly Ni and Si. Cross-sectional examination of CP SX shows enrichment of Ni, Fe, Mg, and O at the surface as seen in Figure 4.36. Enrichment of the more noble metals (Ni, Fe) at the surface may provide better protection to SX relative to the other alloys in the CP condition.

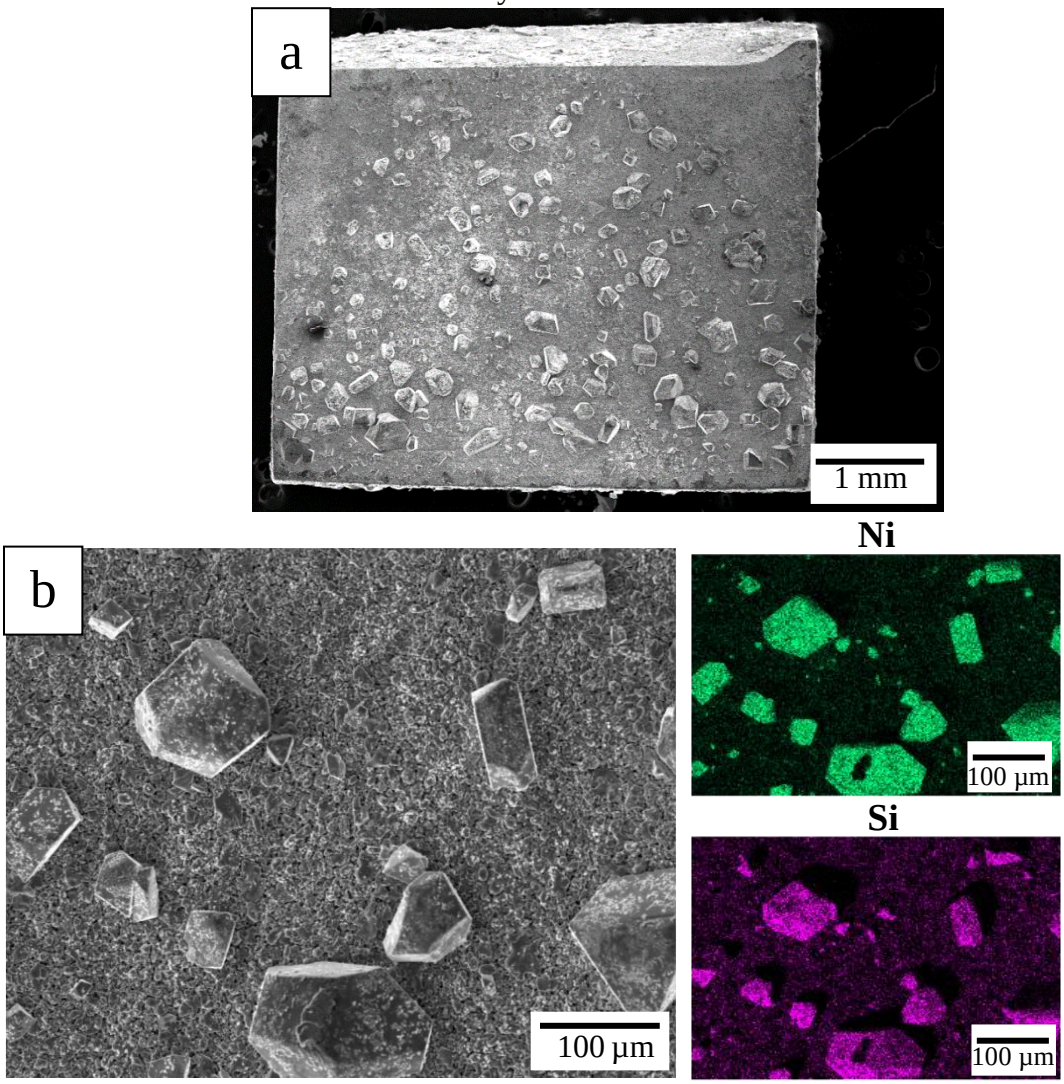

Figure 5.7: (a) low magnification SEI image of the surface of UP SX immersed with CP and (b) associated BSE image and EDS elemental maps.

5.2.3 PO

Figure 5.8 displays a schematic of the oxides presumed to have formed on each alloy during PO treatment. EDS line scans through the cross-section of I800H after PO reveal an oxide scale that was enriched in Cr. Literature shows that Cr_2O_3 is a common scale formed on I800H [96-97] and that intergranular oxidation is common in this alloy [98]. EDS line scans through the cross-section of H214 reveal two distinct layers: an inner layer composed of Al and O as major scale forming elements, and an outer layer enriched in Cr, Ni, Al, and O. Literature shows that $Ni(Al,Cr)_2O_3$ is commonly formed as an outer layer, and Al_2O_3 as an inner layer during air oxidation of this alloy [64-65]. EDS line scans through the cross-section of SX after PO show an outer oxide scale composed of Cr and O as a major scale forming elements, and an inner scale composed of Si and O as a major scale forming elements. Little research has been done on the air oxidation of this alloy, but many studies show that SiO_2 is the common scale that is formed on alloys with high Si compositions [62, 99-100].

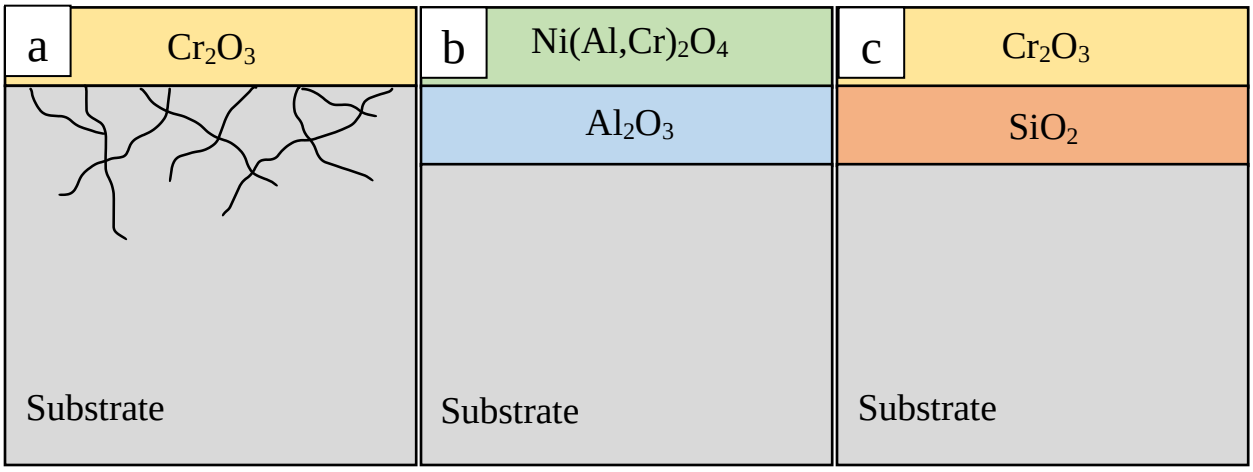

Figure 5.8: Schematic of formed oxides on (a) I800H, (b) H214, and (c) SX during pre-oxidation treatment.

I800H suffered intergranular oxidation that extended 14 µm into the substrate after PO. The intergranular oxidation grew an additional 15 µm after immersion in molten KCl-$MgCl_2$ salt mixture without CP, and no additional growth with CP. SEM-EDS cross-sectional analysis of I800H with PO revealed severe Cr depletion from the substrate and along the grain boundaries. Intergranular oxidation may have acted as an easier path for Cr species to diffuse out of the alloy substrate. Mg and O were observed in the Cr oxide layer indicating the instability of the scale. Cr_2O_3 has a high dissolution rate in molten KCl-containing salts because of the formation of chromate compounds via Equation (5.8) [12, 62].

$$4KCl(s,l) + Cr_2O_3(s) + \frac{5}{2}O_2(g) \rightarrow 2K_2CrO_4(s) + 2Cl_2(g) \qquad 5.8$$

Chromate compounds possess a high solubility in molten salts and consequently the Cr_2O_3 layer readily reacts [12, 91], which leaves a partially dissolved scale. Such a situation allowed for $MgOH^+$ and HCl corrodants to penetrate through the porous Cr_2O_3 layer and react with the substrate. Intergranular oxidation did not grow in I800H when CP was included in the salt mixture. This suggests that CP helped to control corrosion via internal oxidation.

H214 was the best performing alloy of the three with PO as the corrosion control measure because the Al_2O_3 formed was effective in mitigating the penetration of O and Mg species into the substrate and resisted the diffusion of Cr out of the matrix. Cr, Fe, and Ni were unaffected beneath the Al_2O_3 scale during immersion in molten chloride salt mixtures. A dense Al_2O_3 layer is more protective at high temperatures compared to SiO_2 and Cr_2O_3 due to its thermodynamic stability, as displayed in Figure 5.9 [5, 92, 94].

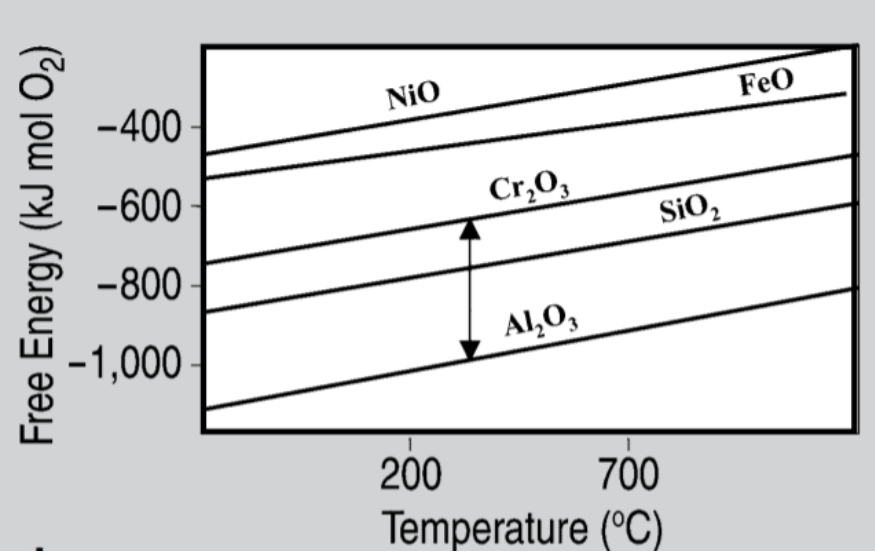

Figure 5.9: Gibbs free energy of oxide formation of common oxides [94].

The improved protection imparted by Al_2O_3 compared to Cr_2O_3 can also be attributed to its slower growth rate at 1000°C, as demonstrated in Figure 5.10.

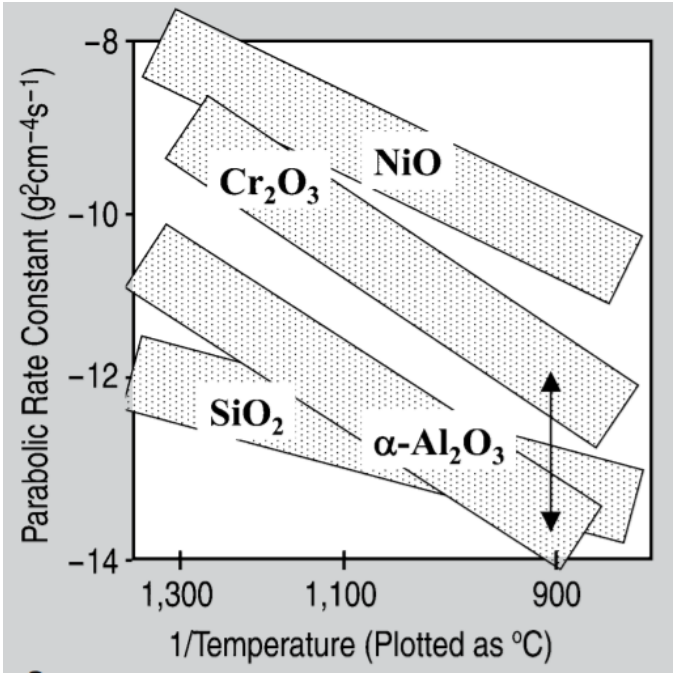

Figure 5.10: Schematic representation of the growth rate of common oxides [94].

H214 with PO but without CP showed an increase in Al_2O_3 thickness of approximately 0.5-1 µm. This indicates that there is a presence of O-containing oxidant in the molten chloride salt mixture since O is required for the further growth beyond what PO alone provided. The Al_2O_3 layer remains the same thickness with CP, suggesting that the purification technique is effectively removing the O-containing oxidant (MgOHCl).

The cross-sectional analysis of SX with PO revealed a completely dissolved SiO_2 layer without CP, and only a small Cr_2O_3 layer remained on the alloy with CP. The cross section of SX with PO and CP indicates that Cr particles moved through the MgO layer, suggesting the formation of a porous MgO layer. The dissolution of these oxide layers left the bare metal exposed to the molten salt and resulted in considerably higher corrosion. The higher corrosion of SX with PO relative to UP case is ascribed to the formation of Mg_2Si. The SiO_2 scale can react with Mg to form the Mg_2Si intermetallic phase, as described by Equation (5.9):

$$SiO_2 + 4Mg = Mg_2Si + 2MgO \qquad 5.9$$

The Mg_2Si product can react with water and HCl to form a gas that will diffuse away from the alloy and into the salt mixture.

$$Mg_2Si + 2H_2O = SiH_4 + 2MgO \qquad 5.10$$

$$Mg_2Si + 4HCl = SiH_4 + 2MgCl_2 \qquad 5.11$$

These reactions were observed by Kipouros et al. [93] during the production of Mg metal via electrolysis of molten KCl-$MgCl_2{\cdot}6H_2O$ salts. It was found that the container materials experienced substantial mass loss due to Si impurities that formed from the reaction of the SiO_2 layer and the Mg which resulted in the formation of SiH_4 that was detected in the vented gases.

6.0 Conclusion

The objectives of this research were to determine the relative corrosion performance of high temperature alloys with different protective scale forming tendencies when exposed to molten KCl-$MgCl_2$ salt mixture. The corrosion performance was investigated using two corrosion mitigation methods, relative to the unprotected (UP) case: chemical purification (CP) of the molten salt mixture by Mg metal additions to render it less corrosive, and thermal pre-oxidation (PO) of the alloys to render them less prone to corrosion. Based on the results presented and discussed, the following conclusions are extracted:

1. Mass loss was determined to be an unsuitable comparable corrosion metric since many alloys gained mass due to the growth of a MgO scale.
2. Each UP alloy experienced corrosion in the form of selective removal of Cr due to reactivity with impurities within the molten chloride salt mixture. The UP alloy that performed the best was H214, followed by I800H and SX. The metrics that were used to compare corrosion extent were the depth of Cr depletion and difference in Cr intensity between the Cr depletion zone and the bulk. H214 was the best performing UP alloy because of its high Ni, and low Cr and Fe content.
3. Adding 1.7 wt % Mg as a corrosion inhibitor (corrosion control by CP) significantly increased the concentration (energy intensity) of Cr in the depleted zone and decreased the depth of Cr depletion zone of each alloy. CP inhibits corrosion because the added Mg metal preferentially reacts with impurities in the molten chloride salt mixture that were formed by hydrolysis reactions between residual water and the molten salt. The CP alloy that performed the best was SX, followed by I800H and H214 respectively based on the

comparable corrosion metrics. SX with CP performed the best because of large polyhedral shaped crystals composed of Ni and Si that formed on the surface and acted as a barrier to inhibit corrosion. The addition of Mg metal in the salt mixture resulted in the precipitation of MgO on the surface of each alloy. The oxide deposition of MgO on components may impact the thermal and mechanical performance of the system. Therefore, the addition of Mg should be optimized for use in an operational system.

4. The PO and PO+CP alloy that performed the best was H214 followed by I800H and SX based on the comparable corrosion metrics. H214 performed the best because alumina is more stable than chromia and silica in molten chloride salt, and therefore resists the diffusion of Cr out of the substrate, and the penetration of corrosive species. Pre-oxidation treatment is not considered ideal for I800H due to the intergranular oxidation that formed during heat treatment. The chromia scale formed on I800H and SX readily reacted with KCl, leaving a partially dissolved scale that allowed corrodants to penetrate through the porous layer. The silica scale formed on SX after pre-oxidation treatment was not corrosion resistant to molten chloride salt mixtures due to the reaction between SiO_2 and Mg.

7.0 References

[1] Government of Canada, "Canadian Net-Zero Emissions Accountability Act," edited August 2021, accessed on September 21, 2021, available at: <https://www.canada.ca/en/services/environment/weather/climatechange/climate-plan/net-zero-emissions-2050/canadian-net-zero-emissions-accountability-act.html>

[2] Natural Resources Canada, "Canada's Small Modular Reactor Action Plan," edited February 2021, accessed on September 21, 2021, available at: <https://www.nrcan.gc.ca/our-natural-resources/energy-sources-distribution/nuclear-energy-uranium/canadas-small-nuclear-reactor-action-plan/21183>

[3] J. Frye, W. Manly, J. Cunningham, "Metallurgy Division Annual Progress Report," Oak Ridge National Laboratory, Oak Ridge, TN, December 1957.

[4] Terrestrial Energy, "IMSR® Technology", 2021, accessed on September 24, 2021, available at: <https://www.terrestrialenergy.com/technology/>

[5] W. Ding, H. Shi, A. Jianu, "Molten Chloride Salts for Next Generation CSP Plants: Mitigation strategies against corrosion of structural materials," Solar Energy Materials and Solar Cells, 193, 2019, pp. 298-313.

[6] M. Mehos, C. Turchi, J. Vidal, "Concentrating Solar Power Gen3 Demonstration Roadmap," National Renewable Energy Laboratory, Technical Report: NREL/TP-5500-67464, 2017.

[7] J.W. Koger, "Effect of FeF_2 Addition on Mass Transfer in a Hastelloy-N – Li-BeF_2-UF_4 Thermal Convection Loop System", Oak Ridge National Laboratory, Oak Ridge, TN, December 1972.

[8] L.C. Olson, J.W. Ambrosek, K. Sridharan, M.H. Anderson, T.R. Allen, "Materials corrosion in molten LiF-NaF-KF salt", Journal of Fluorine Chemistry, 130, 2009, pp. 67-73.

[9] Y. Zhao, N. Klammer, J. Vidal, "Purification strategy and effect of impurities on corrosivity of dehydrated carnallite for thermal solar applications," Royal Society of Chemistry, 9, 2019, 41664.

[10] B. D'Souza, W. Zhuo, Q. Yang, "Impurity driven corrosion behaviour of HAYNES® 230 alloy in molten chloride salt," Corrosion Science 187, 2021, 109483.

[11] J. Gomez-Vidal, A. Fernandez, R. Tirawat, "Corrosion resistance of alumina-forming alloys against molten chlorides for energy production. I: Pre-oxidation treatment and isothermal corrosion tests," Solar Energy Materials & Solar Cells, 166, 2017, pp. 222-233.

[12] S. Kassim, J. Thor, A. Seman, "High temperature corrosion of Hastelloy C22 in molten alkali salts: The effect of pre-oxidation treatment," Corrosion Science, 173, 2020, 108761.

[13] M. Alzamani, K. Jafarzadeh, "The Effect of Pre-Oxidation Treatment on Corrosion Behavior of Ni-Cu-Fe-Al Anode in Molten $CaCl_2$ Salt," Oxidation of Metals, 89, 2018, pp. 623-640.

[14] S. Boghosian, A. Godo, H. Mediaas, W. Ravlo, T. Ostvold, "Oxide Complexes in Alkali-Alkaline-Earth Chloride Melts," Acta Chemica Scandinavica, 45, 1991, pp. 145-157.

[15] J. Lehmusto, P. yrjas, L. Hupa, “Pre-oxidation as a Means to Increase Corrosion Resistance of Commercial Superheater Steels,” Oxidation of Metals, 91, 2019, pp. 311-326.

[16] Q. Liu, Z. Wang, W. Liu, H. Yin, Z. Tang, “Ni-Mo-Cr alloy corrosion in molten NaCl-KCl-$MgCl_2$ salt and vapour,” Corrosion Science, 180, 2021, 109183.

[17] S. Bell, T. Steinberg, G. Will, “Corrosion mechanisms in molten salt thermal energy storage for concentrating solar power,” Renewable and Sustainable Energy Reviews, 114, 2019, 109328.

[18] S. Okoro, M. Kvisgaard, M. Montgomery, F. Frandsen, K. Pantleon, “Pre-oxidation and its effect on reducing high-temperature corrosion of superheater tubes during biomass firing,” Surface Engineering, 33, 2016, pp. 428-432.

[19] H. Yin, L. Gao, H. Zhu, X. Mao, F. Gan, D. Wang, “On the development of metallic inert anode for molten $CaCl_2$-CaO System,” Electrochimica Acta, 56, 2011, pp. 3296-3302.

[20] D.F. Williams, “Assessment of Candidate Molten Salt Coolants for the NGNP/NHI Heat-Transfer Loop”, Oak Ridge National Laboratory, Oak Ridge, TN, June 2006.

[21] W. Ding, A. Bonk, T. Bauer, “Corrosion behavior of metallic alloys in molten chloride salts for thermal energy storage in concentrated solar power plants: A review,” Frontiers of Chemical Science and Engineering, 12, 2018, pp. 564-576.

[22] S. Guo, J. Zhang, W. Wu, W. Zhou, “Corrosion in the molten fluoride and chloride salts and materials development for nuclear applications,” Progress in Materials Science, 97, 2018, pp. 448-487.

[23] K. Sridharan, T. Allen, “Corrosion in Molten Salts,” Molten Salts Chemistry, Chapter 12, Elsevier, 2013, pp. 241-267.

[24] T. Ong, M. Sarvghad, K. Lippiatt, L. Griggs, H. Ryan, G. Will, T. Steinberg, “Review of the solubility, monitoring, and purification of impurities in molten salts for energy storage in concentrated solar power plants,” Renewable and Sustainable Energy Reviews, 131, 2020, 110006.

[25] W. Ding, A. Bonk, J. Gussone, T. Bauer, “Electrochemical measurement of corrosive impurities in molten chlorides for thermal energy storage,” Journal of Energy Storage, 15, 2018, pp. 408-414.

[26] W. Ding, A. Bonk, G. Gussone, T. Bauer, “Electrochemical method for monitoring corrosive impurities in molten $MgCl_2$/KCl/NaCl salts for Thermal Energy Storage,” Conference Paper, 11th International Renewable Energy Storage Conference, Dusseldorf, Germany, 2017.

[27] S. Ren, Y. Chen, X. Ye, L. Jiang, S. Yan, J. Liang, “Corrosion behavior of carburized 316 stainless steel in molten chloride salts,” Solar Energy, 223, 2021, pp. 1-10.

[28] W. Ding, J. Gomez-Vidal, A. Bonk, T. Bauer, “Molten chloride salts for next generation CSP plants: Electrolytical salt purification for reducing corrosive impurity level,” Solar Energy Materials and Solar Cells, 199, 2019, pp. 8-15.

[29] A. Kruizenga, “Corrosion Mechanisms in Chloride and Carbonate Salts,” SANDIA Report, SAND2012-7594, 2012.

[30] G.Y. Lai, “High-temperature corrosion and materials applications,” Chapter 15: Molten Salt Corrosion, ASM International, 2007, pp. 409-421.

[31] G. Kipouros, D. Sadoway, “A thermochemical analysis of the production of anhydrous $MgCl_2$,” Journal of Light Metals, 1, 2001, pp. 111-117.

[32] J. Wang, H. Zhou, C. Zhang, W. Liu, B. Zhao, “Influence of $MgCl_2$ content on corrosion behavior of GH1140 in molten NaCl-$MgCl_2$ as thermal storage medium,” Solar Energy Materials and Solar Cells, 179, 2018, pp. 194-201.

[33] M. Zhu, H. Ma, M. Wang, Z. Wang, A. Sharif, “Effects of Cations on Corrosion of Inconel 625 in Molten Chloride Salts,” High Temperature Materials and Processing, 35, 2015.

[34] B. Liu, X. Wei, W. Wang, J. Lu, J. Ding, “Corrosion behaviour of Ni-based alloys in molten NaCl-$CaCl_2$-$MgCl_2$ eutectic salt for concentrating solar power,” Solar Energy Materials and Solar Cells, 170. 2017, pp. 77-86.

[35] W. Ding, H. Shi, Y. Xiu, A, Bonk, A. Weisenburger, A. Jianu, T. Bauer, “Hot corrosion behaviour of commercial alloys in thermal energy storage material of molten $MgCl_2$/KCl/NaCl under inert atmosphere,” Solar Energy Materials and Solar Cells, 184, 2018, pp. 22-30.

[36] J. Gomez-Vidal, R. Tirawat, “Corrosion of alloys in a chloride molten salt (NaCl-LiCl) for solar thermal technologies,” Solar Energy Materials & Solar Cells, 157, 2016, pp. 234-244.

[37] M. Hofmeister, L. Klein, H. Miran, R. Rettig, S. Virtanen, R. Singer, “Corrosion behaviour of stainless steels and a single crystal superalloy in ternary LiCl-KCl-CsCl molten salt,” Corrosion Science, 90, 2015, pp. 46-33.

[38] J. Indacochea, J. Smith, K. Litko, E. Karell, A. Raraz, “High-Temperature Oxidation and Corrosion of Structural Materials in Molten Chlorides,” Oxidation of Metals, 55, 2001.

[39] K. Vignarooban, X. Xu, K. Wang, E. Molina, P. Li, D. Gervasio, A. Kannan, “Vapor pressure and corrosivity of ternary-metal chloride molten-salt based heat transfer fluid for use in concentrating solar power systems,” Applied Energy, 159, 2015, pp. 206-213.

[40] L. Wang, B. Li, m. Shen, S. Li, J. Yu, “Corrosion resistance of steel materials in LiCl-KCl melts,” Minerals, Metallurgy, and Materials, 19, 2012, pp. 930-933.

[41] J. Koger, “Alloy Compatibility with LiF-BeF_2 Salts Containing ThF_4 and UF_4,” Oak Ridge National Laboratory, Oak Ridge, TN, December 1972.

[42] M. Anderson, “Heat Transfer Salts for Nuclear Reactor Systems – Chemistry and Control, Corrosion Mitigation, and Modeling,” U.S. Department of Energy, 10-905.

[43] J. De Van, “Effect of Alloying Additions on Corrosion Behavior of Nickel-Molybdenum Alloys in Fused Fluoride Mixtures,” Oak Ridge National Laboratory, Oak Ridge, TN, 1969.

[44] J. Koger, “Evaluation of Hastelloy N alloys after nine years exposure to both a molten fluoride salt and air at temperatures from 700 to 560°C,” Oak Ridge National Laboratory, Oak Ridge, TN, 1972.

[45] H. McCoy, “Status of materials development for molten salt reactors,” Oak Ridge National Laboratory, Oak Ridge, TN, 1978.

[46] K. Vignarooban, P. Pugazhendhi, C. Tucker, D. Gervasio, A. Kannan, "Corrosion resistance of Hastelloys in molten metal-chloride heat-transfer fluids for concentrating solar power applications," Solar Energy, 103, 2017, pp. 62-69.

[47] T. Abdullah, C. Petitjean, P. Pantiex, S. Mathieu, "Electrochemical characterization of chromia- and alumina-forming nickel-based superalloys in molten silicates," Applied Surface Science, 360, 2016, pp. 510-518.

[48] E. Essuman, G. Meier, J. Zurek, M. Hansel, T. Norby, L. Singheiser, W. Quadakkers, "Protective and non-protective scale formation of NiCr alloys in water vapour containing high and low-PO_2 gases," Corrosion Science, 50, 2008, pp. 1753-1760.

[49] J. Lehmusto, P. Yrjas, L. Hupa, "Pre-oxidation as a Means to Increase Corrosion Resistance of Commercial Superheater Steels," Oxidation of Metals, 91, 2019, pp. 311-326.

[50] S. Mathieu, L. Aranda, L. Portebois, S. Mathieu, M. Vilasi, "On the Pre-oxidation Treatments of Four Commercial Ni-Based Superalloys in Air and in Ar-H_2O at 950°C," Oxidation of Metals, 90, 2018, pp. 43-63.

[51] I. Polovov, A. Abramov, o. Rebrin. V. Volkovich, E. Denisov, "Corrosion of Stainless Steels in NaCl-KCl Based Melts," The Electrochemical Society, 33, 2010, pp. 321-327.

[52] B. Garcia-Diaz, L. Olson, M. Rodriguez, R. Fuentes, H. Colon-Mercado, J. Gray, "High Temperature Electrochemical Engineering and Clean Energy Systems," Savannah River National Laboratory, Savannah River Site, 2015.

[53] B. Garcia-Diaz, J. Gray, L. Olson, M. Marinez-Rodriguez, R. Fuentes, "High Temperature Molten Salt Corrosion in CSP Systems," CSP Program Summit, SunShot U.S. Department of Energy, 2016.

[54] C. Villada, W. Ding, A. Bonk, T. Bauer, "Engineering molten MgCl2-KCl-NaCl salt for high-temperature thermal energy storage: Review on salt properties and corrosion control strategies," Solar Energy Materials and Solar Cells, 232, 2021, 111344.

[55] Y. Hosoya, T. Terai, T. Yoneoka, S. Tanaka, "Compatibility of structural materials with molten chloride mixture at high temperature," Journal of Nuclear Materials, 248, 1997, pp. 348-353.

[56] V. Cherginets, T. Rebrova, "Studies of some acid-base equilibria in the molten eutectic mixture KCl-LiCl at 700C," Electrochimica Acta, 45, 1999, pp. 469-476.

[57] W. Callister, D. Rethwisch, "Materials Science and Engineering: An Introduction," John Wiley & Sons, 9th edition, 2014, pp. 709-711.

[58] N. Israelsson, K. Unocic, K. Hellstrom, J. Svenssn, L. Johansson, "Cyclic Corrosion and Chlorination of an FeCrAl Alloy in the Presence of KCl," Oxidation of Metals, 84, 2015, pp. 269-290.

[59] T. Abdullah, C. Petitjean, P. Panteix, S. Mathieu, "Electrochemical characterization of chromia-and alumina-forming nickel-based superalloys in molten silicates," Applied Surface Science, 360, 2016, pp. 510-518.

[60] S. Mathiueu, L. Aranda, L Portebois, S. Mathieu, M. Vilasi, “On the Pre-oxidation Treatments of Four commercial Ni-Based Superalloys in Air and in Ar-H_2O at 950°C,” Oxidation of Metals, 90, 2018, pp. 43-63.

[61] T. Pan, Y. Li, Q. Yang, R. Feng, A. Hirose, “Internal oxidation and phase transformations of multi-phase Fe-Ni-Al and Fe-Ni-Al-Cr alloys induced by KCl corrosion,” Corrosion Science, 53, 2011, pp. 2115-2121.

[62] Y. Li, Y. Niu, M. Spiegel, “High temperature interaction of Al/Si modified Fe-Cr alloys with KCl,” Corrosion Science, 49, 2007, pp. 1799-1815.

[63] W. Weng, M. Wang, X, Gong, “Direct electro-deposition of metallic chromium from K_2CrO_4 in the equimolar $CaCl_2$-KCl molten salt and its reduction mechanism,” Electrochimica Acta, 212, 2016, pp. 162-170.

[64] A. Chyrkin, N. Mortazavi, M. Halvarsson, D. Gruner, W.J. Quadakkers, “Effect of thermal cycling on protective properties of alumina scale grown on thin Haynes 214 foil,” Corrosion Science, 98, 2015, pp. 688-698.

[65] D. Young, A. Chyrkin, J. He, D. Gruner, W.J. Quadakkers, “Slow Transition from Protective to Breakaway Oxidation of Haynes 214 Foil at High Temperature,” Oxidation of Metals, 79, 2013, pp. 405-427.

[66] Y. Zhang, D. Zou, X. Wang, Q. Wang, R. Xu, W. Zhang, “Influences of Si content on the high-temperature oxidation behaviour of X10CrAlSi18 ferritic heat-resistant stainless steel at 700C and 800C,” Surface & Coatings Technology, 422, 2021, 127523.

[67] S. Rashidi, J. Choi, J. Stevenson, A. Pandey, R. Gupta, “High temperature oxidation behavior of aluminized Haynes 230,” Corrosion Science, 174, 2020, 108835.

[68] T. Dudziak, L. Boron, M. Homa, R. Nowak, N. Horton, R. Sheppard, R. Purgent, A. Siewiorek, N. Sobczak, J. Sobczak, “The Influence of Fabrication Process on the Initial Stages of Steam Oxidation Performed on Haynes 282 Alloy at 760oC,” Journal of Materials Engineering and Performance, 26, 2017, pp. 239-249.

[69] V. Deodeshmukh, S. Srivastava, “Long-term Cyclic Oxidation Behaviour of Selected High Temperature Alloys,” The Minerals, Metals & Materials Society, pp. 689-698.

[70] L. Xiao, G. Cota-Sanchez, “Microstructural Characterization and Tensile Properties Assessment of GTAW Welded Incoloy 800H Alloys Fuel Cladding for SCWR,” Canadian Nuclear Laboratories, Chalk River, 2021.

[71] E. Hamzah, M. Mundang, M. Khattak, “Effect of variation in microstructure on high temperature creep of Fe-Ni-Cr superalloy,” the World Congress on Advances in Structural Engineering and Mechanics (ASEM13), Keju, Korea, 2013.

[72] R. Dehmolaei, M. Shamanian, A. Kermanpur, “Microstructural changes and mechanical properties of Incoloy 800 after 15 years service,” Materials Characterization, 60, 2009, pp. 246-250.

[73] M. Nafari, A. Salemi Golezani, “Heat affected zone creep characterization of Incoloy 800H by means of small punch test,” Engineering Failure Analysis, 94, 2018, pp. 407-411.

[74] L. Vellaichamy, P. Benedict, T. Gerard, S. Paulraj, "Mechanical and Metallurgical Characterization of Laser Wedling on P91 Ferritic Steel and Incoloy 800HT Dissimilar Joints," Materials Research, 21, 2018.

[75] Y. Kurata, M. Futakawa, S. Saito, "Comparison of the corrosion behaviour of austenitic and ferritic/martensitic steels exposed to static liquid Pb-Bi at 450 and 550°C," Journal of Nuclear Materials, 343, 2005, pp. 333-340.

[76] S. Mahboubi, "Effect of Cr content on corrosion resistance of Fe-Cr-Ni alloys exposed in supercritical water," MASc thesis, McMaster University, Hamilton, ON, 2014.

[77] W. Chen, W. Kai, L. Tsay, J. Kai, "The oxidation behavior of three different zones of welded Incoloy 800H alloy," Nuclear Engineering and Design, 272, 2014, pp. 92-98.

[78] D. Kim, D. Seo, J. Tsang, W. Yang, J. Lee, H. Saari, C. Seok, "The crack growth behavior of Incoloy 800H under fatigue and dwell-fatigue conditions at elevated temperature," Journal of Mechanical Science and Technology, 26, 2012, pp. 2023-2027.

[79] W. Zheng, H. Li, Q. Wang, H. Yin, X. He, H. Fan, T, Ma, "Oxidation behavior of the high temperature alloys in the impure helium and argon," Proceedings of the 2021 28th International Conference on Nuclear Engineering, Virtual, Aug. 2021.

[80] A. Syamimi, H. Wahab, T. Abdullah, "High Temperature Isothermal Oxidation Behavior of Superheater Materials," Materials Today: Proceedings, 17, 2019, pp. 829-835.

[81] C. Li, P. Li, K. Wang, E. Molina, "Survey of Properties of Key Single and Mixture Halide Salts for Potential Application as High Temperatuer and Heat Transfer Fluids for Concentrated Solar Thermal Power Systems," AIMS Energy, 2, 2014, pp. 133-157.

[82] K. Mahboob, A. Khan, M. Khan, "Comparison of Li_2CO_3-K_2CO_3, KCl-$MgCl_2$ and $NaNO_3$-KNO_3 as heat transfer fluid for different sCO2 steam power cycles in CSP tower plan under different DNI conditions," Advances in Mechanical Engineering, 13, 2021, pp. 1-17.

[83] A. Ramos-Ballesteros, R. Gakhar, G. Horne, K. Iwamatsu, J. Wishart, S. Pimblott, J. LaVerne, "Gamma radiation-induced defects in KCl, MgCl2, and ZnCl2 salts at room temperature," Physical Chemistry Chemical Physics, 23, 2021, 10384.

[84] J. Lu, S. Yang, Z. Rong, G. Pan, J. Ding, S. Liu, X. Wei, W. Wang, "Thermal properties of KCl-MgCl2 eutectic salt for high-temperature het transfer and thermal storage system," Solar Energy Materials and Solar Cells, 228, 2021, 111130.

[85] S. Polimeni, M. Binotti, L. Moretti, G. Manzolini, "Comparison of sodium and KCl-MgCl2 as heat transfer fluids in CSP solar tower with sCO2 power cycles," Solar Energy, 162, 2018, pp. 510-524.

[86] D. Williams, K. Clarno, "Evaluation of Salt coolants for Reactor Applications," Nuclear Technology, 163:3, 2017, pp. 330-343.

[87] J. Goldstein, D. Newbury, J. Michael, "Scanning Electron Microscopy and X-Ray Microanalysis," fourth edition, Springer Nature, 2018, pp. 66-67.

[88] W. Ding, A. Bonk, J. Gussone, T. Bauer, “Cyclic Voltammetry for Monitoring Corrosive Impurities in Molten Chlorides for Thermal Energy Storage,” Energy Procedia, 135, 2017, pp. 82-91.

[89] S. Boghosian, A. Good, H. Mediaas, “Oxide Complexes in Alkali-Alkaline Earth Chloride Melts,” Acta Chemica Scandinavica, 45, 1991, pp. 145-157.

[90] F. Stott, F. Wei, “Comparison of the Effects of Small Additions of Silicon or Aluminum on the Oxidation of Iron-Chromium Alloys,” Oxidation of Metals, 31, 1989, pp. 369-391.

[91] W. Weng, M. Wang, X, Gong, “Direct electro-deposition of metallic chromium from K_2CrO_4 in the equimolar $CaCl_2$-KCl molten salt and its reduction mechanism,” Electrochimica Acta, 212, 2016, pp. 162-170.

[92] Z. Zhang, F. Gesmundo, P. Hou, Y. Niu, “Criteria for the formation of protective Al_2O_3 scales on Fe-Al and Fe-Cr-Al alloys,” Corrosion Science, 48, 2006, pp. 741-765.

[93] G. Kipouros, D. Sadoway, “The Chemistry and Electrochemistry of Magnesium Production,” Advances in Molten Salt Chemistry, Vol. 6, 1987, pp. 127-209.

[94] M. Brady, Y. Yamamoto, M. Santella, P. Maziasz, B. Pint, C. Liu, Z. Lu, H. Bei, “The Development of Alumina-Forming Austenitic Stainless Steels for High-Temperature Structural Use,” The Materials Society, 2008, pp. 12-18.

[95] M. Hofmeister, L. Klein, H. Miran, R. Rettig, S. Virtanen, R. Singer, “Corrosion behaviour of stainless steels and a single crystal superalloy in ternary LiCl-KCl-CsCl molten salt,” Corrosion Science, 90, 2015, pp. 46-33.

[96] W. Chen, W. Kai, L. Tsay, J. Kai, “The oxidation behaviour of three different zones of welded Incoloy 800H alloy,” Nuclear Engineering and Design, 272, 2014, pp. 92-98.

[97] D. Kim, D. Seo, J. Tsang, W. Yang, J. Lee, H. Saari, C. Seok, “The crack growth behaviour of Incoloy 800H under fatigue and dwell-fatigue conditions at elevated temperature,” Journal of Mechanical Science and Technology, 26, 2012, pp 2023-2027.

[98] W. Zheng, H. Li, Q. Wang, H. Yin, X. He, H. Fan, T. Ma, “Oxidation behaviors of the high temperature alloys in the impure helium and argon,” 28th International Conference on Nuclear Engineering, Virtual, Aug. 2021.

[99] Y. Zhang, D. Zou, X. Wang, Q. Wang, R. Xu, W. Zhang, “Influences of Si content on the high-temperature oxidation behaviour of X10CrAlSi18 ferritic heat-resistant stainless steel at 700°C and 800°C,” Surface & Coating Technology, 422, 2021, 127523.

[100] Y. Kurata, M. Futakawa, S. Saito, “Comparison of the corrosion behaviour of austenitic and ferritic/martensitic steels exposed to static liquid Pb-Bi at 450 and 550°C,” Journal of Nuclear Materials, 343, 2005, pp. 333-340.